Failure Analysis of Thin Film Solar Modules using Lock-in Thermography

Max Henrik Siegloch

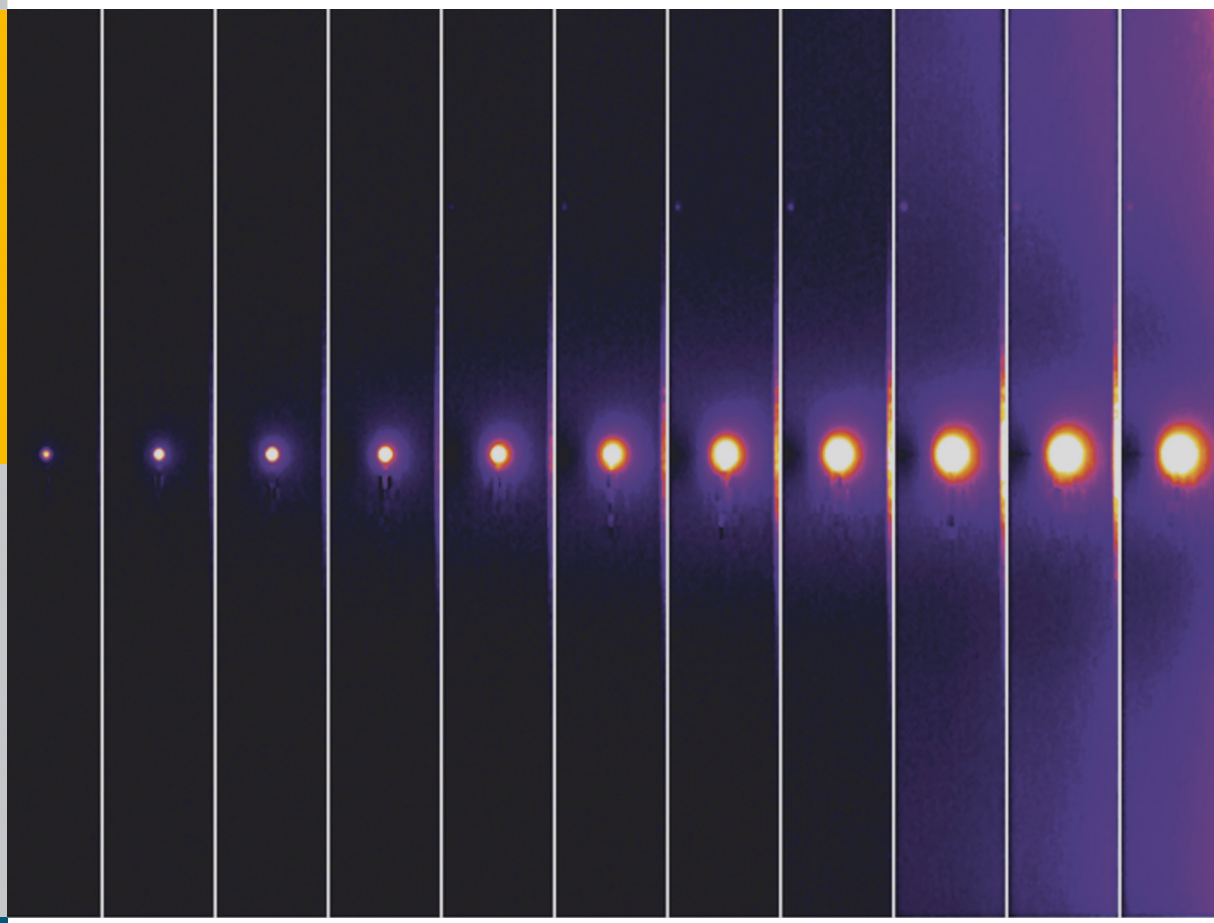

Energie & Umwelt / Energy & Environment
Band / Volume 258
ISBN 978-3-95806-047-0

Member of the Helmholtz Association

JÜLICH
FORSCHUNGSZENTRUM

Schriften des Forschungszentrums Jülich
Reihe Energie & Umwelt / Energy & Environment Band / Volume 258

Forschungszentrum Jülich GmbH
Institute of Energy and Climate Research
IEK-5 Photovoltaics

Failure Analysis of Thin Film Solar Modules using Lock-in Thermography

Max Henrik Siegloch

Schriften des Forschungszentrums Jülich
Reihe Energie & Umwelt / Energy & Environment Band / Volume 258

ISSN 1866-1793 ISBN 978-3-95806-047-0

Bibliographic information published by the Deutsche Nationalbibliothek.
The Deutsche Nationalbibliothek lists this publication in the Deutsche Nationalbibliografie; detailed bibliographic data are available in the Internet at http://dnb.d-nb.de.

Publisher and Distributor: Forschungszentrum Jülich GmbH
Zentralbibliothek
52425 Jülich
Tel: +49 2461 61-5368
Fax: +49 2461 61-6103
Email: zb-publikation@fz-juelich.de
www.fz-juelich.de/zb

Cover Design: Grafische Medien, Forschungszentrum Jülich GmbH

Printer: Grafische Medien, Forschungszentrum Jülich GmbH

Schriften des Forschungszentrums Jülich
Reihe Energie & Umwelt / Energy & Environment, Band / Volume 258

D 82 (Diss. RWTH Aachen Univ., 2014)

ISSN 1866-1793
ISBN 978-3-95806-047-0

The complete volume is freely available on the Internet on the Jülicher Open Access Server (JuSER) at www.fz-juelich.de/zb/openaccess.

Abstract

Lock-in thermography (LIT) is an imaging method that depicts radiated heat and its diffusion in manifold samples. LIT offers versatile possibilities for the characterization of solar cells and modules since the radiated heat is proportional to the dissipation of electrical power. Up to now, the quantitative correlation of detected heat and dissipated electrical power has been known for silicon solar cells only. For many other types of solar cells and modules – especially thin film solar cells – LIT has been used as a qualitative measurement tool for depicting the location of defects, for example. Thus, the potential of LIT in terms of the calculation of power generation and dissipation in thin film solar cells has not been exploited. This visualization and calculation of power flows leads to a better understanding of the influences of defects on the efficiency of solar modules. Furthermore, it enables the evaluation of potential improvements, which results in solar modules with higher efficiencies, produced to lower costs.

In order to interpret LIT signals accurately, the lock-in algorithm and particularly its limits have to be understood. The present thesis shows the evaluation of the lock-in algorithm and its algebraic complex result with simulations. It is found that the weak points of the lock-in algorithm lie in the sampling of the acquired heat signal. Sampling moments that are not uniformly distributed in a lock-in period produce unreliable results. A low sampling at high measurement frequencies shows significant deviations distorting the LIT result. The findings allow for the development of user-friendly LIT systems that automatically avoid sampling errors and produce reliable LIT results.

The comprehension of LIT measurements of thin film solar cells needs a theoretical thermal model for the solar cells that can be used to solve the differential heat diffusion equation. The solution describes the surface temperature distribution that is acquired in LIT measurements. By the evaluation of the frequency response of a point heat source in a thin film solar cell, a simple thermal model representing a solid body is found to adequately reproduce LIT measurements.

LIT investigations in the scale of the thermal diffusion length are hampered by the diffusion of heat that leads to a blurring of heat sources. With the description of the thermal model and a Fourier transform technique, it is possible to successfully deconvolute the heat generating sources from the heat diffusion, meaning the removal of the thermal blurring. This leads to the unimpeded visualization of the dissipated power of small heat sources such as shunts or the series interconnection of cells in a thin film solar module.

To deconvolute LIT measurements of samples, which thermal model is not known, an advanced LIT system is developed. It uses a small laser beam, which is di-

rected at the solar cell and is measured by the LIT setup, in order to obtain the heat diffusion in the sample. The deconvolution adequately reproduces the size of a shunt. Combined with an evaluation algorithm, such an LIT system is carrying out a "self-calibration" for the heat diffusion in any kind of solar cell sample. This enables the system to autonomously detect the dissipated power in manifold devices.

Up to now, the estimation of power losses in solar cells commonly has been carried out with LIT measurements without illumination. This is justified for crystalline silicon solar cells, since their behavior in illuminated conditions can be calculated from unilluminated conditions with a simple model. In thin film solar modules, the electrical behavior in illuminated and unilluminated conditions differs significantly. Thus, the access to power losses lies in LIT measurements of solar modules in operation conditions: with illumination and at a voltage enabling the maximal extraction of power. The quantification of such measurements is impeded by several overlapping heat dissipation mechanisms occurring in thin film solar modules. With new developed LIT methods using a bias voltage modulation under constant illumination, the overlapping heat dissipation mechanisms are resolved and a power scaling for LIT images is achieved. These novel LIT methods thus propose an approach to realistic estimations of power losses in thin film solar modules.

Furthermore, the novel LIT methods allow the investigation of single cells and their interaction in the compound of a module. In industrial solar modules, cells are capsuled and cannot be contacted to determine their electrical behavior in the compound. A specially constructed laboratory scale solar mini-module allowed the contacting of the cells and the acquisition of their electrical characteristics. A good representation of the electrical behavior of the cells in the module compound in LIT measurements with the new methods was found. In future, these methods can be used for the comparison with simulations of the electrical behavior of solar modules. Findings derived from such a comparison allow for finding critical efficiency-limiting features in solar modules.

Kurzfassung

Lock-in Thermographie (LIT) ist ein bildgebendes Verfahren, das ausgestrahlte Wärme und ihre Diffusion von vielfältigen Proben darstellt. Die LIT bietet vielseitige Möglichkeiten für die Charakterisierung von Solarzellen und –modulen, da die ausgestrahlte Wärme von Solarzellen proportional ist zur elektrischen Verlustleistung, die in ihnen auftritt. Bis jetzt war der quantitative Zusammenhang der gemessenen Wärme und der elektrischen Verlustleistung nur für Solarzellen aus kristallinem Silizium bekannt. Für viele andere Arten von Solarzellen und -modulen – insbesondere Dünnschichtsolarzellen – wurde LIT vor allem als qualitatives Messinstrument genutzt, z.B. zur Bestimmung der Position von Defekten. Demzufolge wurden die Möglichkeiten von LIT in Bezug auf die Berechnung von Leistungserzeugung und -verbrauch in Dünnschichtsolarzellen bisher nicht ausgenutzt. Gerade aber die Verbildlichung von Leistungsflüssen führt zu einem besseren Verständnis des Einflusses von Defekten auf den Wirkungsgrad von Solarmodulen. Weiterhin gestattet diese Verbildlichung die Beurteilung von möglichen Verbesserungen, die zu Solarmodulen mit höherem Wirkungsgrad und niedrigeren Produktionskosten führen.

Um LIT-Signale genau interpretieren zu können, braucht man ein tiefes Verständnis des Lock-in Algorithmus und insbesondere dessen Grenzen. Die vorliegende Arbeit analysiert den Lock-in Prozess und die aus ihm resultierende, algebraisch komplexe Größe mithilfe von Simulationen. Die Analyse zeigt, dass der Algorithmus Schwachstellen in der Abtastung des gemessenen Wärmesignals aufweist. Unzuverlässige Ergebnisse werden produziert, wenn die Abtastungszeitpunkte ungleichmäßig über eine Lock-in Periode verteilt liegen. Eine Unterabtastung bei hohen Messfrequenzen zeigt deutliche Abweichungen, die das resultierende LIT Signal verfälschen. Die Untersuchungsergebnisse erlauben die Entwicklung eines benutzerfreundlichen LIT Systems, das Abtastungsfehler automatisch vermeidet und verlässliche Resultate liefert.

Das Verständnis von LIT Messungen von Dünnschichtsolarzellen benötigt ein theoretisches thermisches Modell, das man zur Berechnung der Differentialgleichung der Wärmediffusion nutzen kann. Die Lösung der Differentialgleichung beschreibt die Wärmeverteilung der Oberfläche einer Solarzelle, welche mit LIT gemessen wird. Benutzt wird ein einfaches thermisches Modell, das die Solarzelle als einen einzelnen Festkörper nachbildet. Durch die Analyse des Frequenzganges einer Punktwärmequelle in einer Dünnschichtsolarzelle wird herausgefunden, dass dieses Modell LIT Messungen hinreichend reproduziert.

LIT-Untersuchungen in der Größenordnung der thermischen Diffusionslänge werden durch Wärmediffusion eingeschränkt, welche eine Unschärfe über Wärmequel-

len legt. Die Beschreibung durch das thermische Modell und eine Fourier-Transformationstechnik ermöglicht die Entfaltung der Wärmequellen von der Wärmediffusion und führt zur Entfernung der thermischen Unschärfe. Dies resultiert in einem störungsfreien Bild der Verlustleistung kleiner Wärmequellen wie z.B. lokale Kurzschlüsse (sogenannte Shunts) oder die Serienverschaltung von Zellen in einem Dünnschichtsolarmodul.

Zur Entfaltung der LIT Messungen von Proben, deren thermisches Modell unbekannt ist, wird ein erweitertes LIT System entwickelt. Dieses nutzt einen Laserstrahl, der auf die Solarzelle gerichtet ist und vom LIT System gemessen wird. Dadurch erhält man die Wärmediffusion in der Probe. Die Entfaltungsergebnisse des erweiterten LIT Systems reproduzieren die Größe eines Shunts annehmbar genau. Kombiniert mit einem Evaluationsalgorithmus führt ein solches LIT System eine „Selbst-Kalibrierung“ zur Entfernung der Wärmediffusion für beliebige Arten von Solarzellproben durch. Dies ermöglicht die autonome Ermittlung der Verbrauchsleistung in vielfältigen Bauelementen.

Die Schätzung von Leistungsverlusten in Solarzellen wurde bisher mit LIT Messungen ohne Beleuchtung ausgeführt. Dieses Vorgehen ist gerechtfertigt für Solarzellen aus kristallinem Silizium, da deren Verhalten im beleuchteten Fall einfach aus dem beleuchteten Fall berechnet werden kann. Bei Dünnschichtsolarmodulen unterscheidet sich das elektrische Verhalten im beleuchteten und unbeleuchteten Fall maßgeblich. Deshalb können nur LIT Messungen von Solarmodulen unter Betriebsbedingungen eine Einsicht in Leistungsverluste bringen, d.h. unter Beleuchtung und bei einer angelegten Spannung, die maximale Leistungsentnahme ermöglicht. Die Quantifizierung von LIT Messungen unter diesen Bedingungen wird erschwert durch verschiedene sich überlagernde Verlustmechanismen, die in Dünnschichtsolarmodulen vorkommen. Diese Überlagerungen werden durch neu entwickelte LIT Methoden aufgelöst, die eine Spannungsmodulation unter konstanter Beleuchtung benutzen. Mit diesen Methoden wird ein Maßstab zur Leistungsskalierung von LIT Bildern erreicht. Die neuen Methoden schlagen somit einen Ansatz vor, wie Leistungsverluste in Dünnschichtsolarmodulen unter realistischen Betriebsbedingungen abgeschätzt werden können.

Weiterhin erlauben die neuen LIT Methoden die Untersuchung von Einzelzellen im Modulverbund und deren Wechselwirkung. Industriell hergestellte Solarmodule verkapseln Einzelzellen, welche dadurch nicht einzeln zur Aufnahme ihres elektrischen Verhaltens kontaktiert werden können. Ein speziell konstruiertes Solarmodul im Labormaßstab erlaubt die Kontaktierung der Einzelzellen und die Ermittlung ihres elektrischen Verhaltens. Ein Vergleich zeigt eine gute Abbildung des elektrischen Verhaltens der Zellen im Modul durch die neuen LIT Methoden. In Zukunft können diese Methoden benutzt werden, um ihre Ergebnisse mit denen von Simulationen des elektrischen Verhaltens von Solarmodulen zu vergleichen. Die Erkenntnisse aus solchen Vergleichen werden es erlauben, kritische und wirkungsgradlimitierende Eigenschaften sowie Defekte in Solarmodulen ausfindig zu machen.

Table of Contents

List of Figures

List of Tables

List of Abbreviations

acronym	meaning
AM1.5G	air mass 1.5 global
CDI	carrier density imaging
CELLO	solar cell local characterization
DLIT	dark lock-in thermography
EL	electroluminescence
FIB	focused ion beam
FWHM	full width at half maximum
i	intrinsic (not doped)
IC	integrated circuit
IEK-5	Institute of Energy and Climate Research 5 at Forschungszentrum Jülich
ILIT	illuminated lock-in thermography
IQE	internal quantum efficiency
IR	infrared
LBIC	laser-beam induced current
LED	light emitting diodes
Limo-LIT	light modulated LIT
LIT	lock-in thermography
LIVT	local *I/V* characteristics measured thermally
LWIR	long wave infrared
MPP	maximum power point
MWIR	mid wave infrared
n	negatively doped
NDT	non-destructive testing
p	positively doped
PECVD	plasma enhanced chemical vapor deposition
PSF	point spread function

PV	photovoltaic
SEM	scanning electron microscopy
SNR	signal-to-noise ratio
SRH	Shockley-Read-Hall
SWIR	short wave infrared
TCO	transparent conductive oxide
Vomo-ILIT	voltage-modulated illuminated LIT
Vomo-LIT	voltage-modulated LIT

chemical symbol	element / compound
µc-Si:H	microcrystalline hydrogenated silicon
a-Si:H	amorphous hydrogenated silicon
Ag	silver
CdTe	cadmium telluride
CIGS, $Cu(In,Ga)Se_2$	copper indium gallium diselenide
CO_2	carbon dioxide
H_2O	water
Si	silicon
SnO_2	tin oxide
ZnO	zinc oxide

1 Introduction

In the past decade, the world's demand for photovoltaic (PV) devices increased vigorously [1]. The main reason is the introduction of feed-in tariffs in several countries, especially Germany [2], which made it financially awarding for investors to build PV generators. Along with cheap credits, many people owning a house and farmers with large roof areas on barns embraced the opportunity to build PV generators on their roofs. Even free standing PV plants became attractive as an investment, often organized within community companionships.

The increasing demand triggered a growth of industry and research funds. This resulted in a decrease of the prices of PV devices, in an increase in their efficiency, and in a tremendous growth of the PV market. With the maturity of PV technology, a deceleration in the reporting of efficiency records came along [3]. Further increase of efficiency and further cost reductions require a better understanding of the underlying physical mechanisms of solar cells and modules. The potential of improving solar cells is getting to its limits, yet there is still a lot of potential of optimizing the interconnection of solar cells to modules, and the further upscaling of solar modules to PV generator arrays [4, 5].

To detect further technology-specific characteristics deteriorating the module performance and to find potential improvements in module technology, advanced characterization tools are needed. Lock-in Thermography (LIT) [6, 7] is one such tool, along with other imaging methods such as Electroluminescence imaging (EL) [8, 9, 10]. In the last decade, both techniques became more and more popular. Many LIT investigations have been carried out on crystalline silicon solar cells [11, 6]. Only few research contributions were dedicated to a quantitative study and application to thin film solar cells and modules [12, 13, 14, 15, 16, 17]. However, thin film devices are considered the upcoming second generation of PV generators [18, 19] with a huge potential for cost reductions.

The present thesis focuses on the application of LIT on thin film *silicon* solar modules with LIT. Most of the results are transferable to other thin film technologies. The LIT measurements in this study allow for a quantitatively correct failure analysis of thin film solar modules. Furthermore, the combination of the presented experimental results with simulations provides a basis for the analysis of solar modules aiming to find promising attempts for efficiency gains.

The thesis starts with Chapter 2 explaining the design and composition of thin film silicon solar modules. The equivalent circuit model is used to explain the influence of defects on the electrical characteristics of solar modules. The differences to standard

crystalline solar cells are discussed and heat dissipation and transport mechanisms in solar modules that are visualized by LIT images are explained.

Chapter 3 deals with infrared radiation and its detection with thermographic methods. The theory of the lock-in method is derivated, resulting in the generated complex lock-in signal *S*. Pitfalls in the usage of lock-in algorithms are discussed including their prevention. The LIT setup is introduced along with an overview of existing LIT methods and novel methods developed in this thesis.

Chapter 4 presents basic investigations with LIT. Measurement parameters and preferences are discussed, focusing on their influence on the detection and localization of different defects. The quantification of the experimental thermal signal to a power density is described. Series resistances and shunts (small local short-circuits) are evaluated qualitatively and quantitatively. The origin of shunts in thin film silicon solar cells is revealed with help of microscopic investigations. The consequences of reverse biasing thin film solar cells are discussed, combined with a critical review of the popular technique of "shunt removing" or "shunt bursting". A physical explanation for its functional principle is proposed. Furthermore, basic LIT investigations with modulated illumination as stimulus are presented and the derived results are discussed. At last, the detection of radiation through a glass panel and its drawbacks are investigated.

Chapter 5 introduces a thermal model that allows a deep analysis of the theoretical LIT signal of thin film solar cells and modules. The theoretical frequency response of thin film solar modules is calculated and criteria for the correct acquisition of the signal phase are discussed.

Chapter 6 describes a technique called deconvolution, which is applied to a thin film solar module. It separates the electrically dissipated power from the heat diffusion – which is inherent to all LIT images – by calculating the heat diffusion differential equation. As result, the deconvolution technique enhances the thermal spatial resolution of LIT images. A self-calibrating LIT system is introduced that bypasses the calculation of the heat diffusion with a measurement, allowing for the development of an automated LIT system with a high thermal spatial resolution.

Chapter 7 introduces a novel method that gives realistic access to the power dissipation of defects at the operation point of solar cells, i.e. their maximum power point (MPP). This novel method uses voltage-modulated LIT under constant illumination. It is a quantitative investigation method that records LIT images at differential biases. Voltage-modulated LIT under illumination allows insight into the interaction and operation of cells in a module without the need for electrical contacts of each cell.

The thesis closes with chapter 8 summarizing the main results and conclusions and giving an outlook on possible applications.

2 Thin film silicon solar cells and modules

This chapter describes the design and interconnection of thin film silicon solar cells. The electrical diode characteristics and crucial electrical parameters are derived using an equivalent circuit model. Specific properties of thin film silicon solar modules are outlined and contrasted to standard crystalline silicon solar cells. A detailed evaluation of heat dissipation and transport mechanisms in solar cells is given.

2.1 Design of thin film silicon solar modules

Thin film solar cells consist of several functional layers with an overall thickness of about 1 to 7 µm. The thin layers are deposited on a substrate, which can be glass, plastic or a metal. The three most common inorganic material systems for the photovoltaically active layers are copper indium gallium diselenide ($Cu(In,Ga)Se_2$, short CIGS), cadmium telluride (CdTe), and amorphous and microcrystalline hydrogenated silicon (*a*-Si:H, µc-Si:H). Details on the first two technologies can be found in [20]. In my thesis, I focus on thin film *a*-Si and µc-Si solar cells and modules [4, 21]. Most results found in this thesis can yet be transferred to CIGS and CdTe solar cells and modules.

Thin film silicon solar cells are composed as sketched in Figure 2.1. They are built in a so called superstrate configuration, i.e. the incoming light passes through the glass superstrate and the transparent front electrode (transparent conductive oxide, TCO), which is usually made of tin oxide (SnO_2) [22] or zinc oxide (ZnO) [23, 24]. The TCO has to fulfill three important requirements: Transparency, as the incoming light should mainly be absorbed in the photovoltaically active material. Conductivity, as charge carriers generated in the adjacent active material ought to be transported with few losses to outer contacts. Scattering, as light rays have to be refracted into large angels to enhance the light-path in the thin absorber layer. To obtain the latter mentioned effect, the TCO surface is roughened – usually by etching – after deposition on the glass superstrate.

After being refracted and scattered by the TCO, the light reaches the absorber layer, where it generates charge carriers in the form of electron-hole pairs. These pairs are separated by a built-in electrical field, so that the holes drift to the front and the electrons to the back contact, where they can be extracted. Details of this process are shown in chapter 2.2. The absorber is usually an *a*-Si or µc-Si layer, or a stack of the two. The latter case is called tandem solar cell [25] and is displayed in Figure 2.1b. Both absorber layers are electrically connected in series with a tunnel junction in-between.

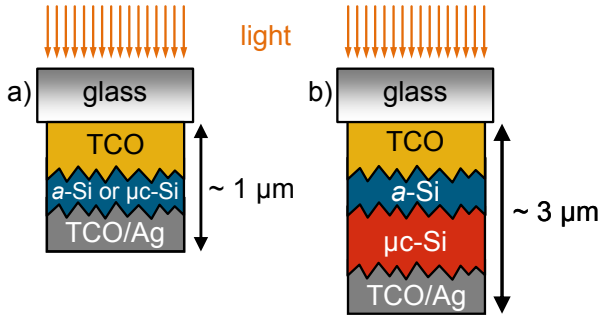

Figure 2.1: Composition of thin film silicon solar cells. a) Single-junction solar cell with a-Si or µc-Si as absorber layer. b) Tandem solar cell with an absorber layer combining an a-Si and a µc-Si cell in series. The general composition is the same: On a glass superstrate, a transparent conductive oxide (TCO) as front contact is deposited. Light reaches the absorber through the glass and the TCO. It is reflected back into the absorber at the metal rear contact. Tandem solar cells reach higher conversion efficiencies than single-junction solar cells due to their better use of the photon energies.

As the light reaches the *a*-Si cell first, this cell is usually referred to as top cell, whereas the µc-Si cell is called bottom cell. The advantage of the tandem configuration is the combination of the good absorption of *a*-Si in the "blue" low wavelength range (~ 250 to 770 nm) with the one of µc-Si, which reaches up to 1100 nm. Tandem cells achieve higher efficiencies than single *a*-Si or µc-Si cells as they reduce thermalization losses and improve the absorption efficiency. Furthermore, the effect of light-induced degradation of *a*-Si [26] is less when using thinner *a*-Si layers in tandem configuration.

All functional layers are deposited in vacuum processes [27]; e.g. the absorber layers are manufactured by plasma enhanced chemical vapor deposition (PECVD) processes. These processes are principally scalable to large superstrates; the largest deposition chambers in industry were built for 2.6 × 2.6 m² glass panels [28]. With such a large area, a quite high current would theoretically be obtained, if just one solar cell would be made out of one panel. However, the voltage of the device would be very low compared to the current and even more important, the resistance of the TCO would lead to tremendous losses in the transport of the high current. Therefore, instead of manufacturing a single solar cell on the glass sheet, a complete module is produced by integrating a series connection. This connection is produced by laser scribing processes during the production that ablate the material in the desired design [29]. Narrow cells (4 to 10 mm) are formed and connected in series limiting the generated current and producing a high output voltage favorable for the detached electrical loads. Figure 2.2 describes the laser scribing processes used for the implementation of the integrated series connection.

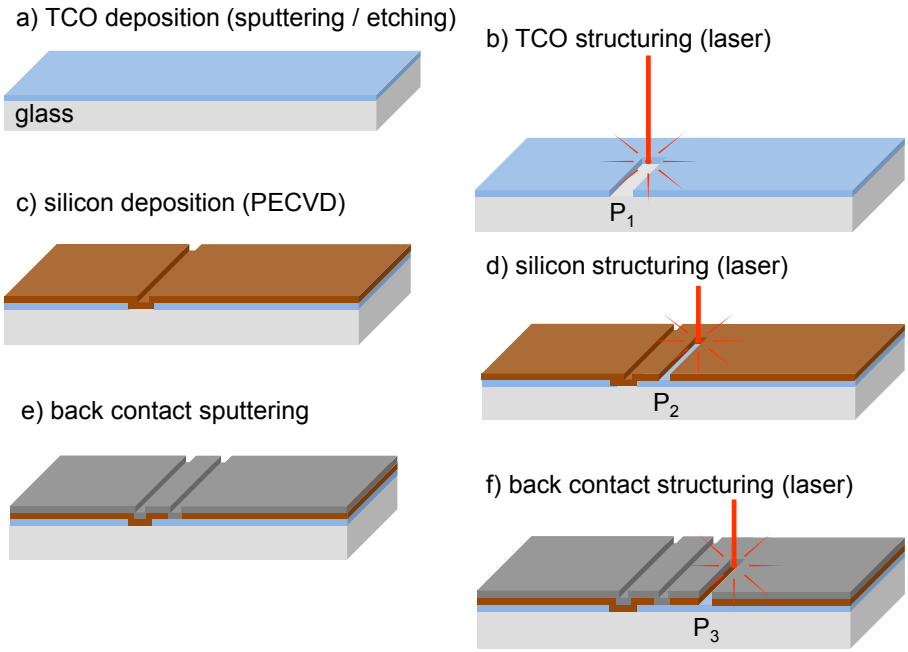

Figure 2.2: Integrated series connection of thin film silicon solar modules. Three structuring steps (b, d, f) in between layer depositions (a, c, e) enable the series connection. A laser ablates a thin trench in each layer, separating the conducting layers. The deposition of the back contact onto the open front contact (e) connects neighboring cells in series.

The laser scribing steps have to be carried out in-between the deposition of the functional layers. After the TCO deposition (a) via sputtering and its etching for the surface roughening, the first structuring line called P_1 is cut in the TCO layer (b). During the silicon deposition (c), silicon adheres on the TCO layer and in the laser-cut trench, where it isolates the TCO areas. The second laser scribe called P_2 structures the silicon (d) and leaves the TCO layer unspoiled. After the back contact sputtering (e) the third and last laser scribe called P_3 (f) cuts through the silicon and the back contact. Now a direct contact between back contact and TCO is formed so that the current flows from the back contact of the cell on the left to the front contact of the right cell. No short-circuits are induced, as P_1 and P_3 completely open the uniform contact layers. The final current path in a module is shown in Figure 2.3. Errors in the scribing process can lead to short-circuits or other defect. One such error is discussed in chapter 6.2.

The terminals for contacting the solar module both lie at the rear side and do not overlap the aperture area. At the Institute of Energy and Climate Research 5 at Forschungs-zentrum Jülich (IEK-5), all productions processes for silicon thin film modules are carried out.

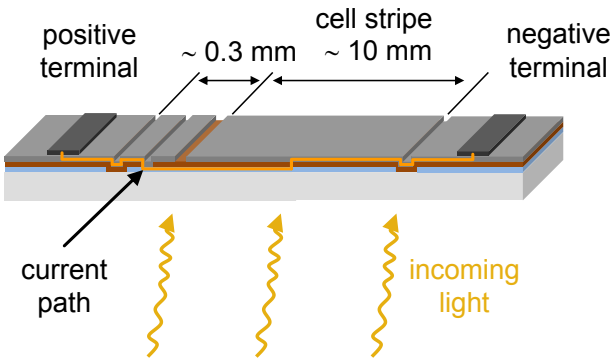

Figure 2.3: Current path through a thin film module with integrated series connection. The series connection enables easy access to the contacting of a thin film module, which occurs completely from the back side of the module. The current has to pass the connection of the front and the back contact, and the absorber layer once. The current direction depends on whether the module is under illumination or biased with a voltage. In the first case, it flows to the right in direction of the image plane, in the second case to the left. The series connection leaves an area with the width of about 0.3 mm *behind that does not contribute to the current collection.*

The sizes of the produced modules are 8 × 8 cm², 26 × 26 cm² and 36 × 36 cm². In my work, I concentrate on the investigation of lab scale modules with the size of 8 × 8 cm². Figure 2.4 shows photographs of such thin film silicon solar modules produced at IEK-5. The module on the left is a standard tandem module shown from the front side. The module on the right is a special *a*-Si module with led-out terminal areas for contacting each cell, shown from the rear side. The special module was produced for investigations of the behavior of single cell stripes in a module (see chapters 4.3 and 4.5). Standard modules have completely isolated rims, i.e. a laser scribe step ablates all layers in a trench. To obtain the terminals, the rims of the special module were not isolated completely; just the laser scribes P_1 and P_2 were carried out between the module rim and the terminals.

2.2 Equivalent circuit model of solar cells and modules

For a profound understanding of the electrical behavior of solar cells and modules, their electrical equivalent circuit model can be used. The model and the mathematical description help to investigate and understand the influence of the various material and device properties on the accessible characteristic solar cell quantities.

Figure 2.4: Mini modules used for laboratory investigations. Left: Standard tandem mini module. The glass superstrate measures 10 × 10 cm², *the device area is* 8 × 8 cm². *The cell widths are adjusted to the type of module: For a-Si modules, it has been found that around* 7 mm *is optimal; for µc-Si* 5 mm *[29] and for tandem modules* 10 mm, *as shown here. Right: Special a-Si module with led-out contacting terminals shown from rear side. The design of the module allows for contacting each single cell stripe of the module separately (red rectangles).*

These quantities are the short-circuit current density[1] J_{sc}, the open-circuit voltage V_{oc}, the fill factor *FF*, the efficiency η, and the maximum power point with its current density J_{MPP}, voltage V_{MPP} and power P_{MPP} [30, p. 124]An appropriate model for the integral description of many types of solar cells is the two diode model shown in Figure 2.5a. It models a solar cell electrically as a current source for J_{sc}, a diode each for the radiative (D_1) and the Shockley-Read-Hall (SRH) recombination (D_2), and two resistances detached in series (R_s) and parallel (R_p), respectively. The common mathematical interpretation is the current/voltage (*J/V*) characteristics for the "dark" (unlighted) and illuminated state as displayed in Figure 2.5b.

The current source represents the illumination-induced generated and extracted charge carrier flow, in the *J/V* characteristic it determines the intersection point of the curve with the *J*-axis and shifts the complete curve towards negative currents for increasing irradiance. The diodes determine the "dark" characteristic in unlighted state and therefore the behavior of the curve between $V = 0$ and $V = V_{oc}$ by their "ideality factors" n_1 and n_2 [31, 32]. The resistances describe contact, junction and sheet resistances (R_s) as well as short-circuits (R_p), which are also called "shunts". They influence the slope of the *J/V* curve at low voltages (R_p) and around V_{oc} (R_s).

[1]To compare solar cells of different sizes, usually the current density *J* is used instead of the absolute current *I*; *J* is calculated by $J = I/A$ with the cell area *A*.

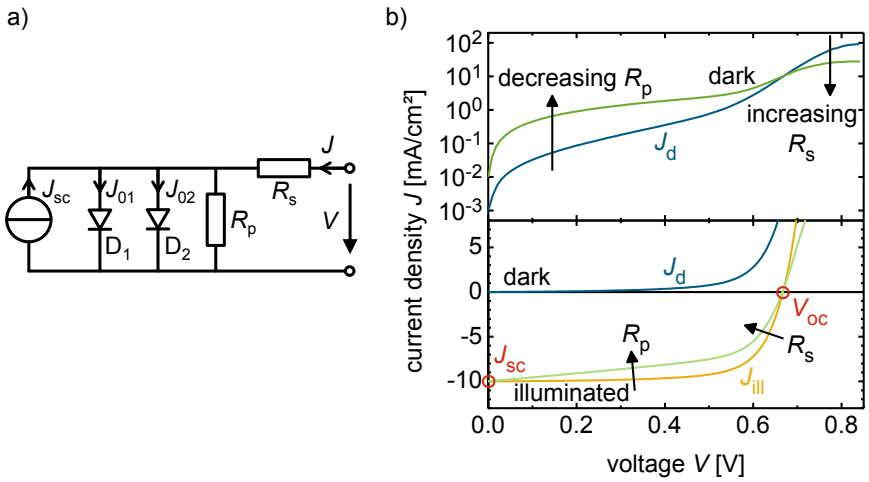

Figure 2.5: Equivalent circuit of a solar cell and its current/voltage (J/V) characteristic. a) Two diode model of a solar cell. J_{sc} models the current induced by illumination, the diodes D_1 and D_2 the diffusion and the recombination currents. R_s describes contact/sheet resistances and R_p short circuits. b) J/V characteristics in unilluminated (dark) and illuminated case. R_p influences the characteristic at low voltages, letting higher parasitic currents pass, the lower the value of R_p is. The influence of a raising value of R_s reduces the overall current at voltages over V_{oc}.

Due to the appearance of R_s, J cannot be calculated explicitly, but the curve can be given in the recursive form

$$J = J_{01}\left(e^{\frac{V+JR_s}{n_1 V_T}} - 1\right) + J_{02}\left(e^{\frac{V+JR_s}{n_2 V_T}} - 1\right) + \frac{V + JR_s}{R_p} - J_{sc} \tag{2.1}$$

with J_{01} and J_{02} being the dark saturation currents, and the thermal voltage $V_T = kT/q$ including the Boltzmann constant k, Temperature T and elementary charge q. If no illumination is applied, the contribution of $J_{sc} = 0$, leading to the dark current density

$$J_{dark} = J_{01}\left(e^{\frac{V+J_{dark}R_s}{n_1 V_T}} - 1\right) + J_{02}\left(e^{\frac{V+J_{dark}R_s}{n_2 V_T}} - 1\right) + \frac{V + J_{dark}R_s}{R_p}. \tag{2.2}$$

With illumination, the illuminated current density J_{ill} is calculated by

$$J_{ill} = J_{01}\left(e^{\frac{V+J_{ill}R_s}{n_1 V_T}} - 1\right) + J_{02}\left(e^{\frac{V+J_{ill}R_s}{n_2 V_T}} - 1\right) + \frac{V + J_{ill}R_s}{R_p} - J_{sc}. \tag{2.3}$$

The difference between both current is called photo current density

$$J_{ph} = J_{ill} - J_{dark}, \tag{2.4}$$

which equals J_{sc} in most cases. This does not hold for thin film silicon solar cells as will be explained in chapter 2.3.

Usually, the integral treatment of defects appearing as R_s or R_p is insufficient, as they locally vary. Especially shunts are often strongly localized in small areas. This makes it interesting to find two- and three-dimensional models for the description of solar cells and to compare them to spatially resolved measurements. Some quantities can be measured using scanning techniques like Corescan [33], laser-beam induced current (LBIC) [34, 35, 36, 37], or solar cell local characterization (CELLO) [38]; some can be imaged with electro- or photoluminescence and thermography [39, 40, 41, 42, 43]. With the help of these analysis methods, it is possible to locate defects (see chapter 4.1) and – with a profound knowledge – to quantify them.

The connection of solar cells to modules complicates the electrical and mathematical description as the parameters increase almost proportional to the number of connected cells. Usually they are connected in series (summing up the voltages of the cells) to so-called strings, which sometimes are combined in parallel. The more the cells are alike, the easier it is to model the module. Additionally, generating a similar current in all series connected cells increases the module's efficiency. The current limitation in series connection can lead to a deterioration of the module performance when single cells generate less current (due to defects or shading). The voltage of a "bad" solar cell in a module can even be reversed [44] at low irradiance or low voltage. This effect is further investigated in chapter 4.5. A reverse-biasing on a solar cell induces new defects due to local breakdown sites [45] that constantly reduce the cell's efficiency. The influence of such a reverse biasing on thin film silicon solar cells is shown in chapter 4.5. It is not feasible to avoid all reverse-biasing with so-called bypass diodes, especially not for thin film modules with their integrated series connection. Thus, a better knowledge of the conditions in which reverse-biasing of single cells in a module occur, can lead to new ideas for its prevention.

2.3 Differences to crystalline wafer solar cells

Most literature on solar cells refers to crystalline silicon solar cells. Term definitions and models, e.g. for defects, have been taken over and adapted to other solar cell technologies. Since there are many differences between the solar cell technologies, the adaption should always be treated with caution to avoid errors. This chapter introduces

important differences between crystalline solar cells and thin film silicon solar modules have to be considered for the investigations in this thesis.

The energy conversion efficiency of crystalline silicon solar cells is about twice as high (ca. 25 %), even though crystalline silicon is an indirect absorber while amorphous silicon acts like a direct band gap absorber. Crystalline silicon wafers are in p/n-configuration, see Fig. 1.6a, the absorber is much thicker (100x). No built-in electrical field spreading over the absorbing layer is needed, as charge carriers diffuse over a concentration gradient to the junction. This is possible because of the high mobility of the charge carriers in crystalline silicon. This enables a simple charge carrier separation at the p/n junction, where a p-doped silicon layer and an n-doped silicon layer are in direct contact [30, p. 120]. The lack of a field over the absorbing layer implies a voltage-independent photocurrent J_{ph} and a high fill factor *FF* of the *J/V* characteristic. In contrary, in thin film silicon solar cells the charge carriers have a low mobility and are separated and extracted by an electric field over the whole thickness of the main absorbing i layer. The thick intrinsic layer is embedded between two thin doped layers, p and n. This leads to a constant force on the carriers to drift towards the contacts as illustrated in Figure 2.6b.

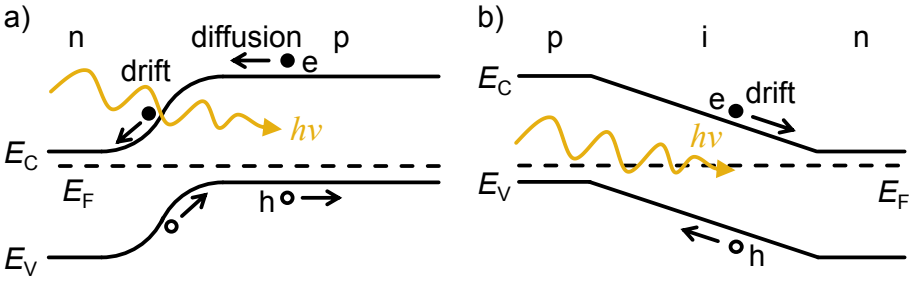

Figure 2.6: Band diagrams of p/n *and* p/i/n *junction devices under illumination. a) In* p/n *junction solar cells (e.g. crystalline silicon solar cells), the base is usually the several hundred* µm *thick* p*-doped wafer. The* 100 nm *thin emitter* n*-layer faces the illumination, since most photons are absorbed in the base. Electrons have a higher mobility than holes which makes a* p *layer advantageous over an* n *layer. The electrons diffuse towards the* p/n *junction, where the built-in electric field forces them to drift into the* n *region. b) Solar cells with* p/i/n *junction (e.g. a-Si, µc-Si solar cells) use the electric field over the whole device to force the electron/hole pairs to separate and to drift to the opposing contacts. Such junction devices are used if the mobilities of charge carriers are very low in a material. The* p *layer faces the illuminated side to ensure a shorter way to the contact for the less mobile holes.*

The electric field makes the photocurrent J_{ph} strongly voltage dependent, as a bias voltage reduces the electric field and therefore limits the carrier extraction at high voltages. This leads to a poor *FF* of the *J/V* characteristic and therefore a lower efficiency. Furthermore, this leads to the fact, that the description of thin film silicon solar cells with the above shown two diode model is not sufficient. The model cannot connect J_{ph} with *V*. Hence, thin film silicon solar cells need to be modeled with simulations as described in references [46, 47, 48, 49, 50].

When comparing imaging investigations of crystalline and thin film silicon solar cells/modules, the geometry of both sample types has to be regarded. The current in crystalline solar cells flows laterally in little areas between the front contact grid fingers, but mostly in *z*-direction (depth). In thin film silicon modules, the current flow divides in a lateral component (see next chapter 2.4) over the width of the cell stripes and a further component in depth direction. Therefore, e.g. the interpretation of series resistances differs, as the definition in crystalline solar cells is not that clear. There, the current flows from the back contact metal, which is extended over the whole device over the junction to the front grid fingers. If this series resistance is measured in a lateral resolution, it is not clear to which contact the resistance values in between the fingers refer to. In contrary, thin film solar modules (not restricted to silicon thin film modules) show a strong series resistance effect laterally between the contacts of a cell. This will be discussed in detail in chapter 4.3.

The different production processes for the two silicon based technologies induce different defects, e.g. shunts. Whereas shunts in crystalline silicon solar cells can have several origins inducing a specific electrical behavior [51] depending on the production steps used; shunts in thin film solar cells usually show to have the same origin: a direct short circuit between the front and back contact due to missing absorber layer. This phenomenon is investigated in chapter 4.4. Another type of shunt can occur at the series interconnection of thin film solar cells, which is not present in crystalline silicon solar cells (see chapter 4.5). Series resistance issues in crystalline silicon solar cells are often related to a bad contact between the emitter layer and the grid fingers above [52]. In thin film silicon solar modules, a bad contact or bad adhesion between an absorber layer and a TCO layer enhances series resistance as well as a low conductivity of the front TCO. Furthermore, a bad bonding of front- and back contact in the module series connection line P_2 can increase R_s, too. In conclusion, the comparison of resistance related defects must be accompanied by a good understanding of the structural differences between these solar cell technologies.

2.4 Origin of heat dissipation in silicon p/i/n-solar modules

Generally, after Joule's law, a current flow in a solid with a certain resistivity leads to a power dissipation in form of heat. The dissipated power per unit area equals the flowing current density multiplied with the applied voltage, $p = U \times J = R_{\blacksquare} \times J^2$. That means, every areal resistance $R_{\blacksquare}$ will induce heat dissipation and will therefore be visible in LIT. In a shunt, e.g., the voltage breaks down to a certain level and the current density is much higher than in the surrounding. This can lead to high dissipated power densities in shunts. A distribution of series resistance in a layer leads to a characteristic current flow distribution depending on where the current is injected. Both effects can be seen in LIT images and will be discussed in chapter 4.3. As the power dissipation is related to flowing currents, Figure 2.7 illustrates the current paths expected in thin film solar modules in a cross view sketch of one cell stripe.

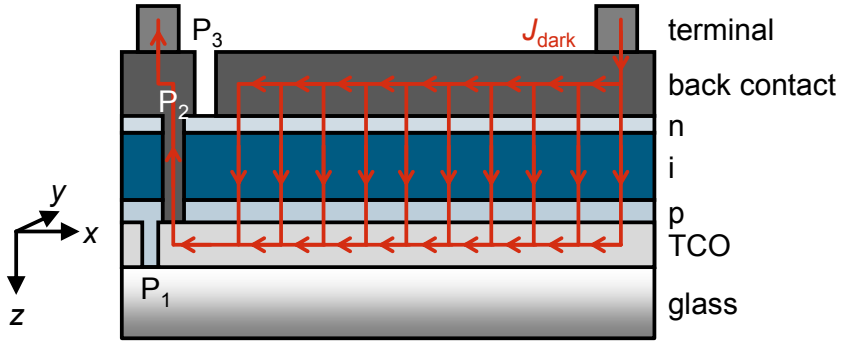

Figure 2.7: Current flow in a thin film silicon solar module. A dark current J_{dark} induced by an applied voltage V flows through the back contact into the absorber and is extracted over the integrated series connection. The current directions divide in a lateral current flow J(x) – mainly in -x direction – in the contact layers and a "depth" current flow J(z) in the absorber. The photocurrent flow J_{ph} is opposed to J_{dark} and is thus directed in x direction in the contact layers and in -z direction in the absorber.

The current in solar cells is a superposition of different current flows that are opposed and therefore partly balance each other out depending on the prevalent conditions. They are influenced by the applied voltage and illumination. In the following, three different points of interest will be discussed to clarify the respective currents and heat dissipation mechanisms. Figure 2.8 illustrates the band diagram of a p/i/n device at following conditions: a) $V > V_{oc}$, no illumination, b) $V = 0$, $J = J_{sc}$ with illumination and c) $V = V_{oc}$ with illumination.

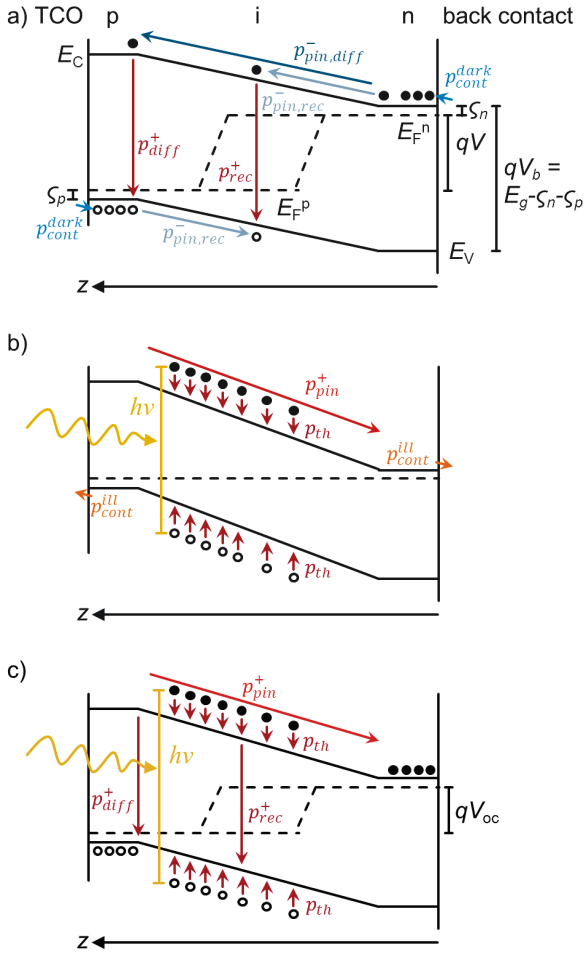

Figure 2.8: Heat dissipation and transport mechanisms in a p/i/n *solar cell. The scheme shows a band diagram at several idealized points of interest: a) The solar cell is biases with $V > V_{oc}$ without illumination. The applied voltage decreases the barrier and splits the Fermi levels of electrons and holes. This enables recombination and diffusion current flow. Injected charge carriers consume thermal energy on their way up the barrier. When recombining, they lose energy, leading to a heating of the material. b) The solar cell is illuminated and short-circuited at J_{sc}. All generated charge carriers move down the barrier releasing their kinetic energy. Further heating occurs under illumination due to thermalization, i.e. photon with higher energies than the band gap transfer the energy difference $h\nu$-E_g to the lattice. c) The solar cell is illuminated and left in open circuit, thus no net current flow occurs. This leads to charge collection at the contacts that builds up V_{oc}. The amount of dissipated heat is the equals the one in case (b).*

In the following, I consider the internal heat dissipation mechanisms at one point x_0, y_0 of a p/i/n solar cell. The description follows the one given in [6, p. 44] for p/n solar cells. Hereby, the complexity of p/i/n cells is greatly reduced for a clear description. Thus, equation (2.1) is used for the analytical description of a p/i/n cell in awareness of its inaccuracy in the description of the photocurrent J_{ph}. An analytical description of the *J/V* characteristic of p/i/n cells is not possible, but it can be approximated with analytical equations [53, 54]. An adequate description of p/i/n cells can only be given by numerical simulations [20, p. 501].

As a further simplification, no resistances are considered, reducing equation (2.1) by leaving out all resistance terms to

$$J = J_{01}\left(e^{\frac{V}{n_1 V_T}} - 1\right) + J_{02}\left(e^{\frac{V}{n_2 V_T}} - 1\right) - J_{sc}. \tag{2.5}$$

a) The flowing current J equals the diode currents and is dominated by the diffusion current $J_{diff} = J_{01}\left(e^{V/n_1 V_T} - 1\right)$ (see Figure 2.5b). This is the dark current $J = J_{dark}$. It flows over the back contact through the absorber layer – overcoming the barrier as a diffusion current due to the huge amount of injected charge carriers – then over the front TCO and the P_2 line to the terminal back to the voltage source as shown in Figure 2.7. The current flows laterally in the contact layers, especially in -*x* direction. The current over the absorber layer is only directed in *z* direction, as there is no attraction for it to flow laterally. When acquiring an image of the surface of the module with a LIT system (only seeing *x* and *y* direction), one sees an overlap of the lateral current flow and the flow in *z* direction. That means, e.g. local series resistances between the contact and absorber layers (due to bad adhesion, e.g.) and lateral sheet resistances, especially in the TCO layer, cannot be separated in *z* direction with an LIT setup and will be seen as a superposition[2].

   The superposition of all heat dissipation and transport mechanisms are illustrated in Figure 2.8a. The entire flowing current J_{dark} is divided into the diffusion current J_{diff} and the recombination current $J_{rec} = J_{02}\left(e^{V/n_2 V_T} - 1\right)$. In the band diagram, they can be seen as an electron current flow from the n side and a hole current flow from the p side. The charge carriers of the diffusion current J_{diff} recombine in the p region, since the diffusing electrons had the energy to overcome the barrier height $q(V_b\text{-}V)$, with V_b being the built-in voltage of the p/i/n-junction, V the applied voltage, and q the elementary charge. The charge carriers

[2] The signal induced by the sheet resistance layer is a well-known pattern where deviations are apparent (see chapter 3.5), i.e. with an advanced technique, a separation of the effects could possibly be calculated.

of the recombination current J_{rec} recombines in the i-layer of the solar cell via the Shockley-Read-Hall (SRH) mechanism as these electrons do not have enough energy to overcome the barrier. Both currents induce heat generation and cooling beginning with their joint injection at the contacts. All electrons coming from the back contact consume energy to reach the n layer. They need to overcome the difference of the Fermi level E_F^n to the conduction band E_C, i.e. $\varsigma_n = E_C - E_F^n$, and accelerate to a certain kinetic energy ε_e^n (which is a mean kinetic energy for all flowing electrons). The same happens with the holes at the TCO-p contact[3]; they consume the energy difference between the Fermi level E_F^p and the valence band E_V, i.e. $\varsigma_p = E_F^p - E_V$ and the mean kinetic energy ε_h^p. In total, the current flow over the contacts induces a thermal heating power of

$$p_{\mathrm{cont}}^{\mathrm{dark}} = -\frac{J_{\mathrm{diff}} + J_{\mathrm{rec}}}{q}\left(\varepsilon_e^n + \varsigma_n + \varepsilon_h^p + \varsigma_p\right). \tag{2.6}$$

The power dissipation mechanisms of the currents flowing over the p/i/n junction can be divided in two parts for J_{diff} and J_{rec} each. The diffusing electrons need thermal energy to overcome the barrier height of $q(V_{\mathrm{b}}\text{-}V)$. Hence, their flow over the barrier is a Peltier cooling effect with the power

$$\begin{aligned} p_{\mathrm{pin,diff}}^{-} &= -\frac{J_{\mathrm{diff}}}{q}\left(qV_{\mathrm{b}} - qV + \varepsilon_e^p - \varepsilon_e^n\right) \\ &= -\frac{J_{\mathrm{diff}}}{q}\left(E_{\mathrm{g}} - \varsigma_n - \varsigma_p - qV + \varepsilon_e^p - \varepsilon_e^n\right), \end{aligned} \tag{2.7}$$

where ε_e^p is the mean kinetic energy of the electrons in the p layer. The term $\varepsilon_e^n - \varepsilon_e^p$ (taking the minus sign outside the parenthesis into account) corresponds to the difference of the mean kinetic energies of the electrons in the n and p layer. This kinetic energy loss is released and counts opposing to the overcoming of the barrier height. After reaching the p layer, the electrons recombine with holes releasing the band gap energy E_{g} and their kinetic energies $p_{\mathrm{diff}}^{+} = E_{\mathrm{g}} + \varepsilon_e^p + \varepsilon_h^p$ as heat. Hence, the heat balance of J_{diff} in the absorber layer is

[3] Here, the complexity of the TCO-p contact is neglected. The TCO-p contact is matter of ongoing research.

$$\begin{aligned} p_{\text{diff}} &= p_{\text{diff}}^{+} + p_{\text{pin,diff}}^{-} \\ &= \frac{J_{\text{diff}}}{q}\left(E_{\text{g}} + \varepsilon_e^p + \varepsilon_h^p - E_{\text{g}} + \varsigma_n + \varsigma_p + qV - \varepsilon_e^p + \varepsilon_e^n\right) \\ &= \frac{J_{\text{diff}}}{q}\left(qV + \varepsilon_e^n + \varsigma_n + \varepsilon_h^p + \varsigma_p\right). \end{aligned} \tag{2.8}$$

A similar treatment of the recombination current J_{rec} over the i layer leads to its Peltier cooling contribution

$$\begin{aligned} p_{\text{pin,rec}}^{-} &= -\frac{J_{\text{rec}}}{q}\left(qV_{\text{b}} - qV - \varepsilon_e^n - \varepsilon_h^p\right) \\ &= -\frac{J_{\text{rec}}}{q}\left(E_{\text{g}} - \varsigma_n - \varsigma_p - qV - \varepsilon_e^n - \varepsilon_h^p\right). \end{aligned} \tag{2.9}$$

Electrons and holes have to get to the same z position, therefore their summed up movement overcomes the barrier height. Their kinetic energy is dissipated as heat and counterbalances the Peltier cooling. The energy released by their recombination per electron/hole pair is E_{g}, as at the recombination event, all their kinetic energy is used up. Thus, the heat balance of the recombination current is

$$\begin{aligned} p_{\text{rec}} &= \frac{J_{\text{rec}}}{q}\left(E_{\text{g}} - E_{\text{g}} + \varsigma_n + \varsigma_p + qV + \varepsilon_e^n + \varepsilon_h^p\right) \\ &= \frac{J_{\text{rec}}}{q}\left(qV + \varepsilon_e^n + \varsigma_n + \varepsilon_h^p + \varsigma_p\right). \end{aligned} \tag{2.10}$$

The sum of all heat balances for the dark current

$$J_{\text{dark}} = J_{\text{diff}} + J_{\text{rec}} \tag{2.11}$$

relates to the overall generated heat

$$
\begin{aligned}
p_{\text{dark}} &= p_{\text{diff}} + p_{\text{rec}} + p_{\text{contacts}} \\
&= \frac{J_{\text{diff}}}{q}\left(qV + \varepsilon_e^n + \varsigma_n + \varepsilon_h^p + \varsigma_p\right) \\
&\qquad + \frac{J_{\text{rec}}}{q}\left(qV + \varepsilon_e^n + \varsigma_n + \varepsilon_h^p + \varsigma_p\right) \\
&\qquad - \frac{J_{\text{diff}} + J_{\text{rec}}}{q}\left(\varepsilon_e^n + \varsigma_n + \varepsilon_h^p + \varsigma_p\right) \\
&= (J_{\text{diff}} + J_{\text{rec}})V \\
&= J_{\text{dark}}V. \qquad (2.12)
\end{aligned}
$$

Hence, this detailed analysis comes to the conclusion that the dissipated power in the solar cell at dark conditions simply depends on the applied voltage V and the flowing current J_{dark}. It should be noted, that all these power losses occur approximately in one diffusion length of the charge carriers L_{D}, therefore the lateral resolution of the power dissipation in x and y direction is L_{D}. Literature values for L_{D} are about < 0.2 µm [55, 56] and the lateral resolution of commercially available LIT systems is several µm per pixel (highest resolution at IEK-5: 4.8 µm/pixel). So in general it can be said, that the recording of thin film solar cells with LIT at dark conditions shows power losses at the site of their origin.

b) In case a), the flowing electrons and holes came from the electrical injection. In case b), the outer electrical influence is cancelled by short-circuiting the device, leading to a voltage $V = 0$. By applying an illumination, electrons and holes emerge from the impinging of photons. They induce a photo current J_{ph} that is opposed to the dark current J_{dark} just along the electric field of the solar cell. At $V = 0$, $J_{\text{dark}} = 0$ and therefore only $J_{\text{ph}} = J_{\text{sc}}$ flows. The acceleration of electrons along the i-layer leads to a heating as they lose the barrier height energy to phonons. This heat contribution is given generally by

$$
\begin{aligned}
p_{\text{pin}}^{+} &= \frac{J_{\text{ph}}}{q}\left(qV_{\text{b}} - qV - \varepsilon_h^p - \varepsilon_e^n\right) \\
&= \frac{J_{\text{ph}}}{q}\left(E_{\text{g}} - \varsigma_n - \varsigma_p - qV - \varepsilon_h^p - \varepsilon_e^n\right). \qquad (2.13)
\end{aligned}
$$

and in this case of $J_{\text{ph}} = J_{\text{sc}}$, by $p_{\text{pin}}^{+,J_{\text{sc}}} = J_{\text{sc}}/q \times \left(E_{\text{g}} - \varsigma_n - \varsigma_p - \varepsilon_h^p - \varepsilon_e^n\right)$. The kinetic energies $\varepsilon_h^p + \varepsilon_e^n$ – that holes have left when reaching the p layer and electrons in the n layer – correspond to cooling as they are not converted into heat.

A second heating mechanism not known from the dark condition arises under illumination, which is thermalization. All photons impinging with a higher energy $h\nu$ than the band gap E_g will relax towards the band edges in a very short time of less than 1 picosecond. This leads to a general heating contribution of the thermalization

$$p_{\mathrm{th}} = \frac{J_{\mathrm{sc}}}{q}\left(h\nu - E_{\mathrm{g}}\right) \tag{2.14}$$

or $p_{\mathrm{th}}^{J_{\mathrm{sc}}} = J_{\mathrm{sc}}/q \times \left(h\nu - E_{\mathrm{g}}\right)$ in case b). Considering the power dissipation at the contacts $p_{\mathrm{cont}}^{\mathrm{ill}}$, it is reversed compared to dark conditions leading to a power per unit area of

$$p_{\mathrm{cont}}^{\mathrm{ill}} = \frac{J_{\mathrm{ph}}}{q}\left(\varepsilon_e^n + \varsigma_n + \varepsilon_h^p + \varsigma_p\right) \tag{2.15}$$

and $p_{\mathrm{cont}}^{\mathrm{ill},\,J_{\mathrm{sc}}} = J_{\mathrm{sc}}/q \times \left(\varepsilon_e^n + \varsigma_n + \varepsilon_h^p + \varsigma_p\right)$. With that, the additional heat generation and cooling balance of the illumination sums up to

$$\begin{aligned} p_{\mathrm{ill}}^{\mathrm{add}} &= p_{\mathrm{pin}}^{+} + p_{\mathrm{th}} + p_{\mathrm{cont}}^{\mathrm{ill}} \\ &= \frac{J_{\mathrm{ph}}}{q}\left(E_{\mathrm{g}} - \varsigma_n - \varsigma_p - qV - \varepsilon_h^p - \varepsilon_e^n\right) \\ &\qquad + \frac{J_{\mathrm{ph}}}{q}\left(h\nu - E_{\mathrm{g}}\right) \\ &\qquad + \frac{J_{\mathrm{ph}}}{q}\left(\varepsilon_e^n + \varsigma_n + \varepsilon_h^p + \varsigma_p\right) \\ &= \frac{J_{\mathrm{ph}}}{q}\left(h\nu - qV\right) \end{aligned} \tag{2.16}$$

and in case b), $p_{\mathrm{ill}}^{\mathrm{add},\,J_{\mathrm{sc}}} = J_{\mathrm{sc}}\, h\nu/q$. The overall general balance is thus

$$\begin{aligned} p_{\mathrm{ill}} &= p_{\mathrm{dark}} + p_{\mathrm{ill}}^{\mathrm{add}} \\ &= J_{\mathrm{dark}}V + \frac{J_{\mathrm{ph}}}{q}\left(h\nu - qV\right) \end{aligned} \tag{2.17}$$

and $p_{\mathrm{ill}}^{J_{\mathrm{sc}}} = p_{\mathrm{ill}}^{\mathrm{add},\,J_{\mathrm{sc}}} = J_{\mathrm{sc}}\, h\nu/q$, respectively. Obviously, at J_{sc} with illumination, all power that is dissipated just depends on J_{sc} (and with that, the irradiance) and

the wavelength for the incoming photons. An example of the quantitative share of power dissipating heat mechanisms in a thin film solar module illuminated by a light emitting diode (LED) panel is given in chapter 4.6.

c) The last case describes a solar cell with illumination at V_{oc}. Here, all above mechanisms are combined: there is no current flow outside the device, all currents and therefore all recombination processes occur just inside the solar module. In a module, however, it is imaginable that there are current paths along the connected cells; these currents are not regarded in this case study. Thus, as all charge carriers are generated by photon absorption and are not extracted, they have to recombine somewhere. They are comparably free to move laterally as no current direction is induced (except e.g. due to shunts). Still, the overall dissipated energy has to be as large as in the case of J_{sc}. This can be derived from the synopsis of the heat processes occurring in this case, which are p_{th}, p_{pin}^{+}, and $p_{diff} + p_{rec}$. The net current flow at the contacts is zero, $J_{ill} = J_{ph} - J_{dark} = 0$, but the internal current flow due to recombination is

$$J_{ph} = J_{dark} = J_{sc}. \tag{2.18}$$

Therefore, the power dissipation at V_{oc} is according to equations (2.8), (2.10), (2.11), (2.13), and (2.14)

$$\begin{aligned} p_{ill}^{V_{oc}} &= p_{th} + p_{pin}^{+} + p_{diff} + p_{rec} \\ &= \frac{J_{sc}}{q}\left(h\nu - E_g\right) + \frac{J_{sc}}{q}\left(E_g - \varsigma_n - \varsigma_p - qV - \varepsilon_h^p - \varepsilon_e^n\right) \\ &\qquad + \frac{J_{sc}}{q}\left(qV + \varepsilon_e^n + \varsigma_n + \varepsilon_h^p + \varsigma_p\right) \\ &= J_{sc}\frac{h\nu}{q} \\ &= p_{ill}^{J_{sc}} \end{aligned} \tag{2.19}$$

Obviously, the total power dissipation at V_{oc} conditions is the same as in J_{sc} conditions. But this is only valid for the integral power dissipation of a whole device. As explained above, there are still differences due to lateral currents, therefore the results at a certain position x_0, y_0 cannot be compared without knowing the surrounding and the overall power dissipation in both cases. The differences between an LIT measurement at V_{oc} and at J_{sc} conditions under illumination are shown in chapter 4.6.

The above discussion was dedicated to the overall dissipated power density at J_{sc}, V_{oc}, and in dark conditions. Under illumination and an applied voltage between $V = 0$ and $V = V_{oc}$, a certain power density is dissipated in an external load. It can be calculated by

$$\begin{aligned} p_{ext} &= p_{ill}^{V_{oc}} - p_{ill}(V) \\ &= p_{ill}^{I_{sc}} - p_{ill}(V) \\ &= J_{sc}\frac{h\nu}{q} - J_{dark}V - \frac{J_{ph}}{q}(h\nu - qV) \\ &= (J_{sc} - J_{ph})\frac{h\nu}{q} + (J_{ph} - J_{dark})V. \end{aligned} \tag{2.20}$$

In the further thesis, I refer to $p_{ill}^{I_{sc}} = p_{ill}^{V_{oc}}$ as p_{in}, which is a valid assumption in a model of a solar cell/module for an internal quantum efficiency (IQE) and an absorption a of 1, respectively. I refer to the power density $p_{ill}(V)$ as dissipated power density $p_d(V)$, which is the power measured by thermography. This transforms equation (2.20) to

$$p_{ext} = p_{in} - p_d(V) \tag{2.21}$$

As mentioned above, a quantitative example for these power dissipations in a thin film solar module is shown in chapter 4.6. For the dissipated power density in the dark (case (a)),

$$p_d(V) = p_{dark} = J_{dark}V \tag{2.22}$$

holds. Equations (2.21) and (2.22) both hold for integral powers also, namely

$$P_{ext} = P_{in} - P_d(V) \tag{2.23}$$

and

$$P_d(V) = P_{dark} = I_{dark}V. \tag{2.24}$$

3 Lock-in Thermography on thin film solar cells and modules

This chapter describes all acquisition steps of lock-in thermography imaging of thin film solar cells. Beginning with the detection of infrared radiation, the chapter guides through the general lock-in principle and the inherent error sources. Simulations of the lock-in process are discussed, asking for the limitations of the process and how a reliable signal reconstruction can be carried out.

3.1 Infrared radiation and its detection with thermography

Heat transfer between two media can occur in three different modes: conduction, convection, and radiation. The latter mode, radiation, allows contactless and therefore non-destructive testing (NDT) of devices [57]. Lock-in thermography of electronic devices such as solar cells or integrated circuits (ICs) is an advanced NDT technique, even enabling a quantitative analysis. However, to avoid misinterpretations of LIT images, it is necessary to be familiar with some radiometric quantities that are the basis of infrared imaging.

In the following, two categories of radiometric quantities will be regarded: Total quantities that result from an integration over the entire spectrum; and spectral quantities, which consider a certain wavelength interval. Every body or medium at temperature T higher than the absolute zero contains a certain amount of energy that it releases through "thermal" radiation. The theoretical case of an ideal radiation characteristic is called a "black body". It absorbs radiation of all frequencies of the electromagnetic spectrum completely. After Kirchhoff's law of thermal radiation, the absorption α equals the emissivity ε,

$$\alpha = \varepsilon. \tag{3.1}$$

Evidently, a black body emits the maximal possible radiant power Φ at a given temperature. Usually, Φ is given per unit area A for a normalized consideration. The emitted power is called the radiant emittance M, the received power irradiance E, respectively. According to the Stefan-Boltzmann law, the emittance of a black body depends only on its temperature T and is calculated by

$$M^{\mathrm{bb}} = E^{\mathrm{bb}} = \frac{d\Phi}{dA} = \sigma T^4 \tag{3.2}$$

with the Stefan-Boltzmann-Constant $\sigma = 5.67 \times 10^{-8} \frac{\mathrm{W}}{\mathrm{m^2 K^4}}$.

The emittance M^{bb} of a black body is the same in all space directions, i.e. absolutely diffuse. Its dependency on the wavelength interval $d\lambda$ per spherical angle $d\Omega$ is called spectral power density L_λ^{bb} and is described by Planck's law as

$$L_\lambda^{\mathrm{bb}} = \frac{dM}{d\Omega d\lambda} = \frac{d^3\Phi}{dA d\Omega d\lambda} = \frac{2hc^2}{\lambda^5} \frac{1}{e^{hc/\lambda kT} - 1} \tag{3.3}$$

with Planck's constant h, the speed of light c, and the Boltzmann constant k. Equation (3.3) is visualized in Figure 3.1 showing the spectral power density L_λ^{bb} for different temperatures T over the wavelength range from 0.06 µm < λ < 100 µm.

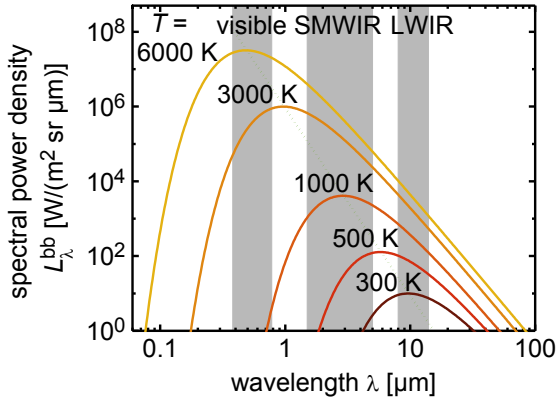

Figure 3.1: Spectral power density of the black body radiation for different temperatures according to Planck's law. The maxima shift with decreasing temperature to higher wavelengths according to Wien's displacement law. For a black body at T = 6000 K*, which is about the sun's surface temperature, the maximum power density lies in the visible spectrum range. At about room temperature, the maximum lies at* 10 µm *in the long wave infrared (LWIR) range. In the short and mid wave infrared (SMWIR) range, the emission of a black body at room temperature is still detectable. Thermographic or infrared cameras use these spectrum ranges for the detection of heat.*

The yellow curve in Figure 3.1 represents L_λ^{bb} at 6000 K, which is about the temperature of the sun's surface. Its maximum lies at around λ_{max} = 0.5 µm. With decreasing temperature, the maxima shift to higher wavelengths according to Wien's displacement law, which is marked by the green dotted line. According to the displacement law, the maxima follow the relation

$$\lambda_{max} = \frac{2897.8\ \mu mK}{T}. \tag{3.4}$$

For room temperature at about 300 K, λ_{max} lies at almost 10 µm. This is in the wavelength range called long wave infrared (LWIR) that goes from 8 to 14 µm and is marked with the grey shading. The ranges short and mid wave infrared (SWIR: 1 to 2.5 µm, MWIR: 3 to 5 µm) are marked with a joint gray shading. Detectors of thermographic cameras are matched to be sensitive in these wavelength ranges. The definitions of the infrared spectral ranges are derived from the radiation transmittance τ of the atmosphere depicted in Figure 3.2. Especially water (H_2O) and carbon dioxide (CO_2) absorb in several wavelengths leaving wavelength "windows" for the detection of infrared radiation.

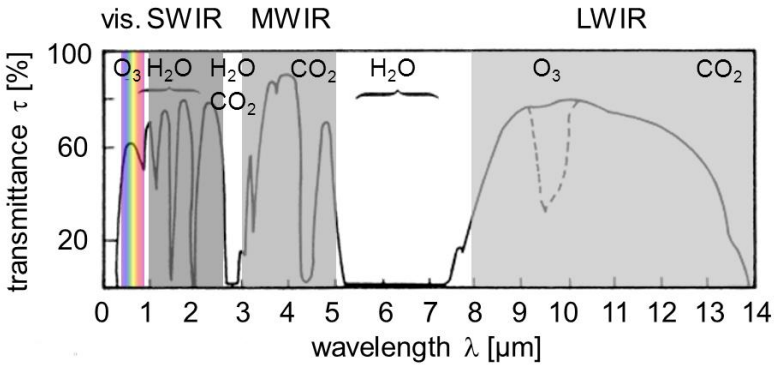

Figure 3.2: Transmittance of the atmosphere to infrared radiation. The earth's atmosphere absorbs radiation of several spectral ranges, especially due to water and carbon dioxide molecules. The spectral "windows" that are left for the detection of infrared radiation are summarized as SWIR from 1 *to* 2.5 µm*, MWIR from* 3 *to* 5 µm *and LWIR from* 8 *to* 14 µm*.*

The transmittance τ of radiation is, together with the reflectance ρ and the absorptance α defined by

$$\alpha + \rho + \tau = 1, \tag{3.5}$$

i.e. the shares of absorptance, reflectance, and transmittance have to be the sum of all incoming radiation to a body. All these radiative parameters are material properties. For a black body, $\alpha = 1$ holds and therefore $\rho = \tau = 0$. In equation (3.5), the radiative parameters are treated integrally over the spectrum. For most materials, they are not constant over the wavelength range and equation (3.5) then reads $\alpha_\lambda + \rho_\lambda + \tau_\lambda = 1$, and is

valid for restricted wavelength ranges only. Equation (3.1) shows integral parameters, so a more exact formulation is

$$\int \alpha_\lambda \, d\lambda = \int \varepsilon_\lambda \, d\lambda. \tag{3.6}$$

This illustrates that the emissivity ε has several definitions depending on which criteria have to be considered. Generally, it is defined as the ability of a body to emit radiation in comparison to the perfect emitter, the black body. So the total hemispherical emissivity is defined as

$$\varepsilon = \frac{M}{M^{\mathrm{bb}}}, \tag{3.7}$$

the spectral hemispherical emissivity as

$$\varepsilon_\lambda = \frac{M_\lambda}{M_\lambda^{\mathrm{bb}}}, \tag{3.8}$$

and the spectral directional emissivity as

$$\varepsilon'_\lambda = \frac{L_\lambda}{L_\lambda^{\mathrm{bb}}}. \tag{3.9}$$

For some materials, $\alpha \neq \varepsilon$ can be valid for certain wavelength ranges as well as totally. It holds for materials that are oriented (not diffuse) emitters also. Well-known examples are metals such as polished chromium with and absorptance of the sun's irradiance of $\alpha = 0.4$ and a total hemispherical emissivity at 300 K of $\varepsilon = 0.07$; or polished gold with $\alpha = 0.29$ and $\varepsilon = 0.0026$. In the evaluations of this thesis, I will consider the investigated samples as diffuse emitters and thus, the total hemispherical emissivity ε according to equation (3.7).

According to equations (3.7) and (3.2), the measurable irradiance E^{meas} that an infrared camera detects is

$$E^{\mathrm{meas}} = \varepsilon M^{\mathrm{bb}} = \varepsilon \sigma T^4. \tag{3.10}$$

This means, a detected irradiance is always the product of the measured material's emissivity and its temperature (to the power of 4). This can cause misinterpretations if different materials are measured in the same image, for example. So when measuring

absolute temperatures by radiation, either a homogenous emissivity has to be ensured or an emissivity correction has to be carried out [58, 6, p. 159].

Close to room temperature, a linearization of equation (3.10) is often used. The validation of this linearization is given in chapter 3.4. Temperature differences around room temperature cause only small irradiance differences. This makes it difficult to detect small temperature differences like in electronic devices, for example. To successfully measure these temperature differences, advanced methods like the lock-in technology have to be used. Lock-in uses an active stimulus and enables the cancellation of noise and signals of other frequencies than the excitation frequency.

3.2 Lock-in signal generation

The lock-in principle is often used for the detection of small signals embedded in a noisy background. A lock-in amplifier acts like an extremely narrow-band filter, which enhances the signal-to-noise ratio (*SNR*) significantly. Historically, the invention of the lock-in amplifier is often referred to Robert Henry Dicke, who was involved in measurements of the cosmic microwave background radiation validating the Big Bang theory [59]. He used lock-in amplifiers for the development of patterns for microwave antenna feeds as well as for experiments with crystal rectifiers [60]. However, he claims not to be the inventor of lock-in amplifiers, explaining his idea was based on work of Walter C. Michels [61, 62]. Michels in turn, references several amplifiers [63, 64] with C. R. Cosens' lock-in amplifier [65] as "most suitable since very simple modifications of the circuit enable the response band to be made very narrow, provided only that the phenomena being observed remain steady for a long enough time to take readings with a long period instrument" [61]. Michels and Cosens did not use an active signal modulation, but a bridge circuit amplifier that could be adapted to a specific frequency.

Today, there are several digital realizations of lock-in amplifiers [66, 67]. Here, I focus on the standard lock-in correlation used by Breitenstein [6, p. 16] because it is used in the most commercial available LIT systems. In the standard lock-in correlation, the time-dependent excitation $E(t)$ results in a complex lock-in signal S. The excitation signal $E(t)$ causes a response signal $F(t)$ from the investigated sample. The simplest case of an excitation is a constant signal. Depending on the sample, the response signal on a constant excitation can be, e.g., a linear increase without saturation. Such a response has no distinct value and is dependent on the measurement time. Therefore it is preferable to choose a periodic signal as excitation $E(t)$. The simplest case of a periodic signal is a rectangular signal, where the excitation is periodically turned on and off. This periodicity is then found in the response signal, too. Furthermore, if the response is measured once during the excitation, once when the excitation is off and the difference of these

two states is calculated, the result will be a nearly constant signal and the background will be canceled out. This is in principle the idea of the lock-in process.

For a better understanding, I will discuss the lock-in principle with the aid of an example. I will assume a response signal *F* that has the height 1.1 when an excitation is present and 1.0 without excitation. The period of the excitation is 2π. That means, $F = \begin{cases} 1.1, & 0 \leq \phi < \pi \\ 1.0, & \pi \leq \phi < 2\pi \end{cases}$. Assuming the signal is measured once in a half period, the value of the difference, which is the actual signal without background, amounts to $S = 1.1 - 1.0 = 0.1$.

Measuring once in a half period could result in crucial errors. A phase shift between excitation and response, e.g. due to capacitive processes, could principally occur. A single measurement per half period would not detect such a phase shift. Continuous measurements can prevent such errors, implicating that *S* has to be an integral. If the lock-in signal *S* is calculated integrally over a period and is normalized to the integration time t_{int}, it amounts to $S = 1/t_{\text{int}} \int_0^{2\pi} F\, dt = (1.1\pi + 1.0\pi)/2\pi = 1.05$. Obviously, this is not correct for the chosen example. Therefore, a correlation function has to be introduced, that weights the two half periods. The simple correlation function $K = \begin{cases} 2, & 0 \leq \phi < \pi \\ -2, & \pi \leq \phi < 2\pi \end{cases}$ is known as the wide-band correlation [6, p. 15]. This leads to the definition of the lock-in signal, which is

$$S = \frac{1}{t_{\text{int}}} \int_0^{t_{\text{int}}} F(t)K(t)\, dt \tag{3.11}$$

For the above example, the resulting lock-in signal is $S = 1/t_{\text{int}} \int_0^{2\pi} FK\, dt = \frac{1}{2\pi}(1.1 \times 2 \times \pi + 1.0 \times (-2) \times \pi) = 0.1$, which is the correct value for the response to the excitation signal.

The correlation function influences the bandwidth of the lock-in procedure. A correlation with a much narrower band is the two-band correlation with the harmonic functions sine and cosine. In LIT, the minus cosine function is used instead of the cosine, as it supports positive values in the LIT results. This is due to the phase (time) delay of thermal signals to their excitation, which are mathematically *counted in the direction to negative angles*. The correlation functions in LIT are

$$K^{0^\circ} = 2\sin(2\pi f_{\text{lock-in}} t) \tag{3.12}$$

and

$$K^{-90^\circ} = -2\cos(2\pi f_{\text{lock-in}} t) = -K^{90^\circ}. \tag{3.13}$$

The angles 0° and -90° refer to the phase shift of the correlation compared to the excitation. With these two correlation functions, two signals are achieved, namely the so called “in-phase” signal

$$S^{0^\circ} = \frac{1}{t_{\text{int}}} \int_0^{t_{\text{int}}} F(t) K^{0^\circ}(t)\, dt \tag{3.14}$$

and the so called negative “quadrature” signal

$$S^{-90^\circ} = \frac{1}{t_{\text{int}}} \int_0^{t_{\text{int}}} F(t) K^{-90^\circ}(t)\, dt = -S^{90^\circ}. \tag{3.15}$$

The complex signal S can be calculated by

$$S = S^{0^\circ} - iS^{-90^\circ} = S^{0^\circ} + iS^{90^\circ}. \tag{3.16}$$

Thus, S^{0° is the real part of the complex quantity S, S^{90° the imaginary part: $S^{0^\circ} = \mathrm{Re}(S)$ and $S^{90^\circ} = \mathrm{Im}(S)$. In the following, a harmonic sine response function with the amplitude A and the phase ϕ will be regarded, i.e.

$$F(t) = A\sin(2\pi f_{\text{lock-in}} t + \phi). \tag{3.17}$$

Exemplarily, I show how S^{0° is calculated; S^{-90° works analogically. The insertion of (3.12) and (3.17) in (3.14) yields

$$S^{0^\circ} = \frac{1}{t_{\text{int}}} \int_0^{t_{\text{int}}} \left(A\sin(2\pi f_{\text{lock-in}} t + \phi) \cdot 2\sin(2\pi f_{\text{lock-in}} t) \right) dt. \tag{3.18}$$

With $\omega = 2\pi f_{\text{lock-in}}$ and the expression for the sine function as a complex number, $\sin x = \left(e^{ix} - e^{-ix}\right)/2i$, equation (3.18) can be written as

$$S^{0^\circ} = \frac{2A}{t_{\text{int}}} \int_0^{t_{\text{int}}} \left(\frac{e^{i(\omega t+\phi)} - e^{-i(\omega t+\phi)}}{2i} \cdot \frac{e^{i\omega t} - e^{-i\omega t}}{2i} \right) dt$$

$$= \frac{A}{t_{\text{int}}} \int_0^{t_{\text{int}}} \left(\frac{\left(e^{i\phi} + e^{-i\phi}\right)}{2} - \frac{e^{i(2\omega t+\phi)} + e^{-i(2\omega t+\phi)}}{2} \right) dt.$$

Substituting $\left(e^{ix} + e^{-ix}\right)/2 = \cos x$ gives

$$S^{0^\circ} = \frac{A}{t_{\text{int}}} \int_0^{t_{\text{int}}} \Big(\cos\phi - \cos(2\omega t + \phi) \Big) dt$$

$$= \frac{A}{t_{\text{int}}} \left[t\cos\phi - \frac{1}{2\omega} \sin(2\omega t + \phi) \right]_0^{t_{\text{int}}}$$

$$= A\cos\phi + \frac{A}{2\omega t_{\text{int}}} \Big(\sin\phi - \sin(2\omega t_{\text{int}} + \phi) \Big). \tag{3.19}$$

The result consists of two terms, one constant term $S^{0^\circ} = A\cos\phi$ and a time dependent term. The latter one reduces with increasing measurement time, i.e. for the limit

$$\lim_{t_{\text{int}}\to\infty} S^{0^\circ} = \lim_{t_{\text{int}}\to\infty} \left[A\cos\phi + \frac{A}{2\omega t_{\text{int}}} \Big(\sin\phi - \sin(2\omega t_{\text{int}} + \phi) \Big) \right]$$

$$= A\cos\phi \tag{3.20}$$

or for $t_{\text{int}} \gg 1/f_{\text{lock-in}} = T_{\text{lock-in}}$, respectively. This shows how noise is reduced with increasing integration time in LIT. Note that the second term in equation (3.20) decreases also with increasing lock-in frequency. In general, the second term is small compared to the first term: For $f_{\text{lock-in}} = 1$ Hz and $t_{\text{int}} = 2\pi$ (one period), e.g., its value is $0.013\,A$. Therefore, I assume in the following that

$$S^{0^\circ} = A\cos\phi \tag{3.21}$$

is fulfilled. Analogically, the expression for S^{-90° is found, namely

$$S^{-90^\circ} = A\sin\phi. \tag{3.22}$$

Equations (3.14) and (3.15) can be combined to get the original amplitude and phase of the response signal by

$$A = |S| = \sqrt{(S^{0°})^2 + (S^{-90°})^2} = \sqrt{(S^{0°})^2 + (S^{90°})^2} \tag{3.23}$$

and

$$\phi = \arg S = \begin{cases} \arctan\dfrac{-S^{-90°}}{S^{0°}}, & S^{0°} > 0 \\ \arctan\dfrac{-S^{-90°}}{S^{0°}} + \pi, & S^{0°} < 0,\ S^{-90°} \leq 0 \\ \arctan\dfrac{-S^{-90°}}{S^{0°}} - \pi, & S^{0°} < 0,\ S^{-90°} > 0 \\ \pi/2, & S^{0°} = 0,\ S^{-90°} < 0 \\ -\pi/2, & S^{0°} = 0,\ S^{-90°} > 0. \end{cases} \tag{3.24}$$

These values correspond to the absolute value and the angle of the complex number *S*. Figure 3.3 illustrates this in the complex plane. Any signal S^{φ} that has a phase shift φ, can therefore be calculated using the multiplication $S^{\varphi} = Se^{i\varphi}$. The $S^{-45°}$ signal can alternatively be calculated by $S^{-45°} = (S^{0°} + S^{-90°})/\sqrt{2}$. If no phase shift ϕ occurs, $S^{0°}$ is the carrier of the signal. This can be seen in equations (3.21) and (3.22), which become $S^{0°} = A$ and $S^{-90°} = 0$ for $\phi = 0$.

The consideration above regarded continuous signals. Yet, a digital measurement system cannot measure continuously. In the following, I will call *n* the number of frames (or images or correlation bases[4], respectively) per period. In practice, all functions are discretized and the integral of equation (3.11) transforms to the sum

$$S = \frac{1}{nN}\sum_{l=1}^{N}\sum_{m=1}^{n} K_m F_{l,m}, \tag{3.25}$$

with *N* representing the number of periods measured and *l*, *m* being the aggregate indices.

[4] A correlation base is the point of time, when the signal F_m is measured, which then is multiplied with the values of the correlation vectors $K_m^{0°}$ and $K_m^{-90°}$.

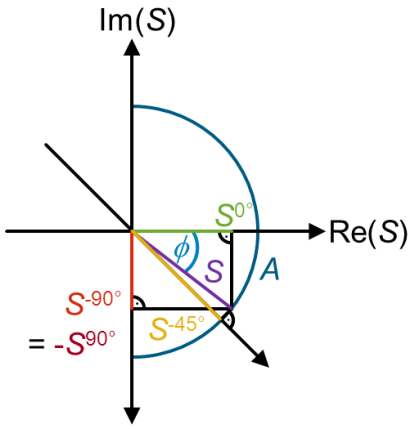

Figure 3.3: Lock-in signal S in the complex plane. The lock-in signal S with the amplitude A and phase ϕ can be described in the complex plane by two components called the "in-phase" real signal $S^{0°}$ and the "quadrature" imaginary signal $S^{90°}$ with $S = S^{0°} + iS^{90°}$. In lock-in thermography, usually phase shifts by time delays occur that have negative angles. Therefore, instead of the $S^{90°}$ signal, the $S^{-90°} = -S^{90°}$ signal is used. The components can be calculated by $S^{0°} = A\cos\phi$ and $S^{-90°} = A\sin\phi$. The signal $S^{-45°}$ is often used in lock- in evaluations and can be calculated by $S^{-45°} = (S^{0°} + S^{-90°})/\sqrt{2}$.

The correlation functions become correlation vectors $K = [K_1, K_2, \dots, K_m, \dots, K_n]$ calculated by

$$K_m^{0°} = 2\sin\left(2\pi\frac{(m-1)}{n}\right) \tag{3.26}$$

and

$$K_m^{-90°} = -2\cos\left(2\pi\frac{(m-1)}{n}\right). \tag{3.27}$$

As a consequence of the discretization, there is a time interval t_s between two measurement points. The reciprocal of t_s is the sampling rate $f_s = 1/t_s$. It determines the most important parameter of lock-in measurements, the measurement frequency $f_{\text{lock-in}}$, by

$$f_{\text{lock-in}} = \frac{f_s}{n}. \tag{3.28}$$

To obtain $S^{0°}$ and $S^{-90°}$ signals that ensure a unique interpretation, n has to be set to $n = 4$ at least, according to the sampling theorem [68, 69]. Therefore, the achievable lock-in frequencies are

$$f_{\text{lock-in}} \leq \frac{f_s}{4} \tag{3.29}$$

with the maximum $f_{\text{lock-in}}^{\max} = f_s/4$. Note that in a measurement system, the sampling rate f_s is usually constant and only n can be varied. Thus, n determines $f_{\text{lock-in}}$, permitting only discrete frequencies. This discretization can induce errors in the lock-in process that are discussed in detail in the following chapter.

3.3 Error sources in the lock-in process

The lock-in signal generation process inherits several obstacles for the correct quantitative analysis owed to the fact that the signal detection has to be discretized. The main influences on the process are the choice of the number of frames per period n and the choice of suitable correlation functions (or vectors, respectively). A low n leads to an insufficient reproduction of $K^{0°}$ and $K^{-90°}$. Thus, the lock-in signal can inherit quantification errors. A simple error estimation for $n = 4$ and $n = 8$ can be found in [6, p. 37]. I carried out a detailed investigation on the choice of n based on simple simulations of the algorithm that are presented in chapter 3.3.3. I find that the correlation vectors have to be matched in their height, which is the correlation coefficient c, and have to be distributed evenly over a period. There are three reasonable distributions conceivable that I discuss in chapter 3.3.2, following the evaluation of the correct choice of c in the next subchapter 3.3.1.

3.3.1 Matching of correlation coefficient

The correlation coefficient c matches the integrals of the response function F with the integrals of the correlation vectors K_i. The derivation of the lock-in signal in chapter 3.2 used a harmonic signal, the sine function, as response. This is not possible in many measurement setups, e.g. electronic devices. These devices inherit electronic parts with strongly non-linear behavior that cannot be operated successfully with a harmonic stimulation. Therefore, LIT uses a step function, namely

$$F = \begin{cases} A, & 0 \leq t < T_{\text{per}}/2 \\ 0, & T_{\text{per}}/2 \leq t < T_{\text{per}} \end{cases} \tag{3.30}$$

with the amplitude A and the period T_{per}. The harmonic correlation function

$$K^{0^\circ} = c\sin(2\pi f t) \tag{3.31}$$

is used, with $f = 1/T_{\mathrm{per}}$, and c being the correlation coefficient. These assumptions inserted in equation (3.11) yield

$$\begin{aligned} S^{0^\circ} &= \frac{1}{T_{\mathrm{per}}}\int_0^{T_{\mathrm{per}}} F \cdot K^{0^\circ}\, dt \\ &= \frac{1}{T_{\mathrm{per}}}\left(\int_0^{T_{\mathrm{per}}/2} Ac\sin(2\pi f t)\mathrm{dt} \;+\; \int_{T_{\mathrm{per}}/2}^{T_{\mathrm{per}}} 0 \cdot c\sin(2\pi f t)\,\mathrm{dt}\right) \\ &= \frac{1}{T_{\mathrm{per}}}\left(Ac\left[-\frac{1}{2\pi f}\cos(2\pi f t)\right]_0^{T_{\mathrm{per}}/2}\right) \\ &= \frac{Ac}{T_{\mathrm{per}}\cdot 2\pi f}\left(1-\cos\left(2\pi f\frac{T_{\mathrm{per}}}{2}\right)\right), \end{aligned}$$

and with $f = 1/T_{\mathrm{per}}$,

$$S^{0^\circ} = \frac{Ac}{2\pi}(1-\cos\pi) = \frac{Ac}{\pi}. \tag{3.32}$$

Equation (3.32) shows that the correlation coefficient has to be $\underline{c = \pi}$ to find the correct signal amplitude. Breitenstein does not specify the correlation coefficient c for the step function F and uses $c = 2$ for the modulation with a harmonic signal [6, p. 18]. Isenberg and Warta reported the coefficient to be $c = \pi/2$ [70, 71, 72, p. 61] for LIT. The same research group had previously used $c = \pi/2$ for carrier density imaging (CDI) measurements, but including a "correction factor" $\xi = 2$, so that $\pi/2 \times \xi = \pi$ [73]. In the presentation of CDI in the book of Breitenstein [6, p. 97], the correlation coefficient is given as $c = 2$ and the correction factor as $\xi = \pi/2$. I hope this confusion will vanish if in future the LIT correlation vectors for the sine/-cosine correlation

$$K_m^{0^\circ} = \pi\sin\left(2\pi\frac{(m-1)}{n}\right) \tag{3.33}$$

and

$$K_m^{-90°} = -\pi \cos\left(2\pi \frac{(m-1)}{n}\right) \tag{3.34}$$

with m being the aggregate index are used to reconstruct the correct signal value of A.

3.3.2 Distribution of correlation bases

There are three reasonable distributions conceivable how correlation bases can be distributed in one lock-in period. Figure 3.4 shows the distributions on the example of $n = 4$. Additionally, it shows the integration time t_{int} that a measurement system needs to measure the signal F at this point of time. Usually, t_{int} is very small compared to the period T_{per}. At high frequencies, t_{int} should possibly be lowered, so that no errors are induced. For the evaluation a simple signal was chosen, which is the step function $F = \begin{cases} 1, & 0° \le \phi < 180° \\ 0, & 180° \le \phi < 360° \end{cases}$.

The three reasonable distributions of the correlation bases for $n = 4$ are:

a) The periodic time T_{per} is divided by the number of frames or correlation bases per period n to yield the time t between the bases. The first base is set to $t_1 = 0$, the others at $t_2 = T_{per}/n$, $t_3 = 2\,T_{per}/n$, $t_4 = 3\,T_{per}/n$, etc. up to $t_n = T_{per}(n-1)/n$. Generally expressed, $t_i = T_{per}(i-1)/n$. For $n = 4$, $K_i^{0°} = \pi \sin(2\pi\,(i-1)/4)$ and $K_i^{-90°} = -\pi \cos(2\pi\,(i-1)/4)$ (see equations (3.33) and (3.34)), e.g., the correlation vectors would be $K^{0°} = [0, \pi, 0, -\pi]$ and $K^{-90°} = [-\pi, 0, \pi, 0]$ at the phase positions $\phi = [0°, 90°, 180°, 270°]$ (blue colored bases in Figure 3.4).

b) The first base is set to $t_1 = 0$ and the last one to $t_n = T_{per}$. In between, they are distributed evenly so that $t_i = T_{per}(i-1)/(n-1)$. For the example of $n = 4$, this leads to $K^{0°} = \left[0, \pi\sqrt{3}/2\,, -\pi\sqrt{3}/2\,, 0\right]$, $K^{-90°} = [-\pi, \pi/2\,, \pi/2\,, -\pi]$ and $\phi = [0°, 120°, 240°, 360°]$ (purple colored bases in Figure 3.4).

c) All correlation bases are distributed equidistantly and centered over the period so that $t_i = T_{per}(2i-1)/2n$. In case of the example $n = 4$, this leads to $K^{0°} = \left[\pi\sqrt{2}/2\,, \pi\sqrt{2}/2\,, -\pi\sqrt{2}/2\,, -\pi\sqrt{2}/2\right]$, $K^{-90°} = \left[-\pi\sqrt{2}/2\,, \pi\sqrt{2}/2\,, \pi\sqrt{2}/2\,, -\pi\sqrt{2}/2\right]$, and $\phi = [45°, 135°, 225°, 315°]$ (yellow colored bases in Figure 3.4).

Figure 3.5 shows the simulation results for these different correlation bases for the sine/cosine-correlation (a-c) as well as for the equidistantly distributed and centered bases for the rectangle correlation (d). The rectangle correlation uses the correlation

functions $K^{0°} = \begin{cases} 2, & 0° \le \phi < 180° \\ -2, & 180° \le \phi < 360° \end{cases}$ and

$K^{-90°} = \begin{cases} -2, & 0° \le \phi < 90° \text{ and } 270° \le \phi < 360° \\ 2, & 90° \le \phi < 270° \end{cases}$.

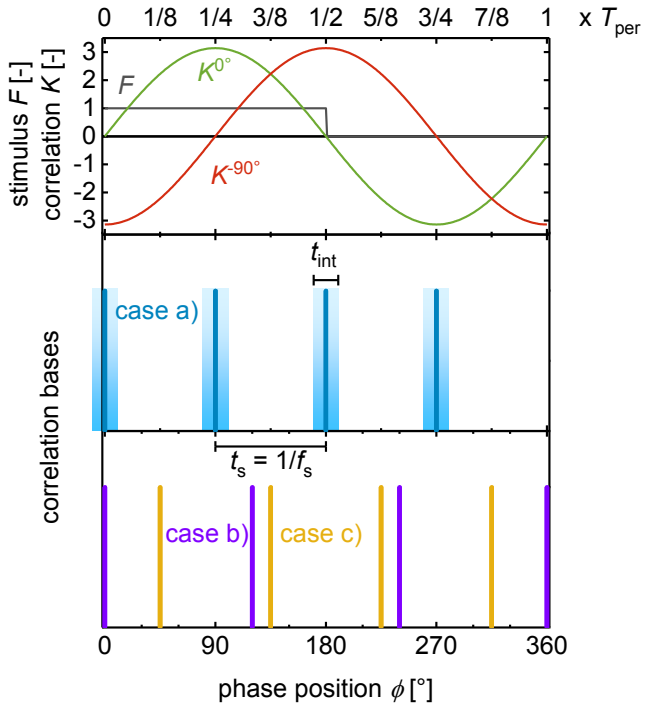

Figure 3.4: Possible distributions of correlation bases within a lock-in period. The example shows a response signal F measured with the lock-in process over one period T_{per}. *In theory, it is multiplied with the correlation functions* $K^{0°}$ *and* $K^{-90°}$, *which are the sine and –cosine functions. In practice, the functions have to be discretized so that a system can measure at a certain amount of time points n with its integration time* t_{int}. *To evenly distribute the discretized correlation bases at time points* t_i *in a lock-in period, three possibilities are illustrated: case (a) with* $t_i = T_{per}(i-1)/n$, *case (b) with* $t_i = T_{per}(i-1)/(n-1)$ *and case (c) with* $t_i = T_{per}(2i-1)/(2n)$.

All distributions tend to the saturation value $A_{sat} = 1$ if n is sufficiently high, i.e. $n \ge 100$, and thus are capable of reproducing the signal height correctly. At low values for n, the reconstruction fails for uneven n in all distributions. For $n \le 100$, the rectangular correlation in d) produces errors for even n also. Therefore, the rectangle correlation is not very reliable. In the same low range for n, the distributions a) and b) create a phase shift to negative values. Nevertheless, the amplitude signal A does not differ too much from the signal value $F = 1$. The reproduction worked well if A and $S^{0°}$ are congruent, as $S^{0°}$

is the carrier of the information if F does not contain a phase shift. The distribution c) delivers the most relying reproduction of the signal height if uneven n are avoided.

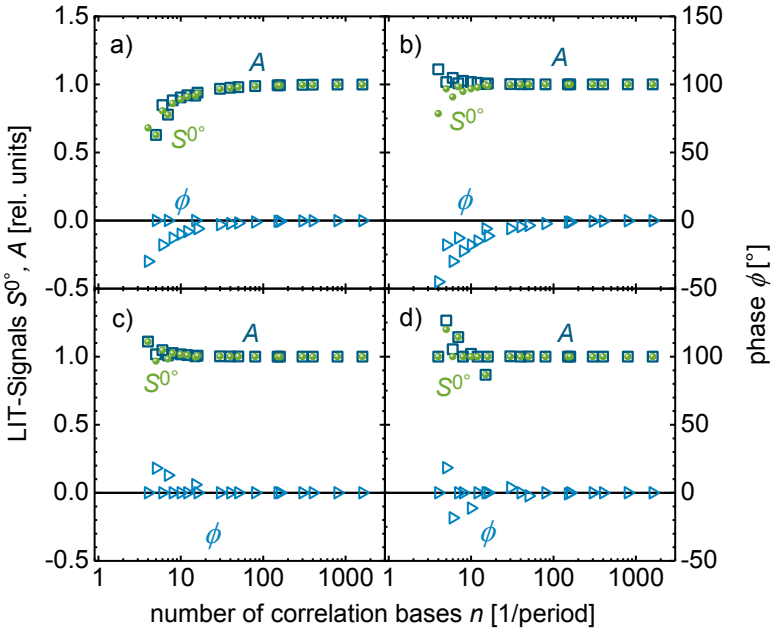

Figure 3.5: Lock-in signals $S^{0°}$, A and ϕ over the number of correlation bases n for different correlations. The distribution of correlation bases in cases (a), (b), and (c) is according to Figure 3.4. In (d), a rectangular correlation function is used with the same distribution of correlation bases as (c). For a sufficient number of correlation bases n in a period, all correlations reconstruct the initial amplitude of $A = 1$ and phase $\phi = 0$. The reconstruction fails in every case for uneven numbers and at a low number n. The distribution shown in (c) delivers the most reliable detection of F; the deviations in the amplitude can be calculated and corrected in a lock-in implementation.

The errors of the reproduction for $n \leq 40$ can be calculated and corrected. For the above example of $n = 4$, which is also known as the 4-bucket method [74], we know the correlation vectors to be $K^{0°} = [\pi\sqrt{2}/2, \pi\sqrt{2}/2, -\pi\sqrt{2}/2, -\pi\sqrt{2}/2]$ and $K^{-90°} = [-\pi\sqrt{2}/2, \pi\sqrt{2}/2, \pi\sqrt{2}/2, -\pi\sqrt{2}/2]$. With $F = [1, 1, 0, 0]$, the carrier signal is according to (3.25) $S^{0°}_{n=4} = 1/4\,(1 \times \pi\sqrt{2}/2 + 1 \times \pi\sqrt{2}/2 - 0 \times \pi\sqrt{2}/2 - 0 \times \pi\sqrt{2}/2) = \pi\sqrt{2}/4 \approx 1.11 = A^{n=4}$. That means, the amplitude result $A^{n=4}$ needs to be multiplied with the correction factor $k^{n=4}_{\mathrm{corr}} = 2\sqrt{2}/\pi \approx 0.90$ to yield the correct amplitude $A = k^{n=4}_{\mathrm{corr}}\, A^{n=4} = 1$. With the implementation of such a correction for each measurements with a low n, a reliable lock-in process can be programmed for all even n.

3.3.3 Reliable detection of amplitude and phase

In the chapters above, I only considered a signal F without a signal phase shift ϕ between excitation and response. Therefore, the $S^{0°}$ signal reproduced the signal height and had the same value as A in most cases. A signal shift ϕ can be introduced over a certain dead (or delay) time t_{dead}. Please note that the mathematical convention defines *a delay in time as a phase shift towards negative angles*. Figure 3.6 shows the resulting signals $S^{0°}$, $S^{-45°}$, $S^{-90°}$, A and ϕ of the lock-in process over the number of correlation bases n for the same signal F as above, but shifted by ϕ_a = -45° (a) and ϕ_b = -90° (b), respectively. Here, the equidistant distributed and centered correlation bases – case (c) in chapter 3.3.2 – are used.

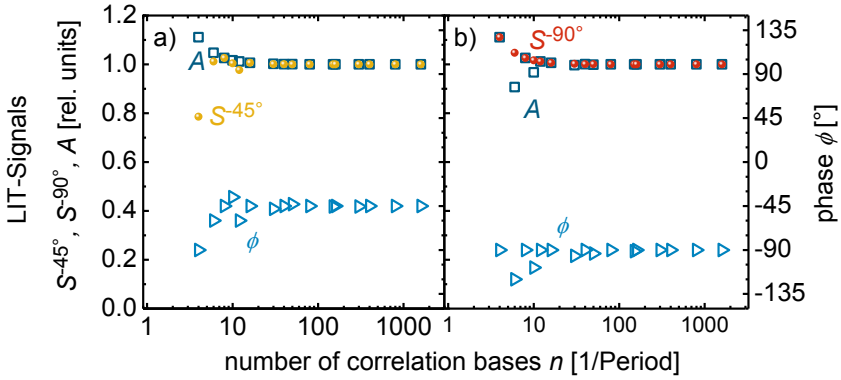

Figure 3.6: Response signals with time delays detected by the lock-in process. For this simulation of the lock-in process, time delays with a dead time t_{dead}, corresponding to signal phase shifts ϕ, were introduced. Case (a) shows a phase shift of -45°*, (b) of* -90°*. The original signal can reliably be detected with the lock-in process if a sufficient amount n of correlation bases is chosen. If n is chosen to an uneven number or too low, deviations in the detection of both amplitude and phase occur.*

For $n \leq 40$, the lock-in process works reliably and detects the phase shift ϕ well. Additionally, it shows that the $S^{-45°}$ (a) and $S^{-90°}$ (b), respectively, reproduce the signal height of F, i.e. their values are equal to A.

Another way how a phase shift ϕ between excitation and response signal becomes detectable is a distortion of the response signal shape. Thermal behavior, e.g., does not respond with a dead time t_{dead}, but with a capacitive distortion of the rectangular stimulation. Then the answer turns out to be a limited growth for the first half period (if no phase shift over a dead time is present) and an exponential decay for the second half period. The shape distortion of F usually strengthens with increasing stimulation frequency. This behavior of an increasing phase shift due to a response signal distortion

is modeled and displayed in Figure 3.7. For the limited growth in the form of $1 - e^{-t/\tau}$ and the exponential decay in the form of $e^{-t/\tau}$, I use the same time constant τ, which depends on *n* over a linear proportionality.

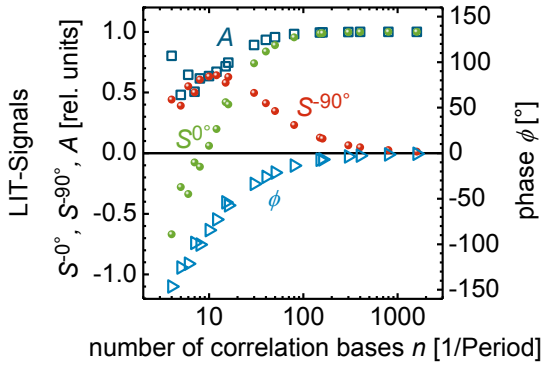

Figure 3.7: Capacitive response signals with phase shifts detected by the lock-in process. Capacitive response signals are distorted step functions with a limited growth in the first half period and an exponential decay in the second. In this simulation, the time constant of growth and decay was the same and was linearly connected with the number of correlation bases n. The expected phase shift to higher negative angles with decreasing n can principally be detected by the lock-in process.

For decreasing *n*, meaning a higher signal shape distortion, the amplitude *A* decreases (except for two outliers at low *n*). $S^{0°}$ decreases for lower *n*, even to negative values. At high *n*, $S^{0°}$ is the carrier of the information and congruent with *A*, as expected. The behavior of $S^{-90°}$ shows an increase for lower *n* up to a maximum at $n = 12$ and then a decrease. The phase ϕ decreases with decreasing *n,* illustrating that a phase shift due to a response signal distortion can principally be measured with the lock-in process.

For high frequencies, the originally rectangular signal can be deformed to a triangular shape. The lock-in result of a triangular signal with $F = 0$ at $t = 0$ and $F = 1$ at $t = T_{per}$, and linear increase in between, is shown in Figure 3.8.
The detected signal phase ϕ is -90° for high *n*; at low *n,* ϕ lies at almost -120°. Thus, a triangular response signal implies a phase of -90° (as the lock-in process is reliable for high *n*). Therefore Figure 3.8 shows that a reliable detection of a triangular signal with the lock-in process only works out for $n \geq 100$. This leads to the conclusion that at high measurement frequencies – which come along with a low sampling rate, i.e. with low *n* – the signal detection is not reliable.

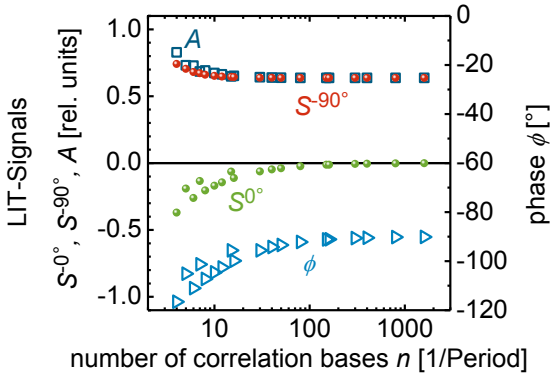

Figure 3.8: Triangular signal detected by the lock-in process. A triangular signal is the maximal response signal distortion for a capacitive phase shift. The simulation of the lock-in process for such a response signal shows that it is only reconstructed reliably with a high number of correlation bases $n \geq 100$*, showing a phase of* -90°*. A number of* $100 \leq n \leq 20$ *still delivers satisfying results. With less n, a not existent further phase shift up to almost* -120° *is detected and the amplitude A is overestimated.*

Summarizing, it can be stated that the lock-in process is a reliable tool for the detection of harmonic and rectangular signals with any phase shift over a dead time delay t_{dead}, if following implementation issues are considered:

- The correlation coefficient c should me matched to the shape of the response signal, i.e. $c = 2$ for a harmonic stimulation and $c = \pi$ for a rectangular stimulation.
- The number of correlation bases n shall only be chosen as an even number. Furthermore, low n (≤ 30) should be avoided if possible. For some values of n, c can be adapted to correct the correlation and to allow low n.
- The correlation bases should be distributed over a lock-in period in such a way that they have the equal distance $t_s = T_{per}/n$ to their neighboring base. Additionally, they have to be centered over the whole period (shifted by $t_{shift} = T_{per}/(2n)$).

Signals with capacitive responses can principally be detected also. However, using $n \leq 100$, deviations occur that are difficult to describe in general. Therefore, the use of $n \geq 100$ is recommended.

3.4 Setup and methods

3.4.1 LIT setup

A typical LIT setup consists of several devices interacting with each other. The most important device of an LIT setup is the thermographic camera (or infrared camera, IR camera) that detects infrared radiation. For the spectral ranges SWIR, MWIR and LWIR, several detectors of different materials are available; some detectors are sensitive in more than one spectral range. At IEK-5, we use a thermographic camera with a mercury cadmium telluride (MCT) detector for SWIR and MWIR with an image resolution of 640 × 512 pixels and endued with several spectral filters.

As discussed in chapter 3.1, the measured irradiance always contains the information on the sample's emissivity times its temperature to the power of 4 (equation (3.10)). That means a homogenous emissivity has to be ensured. At IEK-5, we apply a black spray paint on the back of the measured solar modules to reach a more homogeneous emissivity. Details on the emission of the solar cells are given in chapter 4.7.

The camera needs to be calibrated, if temperatures are to be measured directly. In this thesis, samples were measured in the temperature range 20 °C to approximately 70 °C. Figure 3.9 depicts the irradiance E^{meas} after equation (3.10) with an assumed emissivity of ε = 1. The irradiance increases with a slight slope only in that temperature range. This is important for the calibration, as usually only a linear approximation of the values between two calibration temperatures is supported by the manufacturers.

I used the calibration temperatures 20 °C and 40 °C; between these temperatures the linear approximation deviates maximally 1 % at $T = 30$ °C. At 50 °C, the highest integral value for the sample temperature in the measurements shown in this thesis, the deviation is 1.4 %. At 80 °C, the highest measured temperature of a small hot spot, the underestimation is 9.6 %. Overall, these deviations due to the calibration are well acceptable assuming the high temperatures in small hot spots are not quantitatively evaluated. If so, a correction deduced from both curves in Figure 3.9 has to be used; or a calibration device that reaches such high temperatures.

The velocity of the detector readout in a thermographic camera determines its maximal possible lock-in frequency $f_{\text{lock-in}}$ (see chapter 3.2). Its sampling rate f_s is usually called frame rate f_r, as it illustrates the number of frames (or images) per second that are read out. The frame rate depends of the pixel resolution of the recorded images and can be enhanced using smaller resolutions. For example, the LIT system of IEK-5 has a maximum f_r of 170 Hz for a full frame (640 × 512 pixel) image. It can be increased up to 400 Hz at a frame size of 256 × 256 pixels. According to equation (3.29), f_r limits $f_{\text{lock-in}}$, so that the maximal measureable frequencies at IEK-5 are $f_{\mathrm{lock-in}}^{\max} = 42$ Hz at full resolution and $f_{\mathrm{lock-in}}^{\max} = 100$ Hz at reduced resolution.

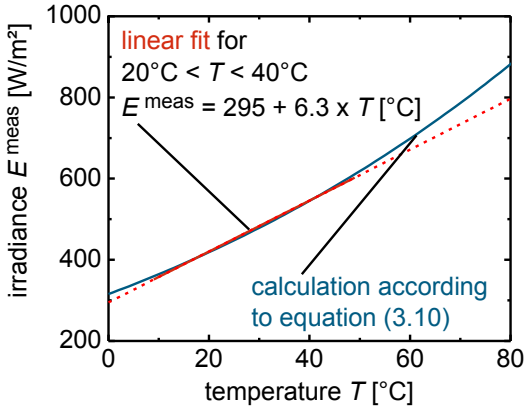

Figure 3.9: Linear fit to the irradiance between 20 °C *and* 40 °C. *This linearization of the irradiance* E^{meas} *is used for the temperature calibration of the thermographic camera at IEK-5. The deviations between fit and actual irradiance are smaller than* 1.4 % *in the temperature range between* 20 °C *and* 50 °C. *If small hot spots with a temperature of about* 80 °C *have to be measured directly, the temperatures are underestimated by* 10 %.

Figure 3.10 shows a scheme of a complete LIT setup with a thin film solar cell sample. The measurement control and configuration is carried out from a personal computer with control software. It provides a periodically pulsed signal with a frequency $f_{\text{lock-in}}$ and reads out and processes the camera raw data.

The signal is either passed on to a power supply, which applies an electrical modulation of the sample, or to a light source for the modulation through illumination. Depending on the chosen stimulus source, LIT measurements are called DLIT (dark lock-in thermography) in case of electrical stimulation (since no light is used) or ILIT (illuminated lock-in thermography) in case of applied illumination. Some ILIT measurement methods combine a constant illumination with an electrical modulation. For ILIT experiments it is advisable to use a power supply that can act as an electrical load in order to absorb the power generated by the solar cell / module. An overview of state-of-the-art DLIT and ILIT methods is given in the following subchapter 3.4.2.

Two different types of illumination sources are used for ILIT measurements: a panel with light emitting diodes (LED) or a laser source. The requirement is the homogeneous illumination of a sample with a very high irradiance of $E = 1000$ W/m². This high intensity is needed to reach the short circuit current density J_{sc} of the sample and to perform measurements under comparable and realistic conditions. The high irradiance puts high demands on the power electronics of the illumination source, as it has to provide the high power needed and must be able to switch it on and off with lock-in frequencies up to several ten Hertz. The LED panel of IEK-5 has LEDs of two light wave-

lengths; blue (450 nm) and infrared (850 nm). With each light color, an irradiance of E = 1000 W/m² can be achieved on an area of 10 × 10 cm². The homogeneity H reached on the same area is about 38 %. It improves strongly (H < 10 %) when applied to a smaller area or at a larger distance of sample and light source. In the latter case, a strong reduction of the irradiance E has to be accepted.

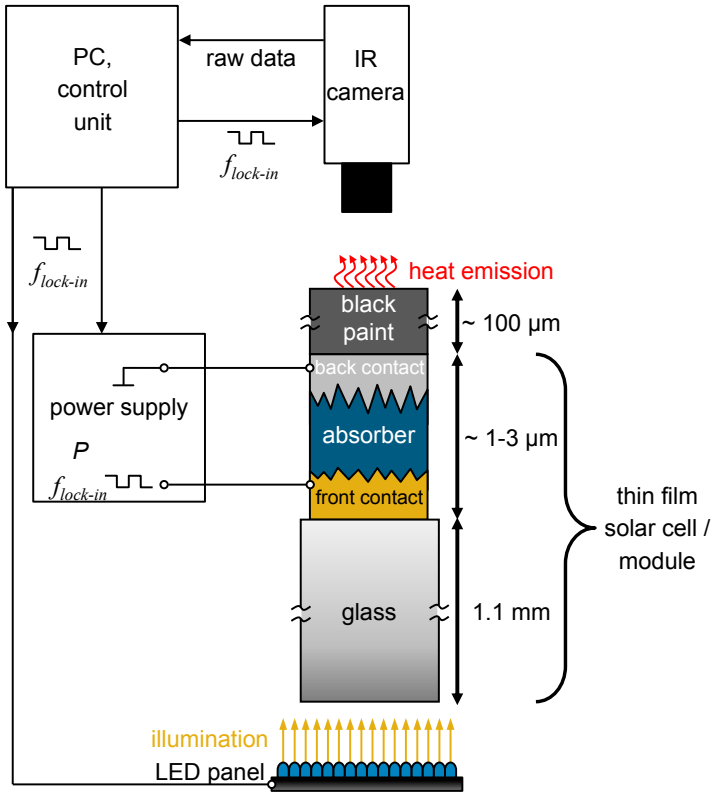

Figure 3.10: LIT measurement setup. The thermographic camera captures the radiated heat. The lock-in process is driven by a personal computer, which sends the stimulation with $f_{lock\text{-}in}$ to the camera and the excitation sources. The sources can be an electrical power supply applying a bias voltage, or a light source. For thin-film silicon solar cells and modules, it is advantageous to illuminate from the front side and to capture the emitted heat from the back, where a black paint enhances and homogenizes the emissivity.

The sample sketched in Figure 3.10 is a thin film solar cell or module as described in chapter 2.1. For a better signal-to-noise ratio (*SNR*), the camera faces the sample from that side of the solar cell that has a black paint coating meant to enhance and to homogenize the infrared emissivity of the back metal (see chapter 4.7). In ILIT

measurements, the illumination impinges through the glass superstrate and reaches the absorber layer via the transparent front contact (superstrate setup configuration). For other configurations of solar cells and modules, e.g. crystalline silicon or CIGS, the illumination source is installed at the same side on the cell/module as the camera (substrate setup configuration).

3.4.2 State-of-the-art LIT methods

The previous chapters showed that all lock-in thermography methods use a periodic excitation that can be either an applied voltage or illumination. Before the development of illuminated LIT in 2004 by Isenberg et. al. [70] and Kaes et. al. [75], all LIT measurements were carried out in the dark (DLIT) with a periodically pulsed bias voltage. The first applications were the qualitative evaluation of shunt and series resistances. By applying low positive or negative voltages, shunts in crystalline silicon solar cells were categorized [51]. A comparison of two LIT images at different voltages showed series resistances [52]. The method of local *I/V* characteristics measured thermally (LIVT) enabled the estimation of shunt *P/V* and *I/V* characteristics [76]. A mapping of the local dark saturation current J_0 and the ideality factor n became possible by approximating the *I/V* characteristic of a solar cell with an exponential curve using two LIT images at different voltages [6, p. 193]. Applying negative voltages, breakdown sites were investigated. The comparison of LIT results at different temperatures led to conclusions on the local temperature coefficient, the slope of breakdown currents, and the multiplication factor of breakdown sites [45]. Despite all the achievements of DLIT, these methods do not allow a realistic evaluation of the physical behavior of solar cells / modules under operation conditions, i.e. under illumination.

Several ILIT methods have been developed by now, which were all established on crystalline silicon solar cells. Basic methods (V_{oc}-, J_{sc}-, MPP-ILIT) modulate the illumination and differ from each other in the applied voltage. Advanced methods use a combination of several ILIT-images (R_s-ILIT) or calculate the efficiency (η-ILIT) [77].

According to Breitenstein [6, p. 203], the "simplest and most popular" ILIT method is V_{oc}-ILIT since no contacting is needed. Therefore, it can be carried out in an early stage of solar cell processing. To acquire images with J_{sc}-ILIT [78], the solar cell or module has to be contacted and short-circuited. The short-circuiting forces the photo current J_{ph} to flow through the solar cell or module. MPP-ILIT can be carried out in two ways: either a resistor is connected to the contact that operates the solar cell / module at its MPP, or an electrical load applies the MPP voltage V_{MPP} and absorbs the extracted power P_{ext}. In the latter case, the voltage has to be modulated simultaneously with the irradiance. Otherwise, the measurement may inherit errors. By modulating the light only, V_{MPP} would be applied also when the light is off. Then a small dark current J_{dark}

would flow, changing the modulated power compared to the case of a connected resistor.

R_s-ILIT can be carried out in two ways also: Either by applying a constant illumination and modulating the voltage between $V = 0$ and $V = V_{MPP}$, or by subtracting an MPP-ILIT image by a J_{sc}-ILIT image. Both ways deliver the same result as will be shown in detail in chapter 7.2.

A principal overview on the state-of-the-art LIT methods used in this thesis is given in Table 3.1, listing the measurement parameters modulation and bias, and the derived results. Furthermore, an alternative terminology is introduced in Table 3.1. The existing terminology of LIT methods may cause confusion, since it does not contain the modulated quantity (light or voltage). It divides the LIT methods depending on the application of light, regardless whether the illumination or the voltage is modulated. To distinguish the respective methods, I follow the terminology introduced by Kaes et. al. [75], naming each method after the respective modulation. Methods using a voltage modulation are named Vomo-LIT, standing for voltage-modulated LIT. Methods using voltage modulation and additionally a constant bias illumination are referred to as Vomo-ILIT. Methods using light modulation are named Limo-LIT, standing for light modulated LIT. The applied bias is then attached at the end, e.g. Limo-LIT@V_{oc}.

3.5 LIT signals of thin film solar cells

Since the LIT signal S is a complex signal (see equation (3.16)), different real signals can be used for the evaluation of thin film silicon solar modules. These are the phase dependent signals $S^{0°}$, $S^{-90°}$, $S^{90°}$, $S^{-45°}$ as well as the absolute (amplitude) value $A = |S|$ and the phase ϕ. Figure 3.11 shows Vomo-LIT images of a typical µc-Si solar module acquired at $f_{lock\text{-}in} = 3$ Hz and an applied bias of $V = 8.6$ V, which caused a current density of $J = 34$ mA/cm² ≈ 0.8 × J_{sc}: a) $S^{0°}$, b) $S^{-90°}$, c) $S^{90°}$, d) $S^{-45°}$, e) A, and f) ϕ. The signals in (a), (b), (d), and (e) are scaled to the same values. For an easier comparison, Figure 3.12 displays the mean value (in y direction) linescans of the images from Figure 3.11 in x direction.

The $S^{0°}$ image has the highest sharpness and is therefore helpful for the detection of small features, e.g. shunts. In chapter 6 it is shown how the dimensions of small heat sources like shunts can be reconstructed.

Compared to the $S^{0°}$ image, the $S^{-90°}$ image looks blurry and has a lower contrast. The $S^{90°}$ signal – the imaginary part of S – is the negative inverse of $S^{-90°}$, i.e. $S^{90°} = -S^{-90°}$.

Table 3.1: State-of-the-art LIT methods, parameters used and results gained. An alternative terminology for the methods used in this thesis includes the modulation source (voltage or light) in the method name. All influencing parameters and the result of the methods are listed together with references of publications of the methods.

existing name	DLIT	LIVT	V_{oc}-ILIT	J_{sc}-ILIT	MPP-ILIT	R_s-ILIT
name used in this thesis	Vomo-LIT	LIVT	Limo-LIT@V_{oc}	Limo-LIT@J_{sc}	Limo-LIT@ MPP	Vomo-ILIT from $V = 0$ to $V = V_{MPP}$
modulation	voltage V	V	irradiance E	E	E and V	$V = 0$ to $V = V_{MPP}$
bias	-	-	$V = V_{oc}$	$V = 0$	$V = V_{MPP}$	$E = E_{STC}$
result	qualitative shunt-, R_s- imaging	thermal P/V and I/V characteristics	qualitative shunt-imaging	qualitative R_s- imaging	image at real operation conditions	extracted power density
reference	[51, 79]	[76]	[71, 6, p. 203]	[71, 78, 6, p. 205]	[71, 6, p. 208]	[80, 6, p. 207]

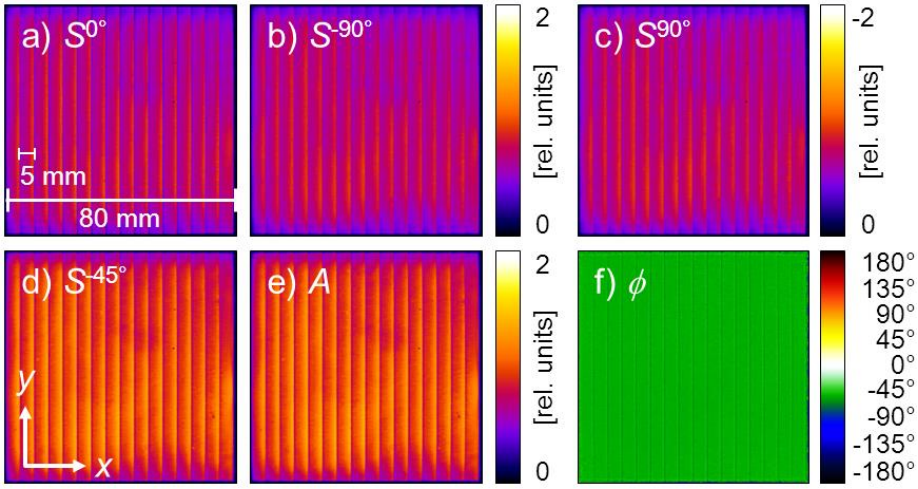

Figure 3.11: Vomo-LIT images of a µc-Si thin film solar module. The measurement was derived using a lock-in frequency of $f_{lock\text{-}in}$ = 3 Hz and an applied voltage of V = 8.6 V, leading to a current density of J = 34 mA/cm². The complex Vomo-LIT signal S can be described by its absolute value A (e), phase ϕ (f), real part $S^{0°}$ (a) and imaginary part $S^{90°}$ (c). Instead of $S^{90°}$, usually the positive signal $S^{-90°} = -S^{90°}$ (b) is used. In the case of thin film solar modules on glass, the phase shift is -45°. This makes the $S^{-45°}$ signal (d) the main carrier of the information.

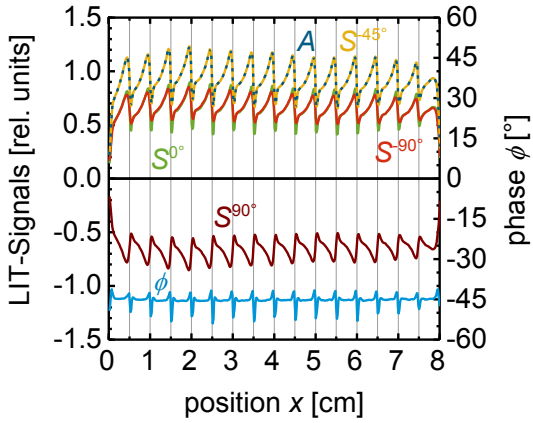

Figure 3.12: Mean value linescans of Vomo-LIT images of a µc-Si thin film solar module. The linescans are calculated for the images shown in Figure 3.11 by averaging in y direction. The $S^{-45°}$ signal is the information carrying signal and thus congruent to A as long as it does not contain negative values. $S^{0°}$ and $S^{-90°}$ have the same value of $A/\sqrt{2}$.

The $S^{-45°}$ image is the highest signal overall; the phase image lies at -45° for the largest parts (see chapter 5). That means the signal of thin film solar cells on glass substrates is shifted by -45° compared to the stimulation. Therefore, the $S^{-45°}$ signal is the correct signal for the quantification of LIT images of thin film solar cells and modules. One more detail proves this fact: The amplitude A is congruent to the $S^{-45°}$ signal as long as it is positive, which is true for this example (see Figure 3.12). As A cannot be negative by its definition in equation (3.23), errors are induced when A is used for quantification. This means, A cannot describe thermal cooling processes. However, it is the most commonly displayed signal (especially for crystalline silicon solar cells), as it combines the information of the $S^{0°}$ (small heat sources) and $S^{-90°}$ (extended heat sources) signals.

The phase image ϕ is seldom used in publications, even though it contains valuable information. The phase image does not contain any emissivity contrast [6, p. 139] and resolves small heat sources even better than the $S^{0°}$ image. As shown, the phase image provides the information, at which phase value the highest signal is found, i.e. what signal to use for quantification. At which phase a signal lies, depends on the sample's geometry and material; for crystalline silicon solar cells it is -90°, for thin film solar cells on glass substrates, it is -45° [6, p. 134]. A detailed discussion of the origin of the phase signal is given in chapter 5. The drawbacks of the phase description are the high amount of noise in regions, where $S^{0°}$ and $S^{-90°}$ are of small signal strength, and

the non-proportionality to the dissipated heat. The latter point is the reason for the constant phase signal over a cell.

All signals except ϕ show a power drop over a cell width in x direction. This power drop can be explained as follows: The current I flows in the front TCO layer mainly in x (Limo-LIT) or $-x$ (Vomo-LIT) direction as shown in Figure 2.7, where it encounters the sheet series resistance R_{sheet}. The sheet resistance hampers the current density $J(x)$ to evenly distribute over the cell width w, resulting in a higher current density at the side of the current injection and a lower current density at the opposite site. Additionally, a voltage drop over the cell width w due to R_{sheet} occurs. Both effects lead to a power distribution over the cell width as can be seen in all Vomo-LIT images of thin film solar modules with a certainly high injection current (compare Figure 3.11 and Figure 4.1). At lower injection currents, the effect diminishes as visible in Figure 4.1.

4 Defect analysis of thin film solar modules with basic LIT methods

The topic of this chapter is the information about thin film solar modules gained by basic LIT methods. The chapter begins with an introduction of LIT measurement regimes and explains which parameters have to be used to visualize certain information. Following, investigations on resistance related defects such as shunts and sheet resistances are presented. Basic voltage- and light-modulated LIT methods are compared, showing their abilities and limits. The last sub-chapter deals with the measurement of capsuled modules and shows to which extent the capsulation hampers LIT evaluations.

4.1 Basic measurement strategies

The basic Vomo-LIT setup allows varying two main parameters:

- the measurement frequency $f_{\text{lock-in}}$, which is set indirectly over the frame rate f_r and the number of frames per period n as shown by equation (3.28);
- the applied bias voltage V, leading to a power dissipation in the measured device of $P_d = V \times I_{dark}$ (equation (2.22)).

With these two parameters, a matrix can be generated that shows the properties of LIT images of thin film solar modules in dependency of $f_{\text{lock-in}}$ and V. This matrix is depicted in Table 4.1 and gives information about the visibility of resistance related defects (a), the spatial resolution (b), the signal-to-noise ratio *SNR* (c), the needed measurement time (d), and possible unwanted by-effects like slow overlapping temperature transients (e), problems with the evaluation due to the lock-in process (f) (see chapter 3.3.3) or possible damaging of the solar module (g).

In principle, three bias regimes and three frequency regimes can be distinguished. Each regime accentuates different features in the LIT images of thin film solar modules. For an overview, I start with the bias regimes. As explained in chapter 2.2, a solar module has a current-voltage characteristic of several diodes in series connection. Therefore, the electrical behavior is different depending on the applied voltage and with that, the injected current. Here, I separate three bias regimes: reverse bias injection (applied voltage is negative), low injection currents of about 1/10 of J_{sc} (applied voltage is about V_{oc}) and high injection currents of about J_{sc} or higher (applied voltage is higher than V_{oc}). The chosen lock-in frequency has a high influence on the spatial resolution and the *SNR* of the resulting LIT images, and therefore, on the measurement time. Additionally, measurements at low frequencies may overlap with slow temperature transients, which can influence the result. As shown in chapter 3.3.3, high frequencies due to

a low number of frames per period n induce errors, too. Thus, I divide the possible LIT frequencies in three ranges as Table 4.1 shows. To illustrate the regimes and the differing information gained due to them, Figure 4.1 displays LIT measurements of a tandem module at the regimes 1 to 9 defined in Table 4.1. The measurement parameters for the regimes were:

1) $f_{\text{lock-in}} = 0.5$ Hz ($f_r = 160$ Hz, $n = 320$), $V = -4$ V, $I = -0.05$ mA, $t_{\text{meas}} = 20$ min
2) $f_{\text{lock-in}} = 0.5$ Hz ($f_r = 160$ Hz, $n = 320$), $V = 10$ V, $I = 8$ mA, $t_{\text{meas}} = 5$ min
3) $f_{\text{lock-in}} = 0.5$ Hz ($f_r = 160$ Hz, $n = 320$), $V = 12$ V, $I = 85$ mA, $t_{\text{meas}} = 5$ min
4) $f_{\text{lock-in}} = 5$ Hz ($f_r = 160$ Hz, $n = 32$), $V = -4$ V, $I = -0.05$ mA, $t_{\text{meas}} = 40$ min
5) $f_{\text{lock-in}} = 5$ Hz ($f_r = 160$ Hz, $n = 32$), $V = 10$ V, $I = 8$ mA, $t_{\text{meas}} = 5$ min
6) $f_{\text{lock-in}} = 5$ Hz ($f_r = 160$ Hz, $n = 32$), $V = 12$ V, $I = 85$ mA, $t_{\text{meas}} = 5$ min
7) $f_{\text{lock-in}} = 40$ Hz ($f_r = 160$ Hz, $n = 4$), $V = -4$ V, $I = -0.05$ mA, $t_{\text{meas}} = 120$ min
8) $f_{\text{lock-in}} = 40$ Hz ($f_r = 160$ Hz, $n = 4$), $V = 10$ V, $I = 8$ mA, $t_{\text{meas}} = 5$ min
9) $f_{\text{lock-in}} = 40$ Hz ($f_r = 160$ Hz, $n = 4$), $V = 12$ V, $I = 85$ mA, $t_{\text{meas}} = 5$ min.

At reverse bias (regimes 1, 4 and 7), only low parasitic currents flow over regions of low R_p, e.g. shunts. Therefore, the detected signal is quite low, leading to a comparably low *SNR* and thus, high measurement times. The application of reverse bias leads to damages on the series connection of thin film solar modules. This is visible in Figure 4.1; the hot spots in the reverse bias images do not match with the shunts in the forward bias images (except one shunt in cell 7). They lie at the series connections between the cells. This phenomenon is discussed in chapter 4.5. I recommend not to measure at reverse bias unless the damaging phenomenon is the aim of the investigation. For the evaluation of shunts, I recommend to measure at low positive biases.

At low positive biases (regimes 2, 5 and 8), recombination currents and currents over shunt resistances occur and become visible in LIT images. Depending on the bias voltage value, the recombination current J_{rec} is visible as a cell signal or not. The *SNR* is higher and the measurement time lower than at reverse bias.

In regimes at high injection currents (regimes 3, 6 and 9), the diffusion current flows and induces losses at the sheet resistance of the TCO layer. This results in a typical pattern in cell stripes of thin film modules, which is explained in chapter 4.3. The higher power dissipation in these regimes compared to other bias regimes enhances the *SNR* and lowers the spatial resolution.

Low lock-in frequencies (regimes 1, 2 and 3) yield a low spatial resolution, which is noticeable e.g. at the “halos” around shunts. Their broadening is high, as the heat has more time to spread compared to higher frequencies. Advantageous on low frequencies is the higher *SNR* and with that, shorter measurement time. A further disadvantage is the possible overlap with slow temperature transients.

Table 4.1: Measurement regimes for Vomo-LIT results of thin film solar modules. The gathered information, advantages and disadvantages of the regimes are compared by means of the visibility of resistance related defects (a), the spatial resolution (b), the signal-to-noise ratio SNR (c), the needed measurement time (d), and possible unwanted by-effects like slow overlapping temperature transients (e), problems with the evaluation due to the lock-in process (f) or possible damaging of the solar module (g).

	$V < 0$	$0 < V \leq V_{oc}$	$V > V_{oc}$
$f_{lock\text{-}in}$ < 1 Hz	**regime 1** a) reverse shunts (R_p) b) low c) low d) moderate e) probable f) not probable g) possible	**regime 2** a) shunts (R_p); recombination current I_{rec} (strong) b) low c) high d) low e) probable f) not probable g) unlikely	**regime 3** a) shunts (R_p); dark current I_{dark}; series/sheet resistance R_s b) low c) high d) low e) probable f) not probable g) possible at high currents ($I_{dark} >> I_{sc}$)
1 Hz < $f_{lock\text{-}in}$ < 10 Hz	**regime 4** a) reverse shunts (R_p) b) high c) low d) high e) not probable f) not probable g) possible	**regime 5** a) shunts (R_p); recombination current I_{rec} (moderate) b) high c) moderate d) moderate e) not probable f) not probable g) unlikely	**regime 6** a) shunts (R_p); dark current I_{dark}; series/sheet resistance R_s b) high c) high d) moderate e) not probable f) not probable g) possible at high currents ($I_{dark} >> I_{sc}$)
$f_{lock\text{-}in}$ > 10 Hz	**regime 7** a) reverse shunts (R_p) b) high c) low d) high e) not probable f) probable g) possible	**regime 8** a) shunts (R_p); recombination current I_{rec} (weak) b) high c) low d) high e) not probable f) probable g) unlikely	**regime 9** a) shunts (R_p); dark current I_{dark}; series/sheet resistance R_s b) high c) moderate d) high e) not probable f) probable g) possible at high currents ($I_{dark} >> I_{sc}$)

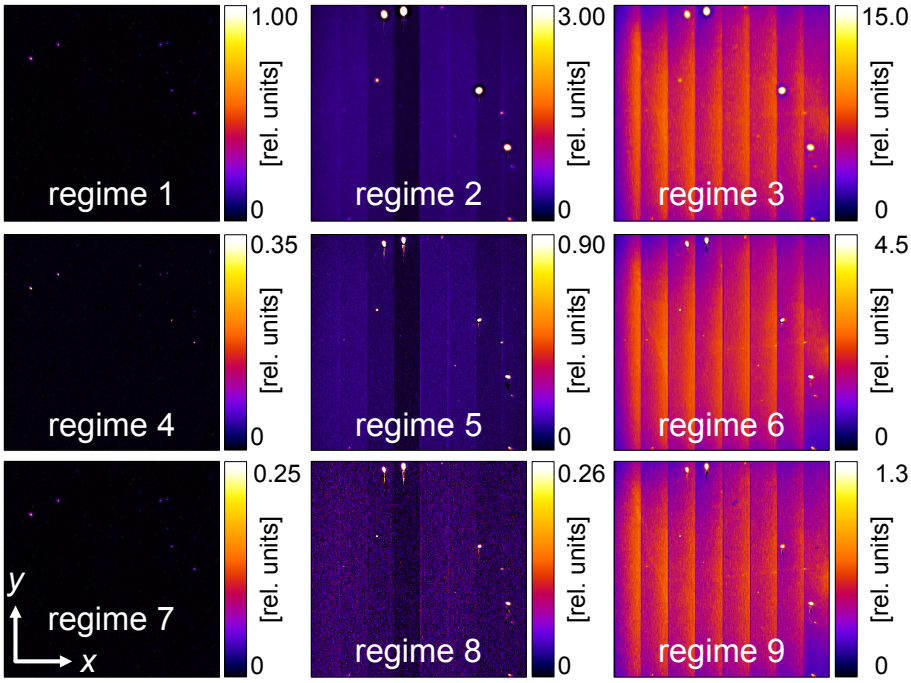

Figure 4.1: Vomo-LIT S^{-45° images of an a-Si module acquired in different measurement regimes. Main parameters in Vomo-LIT measurements are the lock-in frequency $f_{\text{lock-in}}$ and the applied bias voltage V. At reverse voltages, only parasitic currents via shunts are flowing (regimes 1, 4 and 7). At low forward biases, these shunts currents flow also and dominate the image. Depending on the bias voltage value, the recombination current J_{rec} is visible as a cell signal or not (regimes 2, 5 and 8). At high bias voltages, the diffusion current flows, making the sheet resistance of the front electrode of the solar module visible (regimes 3, 6 and 9). For low lock-in frequencies (regimes 1, 2 and 3), the spatial resolution is low, noticeable at the wide "halos" around shunts. The advantage of low frequencies is the higher SNR and thus shorter measurement time. Moderate frequencies from 1 *to* 10 Hz *(regimes 4, 5 and 6) are a compromise between good spatial resolution and high SNR / low measurement time. High frequencies (regimes 7, 8 and 9) show the best spatial resolution. For a sufficient SNR, long measurement times are needed.*

Moderate frequencies from 1 to 10 Hz (regimes 4, 5 and 6) find a compromise between good spatial resolution and high *SNR* / low measurement time. Furthermore, they give the most reliable reconstruction of the original signal with the lock-in process.

High frequencies (regimes 7, 8 and 9) show the best spatial resolution, but it does not increase much compared to moderate frequencies. Additionally, long measurement times are needed for a sufficient *SNR*. For quantitative evaluations, the sub-

sampling of the signal leads to problems with the original signal reconstruction with the lock-in process (see chapter 3.3.3). Therefore high frequencies deliver no advantages in most cases.

Summarizing, it can be stated that the parameter regimes have to be adapted to the aim of the LIT detection. For example, for the detection of shunts, a low voltage at moderate frequencies is recommended (regime 5). If the cell boundaries have to be displayed also, a moderate increase of V often helps due to an increase of the recombination current. The detection of series resistances only works out at high bias voltages. Here, the frequency should be moderate (not high) to show the cell signal strongly (regime 6). In principle, moderate frequencies show the best performance in most applications. For quantitative evaluations, always a moderate frequency should be chosen to avoid errors due to slow temperature transients (at low frequencies) and the problems with the signal reconstruction with LIT (at high frequencies).

4.2 Scaling of Vomo-LIT images

A way to quantify Vomo-LIT images is the application of a dissipated power density scale, replacing the scaling in relative units. Such a scaling is valid if the absolute induced power measured at the contacts P_{contacts} is dissipated completely in the module, i.e. no contact resistances occur, leading to $P_{\text{contacts}} = P_{\text{d}} = I_{\text{dark}} V$ (compare equation (2.24)). Furthermore, the whole device has to be visible in the Vomo-LIT image. Figure 4.2 shows a Vomo-LIT $S^{-45°}$ image of an *a*-Si module, taken at a bias $V = 6.3$ V, an injected current $I = 120$ mA, and a lock-in frequency $f_{\text{lock-in}} = 5$ Hz. The scaling is from 0 to 2 relative units.

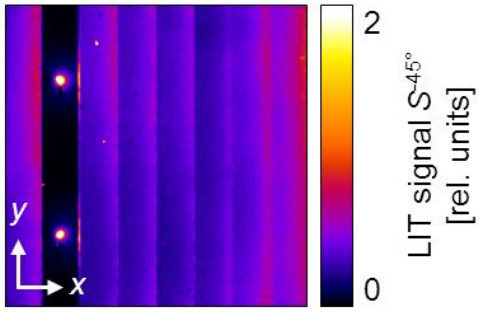

Figure 4.2: Vomo-LIT image of an a-Si module for power density scaling. The size of the module is $A_{\text{m}} = 64$ cm². *The image was taken at a bias* $V = 6.3$ V, *a current* $I = 120$ mA, *and a lock-in frequency* $f_{\text{lock-in}} = 5$ Hz. *The application of equation* (4.1) *leads to the conversion factor of* 32.6 mW/cm²/(relative unit), *giving the image pixels a power density scale from* 0 *to* 65.2 mW/cm².

To achieve the power density scale $p_{\mathrm{d}}^{\mathrm{x_0,\,y_0}}$ for the Vomo-LIT signal $S_{\mathrm{x_0,\,y_0}}^{-45^\circ}$ of an image pixel at x_0, y_0, following calculation has to be carried out: The integral sum of the S^{-45° signal $\sum_1^{N_\mathrm{x}} \sum_1^{N_\mathrm{y}} S^{-45^\circ}$ of the module's image, with N_x and N_y being the number of image pixels in *x* and *y* direction, has to be divided by the total number $N_\mathrm{xy} = N_\mathrm{x} \times N_\mathrm{y}$ of image pixels and multiplied with the module's area A_m (in this case, 64 cm²). The inverse of this value has to be multiplied with P_d (measured at the contacts) and the Vomo-LIT signal of the pixel $S_{\mathrm{x_0,\,y_0}}^{-45^\circ}$ to achieve the scaling value for $p_{\mathrm{d}}^{\mathrm{x_0,\,y_0}}$ in W/m², i.e.

$$p_{\mathrm{d}}^{\mathrm{x_0,\,y_0}} = \frac{N_{xy}}{\sum_1^{N_x} \sum_1^{N_y} S^{-45^\circ}} \frac{P_\mathrm{d}[\mathrm{W}]}{A_\mathrm{m}[\mathrm{m^2}]}\, S_{\mathrm{x_0,\,y_0}}^{-45^\circ}. \tag{4.1}$$

In the image in Figure 4.2, an overall power of $P_\mathrm{d} = V \times I_\mathrm{dark} = 756$ mW is dissipated and the number of pixels is in *x* and in *y* direction is $N_x = N_y = 496$, yielding a pixel number for the whole image of $N_{xy} = 246016$. Together with the integral sum of all image pixels $\sum_1^{N_x} \sum_1^{N_y} S^{-45^\circ} = 89182$, this yields the value of 326 W/m² = 32.6 mW/cm² for the LIT signal of an image pixel $S_{\mathrm{x_0,\,y_0}}^{-45^\circ}$. Thus, the dissipated power density scaling in Figure 4.2 is from 0 to 652 W/m² = 65.2 mW/cm². Please keep in mind that such a scale refers to areas of 1 m² or 1 cm², respectively, and not to the size of one image pixel. This means, the value of a pixel in the image does not correspond to the absolute power P_d in mW or W dissipated in its area, but the dissipated power per unit area p_d. A scaling for the absolute power P_d is also possible by leaving out the factor N_{xy}/A_m. in equation (4.1), i.e.

$$P_{\mathrm{d}}^{\mathrm{x_0,\,y_0}} = \frac{P_\mathrm{d}[\mathrm{W}]}{\sum_1^{N_x} \sum_1^{N_y} S^{-45^\circ}}\, S_{\mathrm{x_0,\,y_0}}^{-45^\circ}. \tag{4.2}$$

4.3 Analysis of local shunt and series resistances in thin film solar cells by LIT

The electrical influence of local defects, such as shunts or series resistances, is of large interest for every manufacturer of photovoltaic devices. LIT offers the possibility to characterize defects and – in limits – to quantify their electrical influence. For crystalline silicon solar cells, different types of shunts were found depending on their structural origins [81, 51, 82]. Several methods for the mapping of series resistances with LIT were proposed [52], but only one with combined EL measurements was verified to deliver quantitatively reasonable results [40].

Both types of defects – shunts and series resistances – are found in thin film silicon devices also, but they have different origins than the defects in crystalline solar cells. The origin of shunts is usually a direct short-circuit between front and back con-

tact and is investigated in the following chapter 4.4. Series resistances can occur due to inhomogeneous TCO layers, or if the contact between TCO and silicon malfunctions.

A quantitative access to calculate series resistances using LIT only has not been found yet; just qualitative measurements are possible [6, p. 214]. By combining LIT with EL measurements, a quantitative correct mapping of series resistances called RESI was achieved for crystalline solar cells [40, 41]. The application of quantitative EL measurements according to the reciprocity theorem [83] is – until now – only possible for solar cells that show radiative recombination with an ideality factor $n = 1$ [84, 85, 86]. This has not been proven for thin film silicon solar cells yet. Anyway, new proposed methods presented in chapters 7.3 and 7.4 may pave the way to a quantitative correct mapping of series resistance induced losses with LIT only.

The influence of shunts on a solar cell can be evaluated with the image proportionality method [79] combined with LIVT [76] measurements. Hereby, the LIT signal of a shunt is compared with the signal of its surrounding cell to obtain the percentage of the power dissipated in the shunts compared to the power dissipated in the cell. If this is carried out for several cell voltages, a relative power-voltage (*P/V*) characteristic of the shunt is derived. The method was applied to an *a*-Si module with led-out contact terminals as shown in Figure 2.4 on the right side. Figure 4.3 shows two shunted cell stripes (cell no. 3 and 4) of the module at different cell biases. The images were taken at a lock-in frequency $f_{\text{lock-in}}$ of 5 Hz and had a measurement time of $t_{\text{meas}} = 5$ min each. For a good comparability, all images are scaled to the same values from 0 to 5 relative units.

In both cells, the shunts dominate the image at low cell voltages, where the cells show a low signal. With increasing voltage, the cell signals start to increase according to the electrical influence of the shunts lying in the corresponding cells. The bigger the shunts' influence, the higher the applied voltage has to be to make the cell become active. This is due to the voltage collapse in the cell caused by the shunt. The shunt in cell 3 appears to be stronger than the one in cell 4, because it shows a markedly larger halo. To show this fact quantitatively, I used the above mentioned image proportionality method. This method states that the ratio of the dissipated power in the shunt $P_{\text{d}}^{\text{shunt}}$ to the dissipated power in the cell $P_{\text{d}}^{\text{cell}}$ equals the ratio of the integral signal $\int S^{-45^\circ}\, dA_{\text{shunt}}$ of the shunt area A_{shunt} to the integral signal $\int S^{-45^\circ}\, dA_{\text{cell}}$ of the whole cell area A_{cell} (including the shunt), i.e.

$$\frac{P_{\text{d}}^{\text{shunt}}}{P_{\text{d}}^{\text{cell}}} = \frac{\int S^{-45^\circ}\, dA_{\text{shunt}}}{\int S^{-45^\circ}\, dA_{\text{cell}}.} = \frac{S_{\text{shunt}}^{-45^\circ}}{S_{\text{cell}}^{-45^\circ}}. \tag{4.3}$$

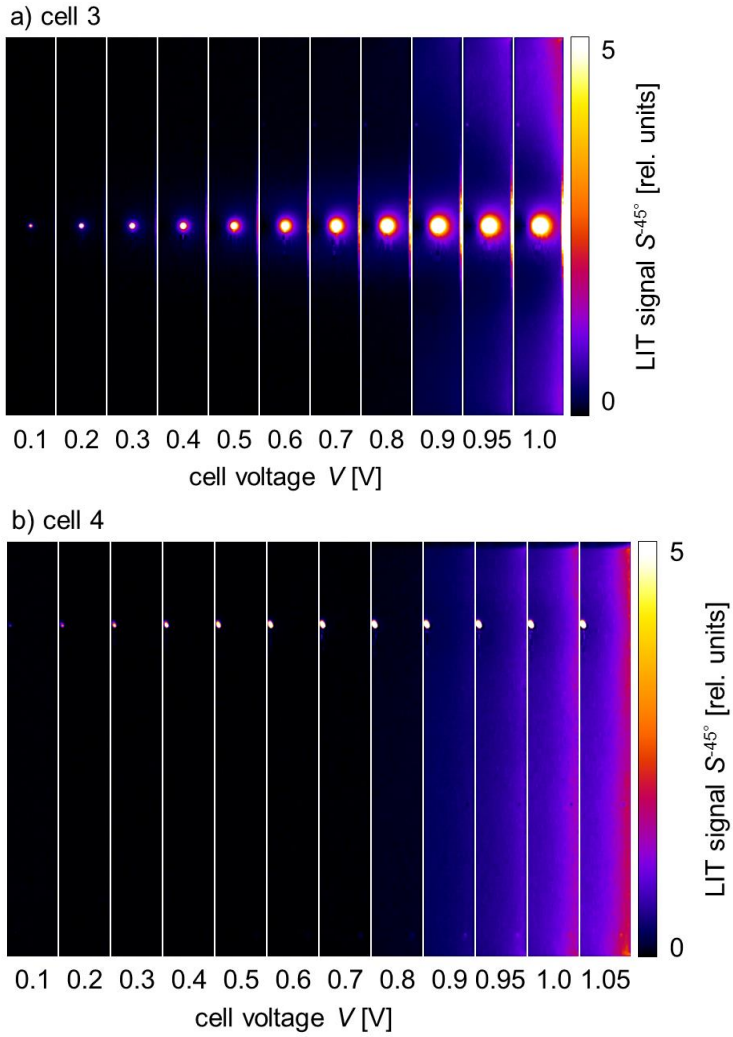

Figure 4.3: Vomo-LIT images of two shunted cell stripes of an a-Si module at different bias voltages. Both shunts dominate the LIT signal at low voltages. The shunt in cell 3 (a) is stronger than the one in cell 4 (b). This is indicated by two features: the larger halo around the shunt in cell 3; and the signal of the cell areas surrounding the shunts, where the surrounding of the shunt in cell 3 shows a markedly lower signal at high voltages. Above 0.9 V*, the current flow in the shunt in cell 4 does not increase.*

The proportionality method strongly depends on the choice of the shunt area A_{shunt}. Thus, a reasonable choice has to be made that fits for the shunt influence of all images at different biases. For example, a rectangular area around the shunt having a minimum signal of 10 % of the maximal shunt signal $S^{-45°}_{\text{shunt,max}}$ could be chosen. In the considered case, this approach leads to a shunt area of 10 × 10 image pixels for both

shunts. The ratio $S_{\mathrm{shunt}}^{-45°}/S_{\mathrm{cell}}^{-45°}$ for each cell voltage delivers the behavior shown in Figure 4.4 (a). The images at $V_c = 0.1$ V have such a low *SNR* that their results are not trustworthy. For $V_c < 0.8$ V (cell 3) and $V_c < 0.7$ V (cell 4), the ratio has a quite high value of above 60 % and 80 %, respectively, meaning that this amount of the cell current flows through the shunt. Beginning with 0.7 V / 0.8 V, the current flowing over the cell area increases, leading to a lower shunt-to-cell ratio. In case of the strong shunt in cell 3 it decreases to 45 %, in case of the shunt in cell 4 to 5 %. Thus, the relative influence of a shunt to its cell decreases with increasing bias voltage. This is important to keep in mind if the influence of a shunt is estimated. Single LIT images at one voltage only cannot deliver satisfying answers.

Further information about the shunt's electrical behavior is found when plotting its LIT signal $S_{\mathrm{shunt}}^{-45°}$ and the cell signal $S_{\mathrm{cell}}^{-45°}$ against the bias voltage and comparing them to the measured injected power at the contacts. This plot is shown in Figure 4.4b. For both cells, the injected power shows good congruence to the integral cell signals $S_{\mathrm{cell}}^{-45°}$, leading to the conclusion that contact resistances are negligible as assumed for the scaling of Vomo-LIT images in chapter 4.2. Hence, the shunts' P_d/V characteristic can be quantified using equation (4.3) solved to P_d^{shunt}.

A shunt *J/V* characteristic can be derived from the P_d/V characteristic with the assumption of a homogeneously distributed voltage V over the cell. This assumption is not valid in the close surrounding of the shunt, where a voltage breakdown occurs. Still, the assumption can give an approximate insight since the region considered is quite large compared to the actual shunt size (see chapter 5). The derived shunt *J/V* characteristics are illustrated in Figure 4.5 for the investigated shunts. Both characteristics show linear ohmic behavior. The shunt in cell 4 goes into saturation at voltages above $V > 0.9$ V. This is probably a side-effect of the high TCO sheet resistance, limiting the lateral current flow in the cell. Thus, a shunt's influence is limited to a certain surrounding, which would be larger for a lower sheet resistance.

Concluding, the proportionality method combined with LIVT delivers an estimation of the electrical influence of shunts *under dark conditions*. As the current paths of injection in the dark and extraction under illumination vary, the estimation cannot be conferred to estimations of a shunts' influence on the cell efficiency. This can work for solar cells with a voltage-independent photo current J_{ph} [87, 20, p. 37], but not for thin film silicon solar cells (see chapter 2.3). Thus, a realistic evaluation of the efficiency losses due to shunts in solar cells has to be carried out at real operation conditions: under illumination and at V_{MPP}. This is discussed in detail in chapters 7, 7.3 and 7.4.

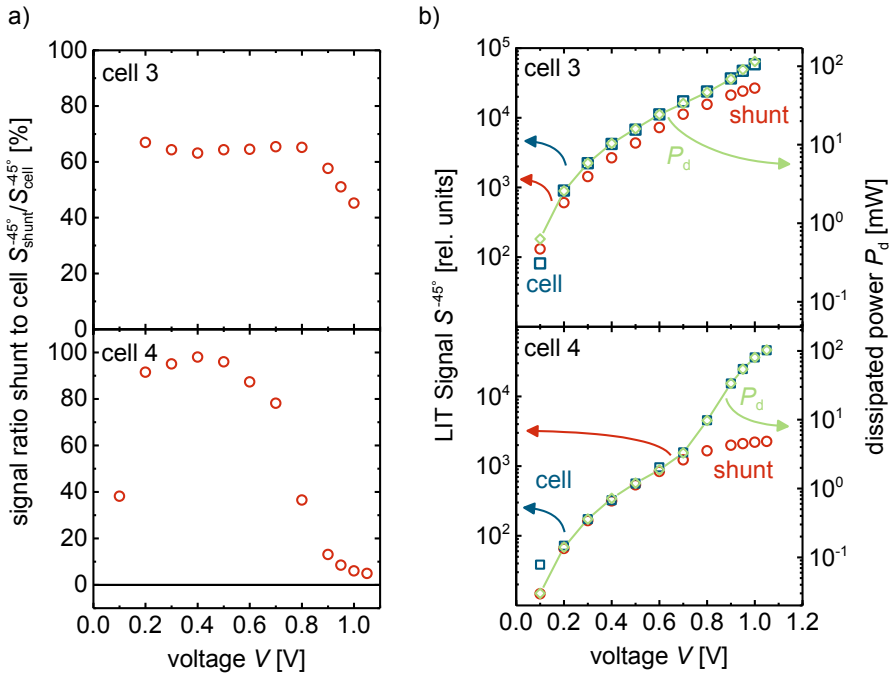

Figure 4.4: Electrical influence of shunts dependent on bias voltage. (a) The signal ratio from the integral signal of the shunt to the integral signal of the cell delivers the percentage of the shunt's influence on the power dissipation of the cell. The SNR of the images at 0.1 V *is too low for a reliable signal interpretation. Up to* 0.8 V *for cell 3 and* 0.7 V *for cell 4, the ratio shows high shares of the overall power dissipation with values above* 60 % *and* 80 %*, respectively. For higher voltages, the shunts' influence decreases strongly, especially in cell 4. (b) The integral LIT signal of the cells (blue squares) matches the injected power at the contacts (green rhombuses) well. The integral LIT signal of the shunts (red circles) follows the behavior of the dissipated power* P_d *at low voltages and diverges at higher voltages. Hence, it is proportional to the dissipated power* P_d *in the shunts according to equation (4.3).*

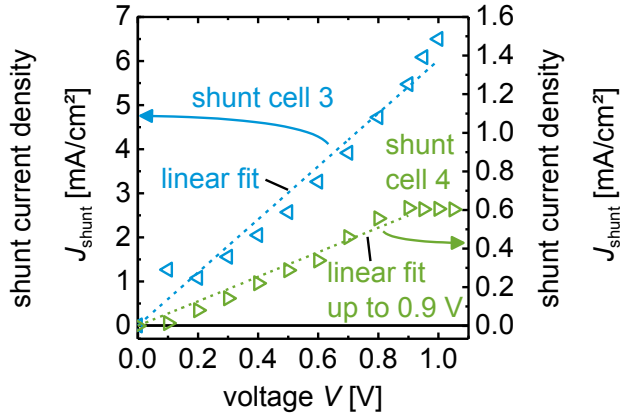

Figure 4.5: Shunt J/V characteristics derived from Vomo-LIT measurements. By dividing P_d/V characteristics of shunts (see Figure 4.4) by the applied voltage V, J/V characteristics of the shunts are calculated. Compared to the image dimensions, the actual shunt size is quite small, giving the method a justification if considered as a rough approximation to access the slope of the curve. Both shunts show linear ohmic behavior. The shunt in cell 4 goes into saturation, which is presumably due to the TCO sheet resistance limiting the lateral current flow in the cell.

4.4 Origin of shunts in thin film silicon solar cells

To reveal the structural origin of shunts in the cell area of thin film silicon solar cells, I investigated their local composition. For that, scanning electron microscopy (SEM) images were captured after milling trenches through the shunts with a focused ion beam (FIB) tool. The sample was an *a*-Si/*μc*-Si tandem module with the size of 8 × 8 cm² and eight major shunts lying in the cell area. For the sample preparation, I localized the shunts using LIT images captured with macro- and microscopic lenses as well as optical microscopy images. Figure 4.6 shows a macroscopic high injection current LIT image of the whole module with labels from "A" to "H" for the shunts (a), microscopic thermographic raw images of shunt H without (b) and with applied power (c), and an optical microscopy image of the same shunt (d). The structure of shunt H found in the optical microscopy image can be seen in the thermographic raw image, too. By applying a bias voltage, the actual electrical shunt within the visible structure is highlighted in the thermographic images.

After the localization, six shunts ("A", "B", "C", "E", "F", "H") were cut out on 1 × 1 cm²-pieces and a thin layer (in the range of several nanometres) of platinum was deposited. This was necessary for the following investigations by SEM. The SEM images of the shunts before the FIB milling process in Figure 4.7 show that over the whole shunt area the surface is lowered compared to the region around. Therefore, some mate-

rial underneath the surface must be missing. This can be evaluated from the FIB cuts: Figure 4.8 displays shunts A and H which are the largest ones with areas of roughly estimated 2000 µm² and 8000µm², respectively. Here the absorber layer, which is the thick grey layer in the figures, is missing completely over an extensive area. That means the front and back contact of the solar cell are directly short-circuited.

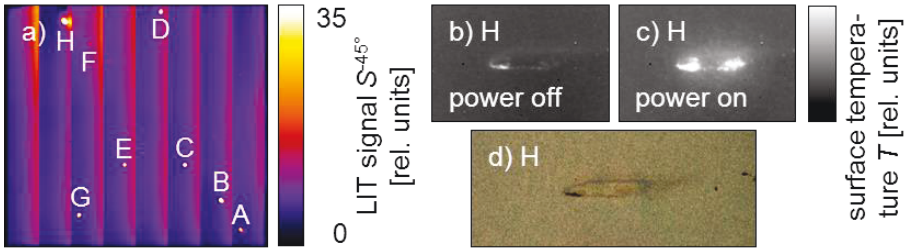

Figure 4.6: Shunts of a tandem module captured by LIT, raw thermography and optical microscopy. (a) shows the examined shunts in a macroscopic Vomo-LIT image. Shunt "H" is displayed in a raw thermographic image without (b) and with (c) applied power. Its structure is found in the optical microscopy image (d), too. The raw thermography image in (c) reveals the actual heat sources of the shunt, demonstrating that not the entire feature size is short-circuited.

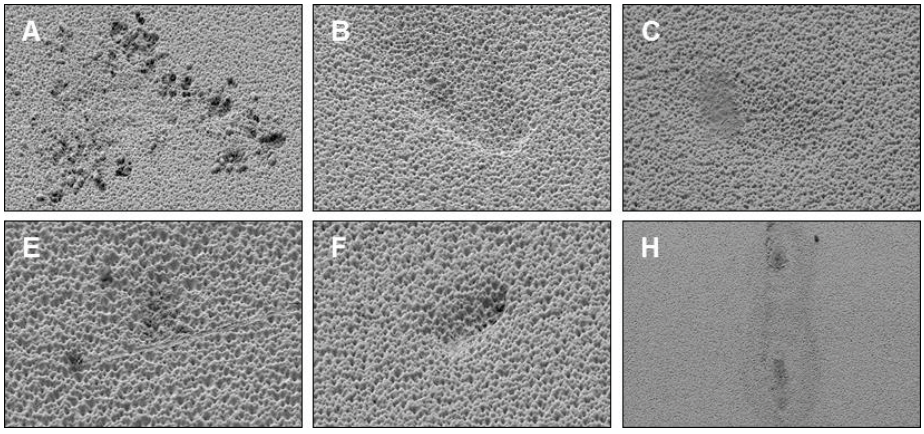

Figure 4.7: SEM images of investigated shunts. All shunt structures are clearly seen since the solar cell's surface is lowered at their sites. This indicates missing material. Shunts B, C and F look quite alike. Shunt A additionally has pellet-like looking features. In the region of Shunt E, a scratch is present. Shunt H has the largest dimensions and shows two dark spots on its surface, which probably are remains of the black spray paint used for emissivity enhancement.

This can also be seen when looking at the surface structure: In the shunted region, the surface texture of the TCO – which is dominated by crater-like structures – can be seen. In contrast to that, at the not-shunted regions, the surface looks 'chubbier'. The smooth substance on top of parts of shunts H might be some remains of the black spray paint which was used to enhance the emissivity of the back contact during the LIT experiments (see chapter 4.7).

Shunts B and C look somewhat different, as pointed out in Figure 4.9. The absorber layer is very thin in an extensive area, but a direct short-circuit seems to be at several small points only. Additionally, some sort of substance can be found at some points between the glass and the TCO, which does not allow the layers to grow in a way that the cell would be well-functioning. Cracks, voids and air inclusions can be seen at these points as well as again some remains of the paint at shunt C.

Shunts E and F are the smallest shunts of the investigated ones with areas of approximately 70 and 60 µm². Figure 4.10 shows SEM images of them. It seems as if the actual short-circuits are at small points, too, and the absorber layer is very thin over a larger area.

In summary, all shunts show at least a small direct contact area between front- and back contact and an extensively missing absorber layer (even if a thin layer remains). The most probable process for the origin of shunts in cells lies according to deposition engineers in the non-perfect vacuum process for the fabrication of thin silicon films, which is done by PECVD. During the deposition, small particles that are left in the vacuum may lay down on the substrate. At these points, the layer either cannot be deposited, or only is under strong mechanical strain. Therefore, the silicon flakes of there, especially if the substrate undergoes a rapid temperature change, for example when it is taken out of the hot PECVD chamber (ca. 150 to 200 °C) quickly into room temperature. The same happens at areas with impurities between glass and TCO: the impurities prevent the TCO from being built up and therefore put mechanical strain on the thin layers. If the parts where the silicon flaked off are not isolated in an additional process, i.e. the back contact is deposited immediately after the PECVD, direct contacts between front TCO and back metal contact are created.

The statistical basis of this investigation is small, as only six shunts were explored. In principle, it could also happen that e.g. small metal particles in the PECVD chamber are deposited at small spots at the sample and build a direct contact between front- and back contact. Therefore, general conclusions cannot be drawn out of this investigation, but the experience of the deposition and characterization team at IEK-5 points in the direction, that the described processes are the ones which produce most of the shunts in cell areas.

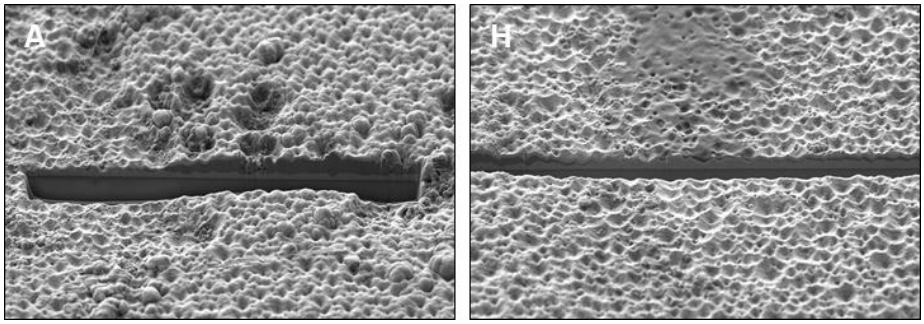

Figure 4.8: SEM images of FIB-cuts through shunts A and H. The contrast of the images allows to distinguish the glass superstrate (thick layer from the bottom), the front TCO (bright layer above the glass), the silicon absorber layers (dark grey layer), and the final silver back contact (bright gray). In both shunts, the absorber layers are missing in an extensive area. Hence, the back contact is directly connected with the front contact layer, causing a direct short-circuit.

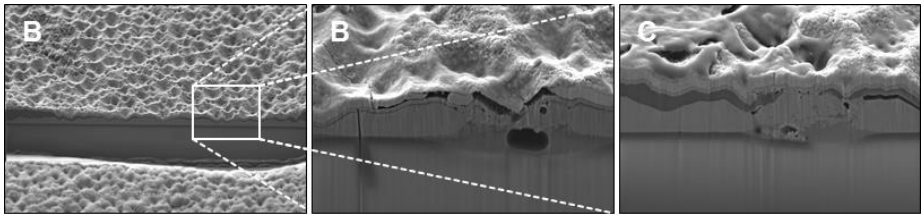

Figure 4.9: SEM images of FIB-cuts through shunts B and C. In contrast to shunts A and H, both shunts have a very thin absorber layer left. Direct short circuits can be observed at small spots, where a contamination between glass and TCO is visible. The contamination hampers the TCO to build up a regular structure and induces cracks and voids in the TCO as well as between all layers.

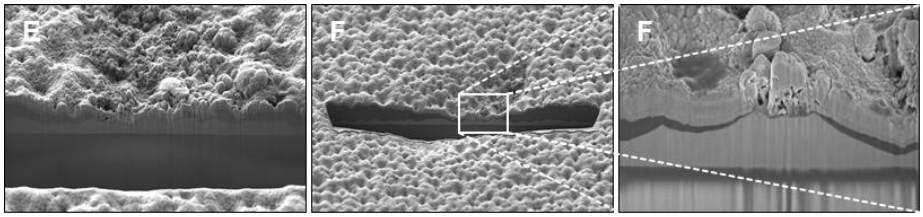

Figure 4.10: SEM images of FIB-cuts through shunts E and F. These shunts had the smallest areal dimensions of all investigated shunts. The absorber layer is thinned strongly, comparable to shunts B and C. The short-circuits occur at small sites also, but no indications for contaminations between glass and TCO are found.

For several solar cell technologies, shunts have been categorized and characterized by their *J/V* behavior deduced from LIVT measurements using the proportionality method as shown in chapter 4.3. This is justified by differing structures and origins of these shunts. If the results of this chapter turn out to be representative, then most shunts in the cell area of thin film silicon solar modules have the same origin. This would lead to the conclusion that a categorization of shunts is redundant. Furthermore, the shunt’s share on the current flow in their cell is then probably only dependent on the size of the direct contact area of front and back electrodes.

4.5 “Shunt bursting” – consequences of reverse voltage biasing on thin film silicon solar cells

Reverse voltage biasing can occur on solar cells in a module relative easily due to partial shading [88], low (inhomogeneous) illumination, or low module voltage [89, p. 83]. As diodes, solar cells can bear a reverse voltage up to certain values, where break-through mechanisms start to work [45, 90]. For crystalline silicon solar cells, these values are known and were investigated intensively in the last years [91, 92, 93]. For thin film solar cells, several theoretical approaches for the description of shunts under reverse [94, 95, 96] and forward bias [97] were introduced. Some investigations on shunts were made using imaging methods [12, 13, 14, 15, 16, 17, 98]. Still, it is not clear how a temporary reverse bias on thin film silicon solar cells leads to damages, i.e. new shunts.

A method for the usage of reverse biasing in the field of thin film silicon solar cells already exists: the so called “shunt busting/bursting/curing/removal” [99]. The idea is to apply a reverse bias to a shunted solar cell so that the shunt would be “burned out” or removed. This method was used in industry and labs, improving cell efficiencies of shunted cells moderately. Anyway, the physical mechanism behind this phenomenon is not clear; Dongaonkar et. al. assume that current paths due to aluminum diffusion from the TCO (which is usually aluminum-doped) arise [99].

I investigated the formation of shunts under reverse bias in a simple experiment with the LIT setup. A solar cell in a thin film silicon module with led-out contacts (see Figure 2.4 on the right) was contacted separately and first measured at several forward biases. The forward bias results are the ones of cell 3 in Figure 4.3a. Then, a reverse voltage was applied and stepwise increased up to -1.0 V (-1.5 × V_{oc}) inducing a reverse current flow of -10.5 mA/cm² (-1.1 × J_{sc}). After reverse biasing, the measurements with forward bias were repeated. Figure 4.11 displays the $S^{-45°}$ LIT signals while reverse biasing (a) and the repeated forward bias measurements (b).

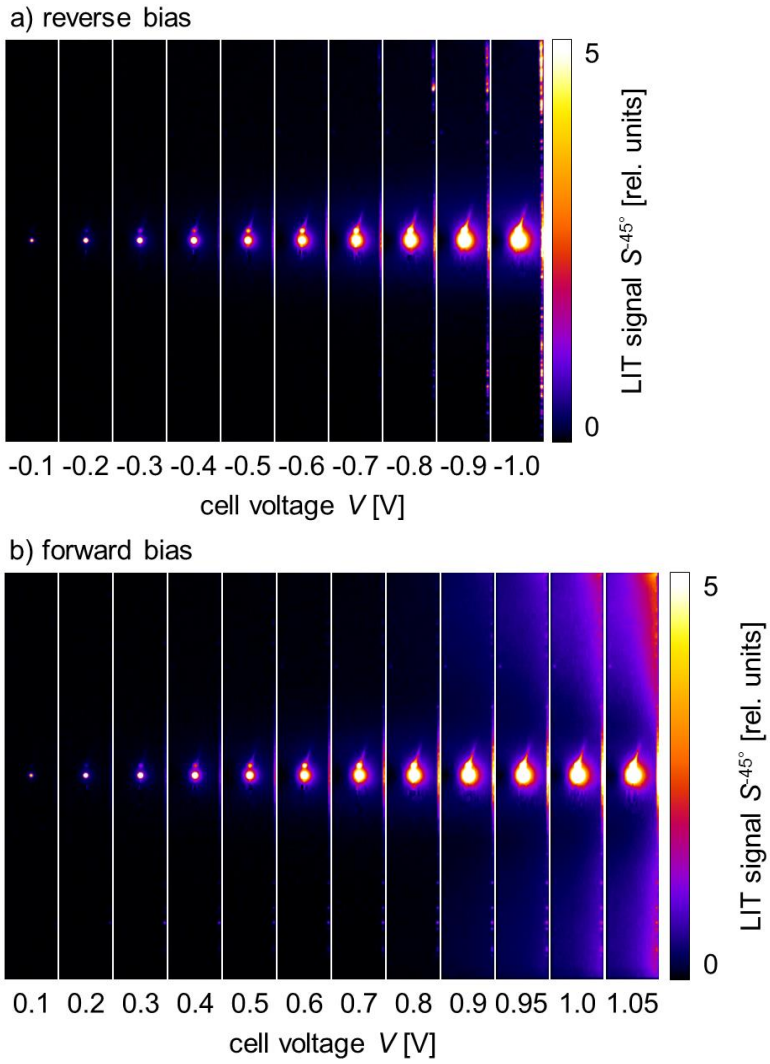

Figure 4.11: Vomo-LIT series of an a-Si cell stripe. The measurements were carried out on the same cell as described in Figure 4.3. A series with reverse biases (a) was carried out and then forward bias measurements were repeated (b). In the images of the first forward bias series, no shunts on the series connection on the right side of the images are found except in the intermediate region of the stripe's height. While applying reverse bias, these edge shunts appear over the entire length of the series connection. Additionally, a second shunt above the first one emerges, including a "tail". In the images of the second forward bias series, all these shunts remain visible.

The reverse bias measurement shows changes in the cell at a low reverse voltage of -0.2 V already. A second shunt emerges above the first one. With increasing reverse voltage, it develops a "tail" that propagates upwards. From -0.8 V, new shunts at the

series interconnection at the right margin of the cell become visible. That means the high strain due to the reverse voltage creates new current paths across the series connection.

The repeated forward measurement demonstrates that the new induced shunts above the first one and at the series connection contribute to the current flow in forward direction. This can be seen in the comparison of the shunt share on the cell signal shown in Figure 4.12a, which decreases slightly after reverse biasing. Thus, the damages due to the reverse biasing seem to be irreversible and permanent. Comparing the current values before and after reverse biasing for the same voltages in Figure 4.12b, it is found that the current decreases strongly. The diode character of the cell previously seen at voltages above 0.8 V vanishes, leaving a hardly explainable characteristic with possibly transient behavior from 0.7 V to 0.9 V. This damaging of the cell leads to a probably permanent poorer cell efficiency.

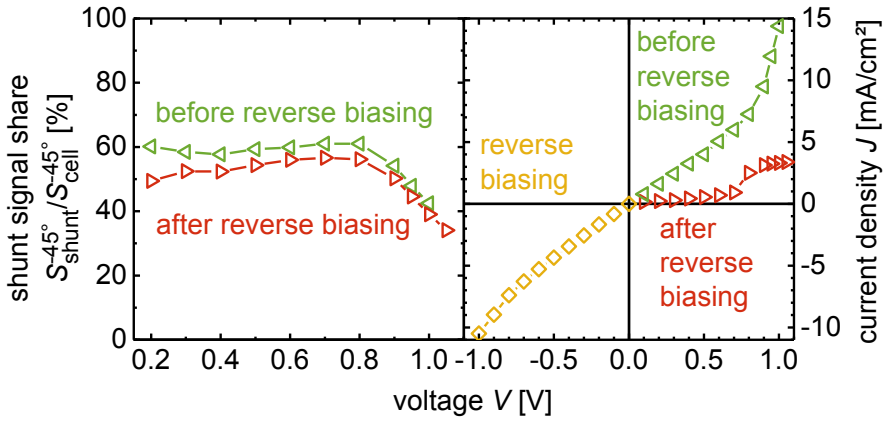

Figure 4.12: Comparison of cell characteristics before and after reverse biasing. a) The signal share of the previously existing shunt on the cell signal decreases slightly after reverse biasing, since new shunts occur and contribute to the current flow. b) The J/V characteristic of the cell at reverse bias measurements is linear. After reverse biasing, the characteristic is degenerated with strongly lowered current values.

So how does this assumption fit to the shunt bursting experiences? My presumption is that shunt bursting only works with some shunted cells, where one or few huge shunts cause the entire cell current to flow through them; even at high bias voltages (as seen in chapter 4.3, a shunt’s influence usually decreases with increasing cell bias). With applying a reverse bias, the creation of many comparatively smaller shunts at the series interconnection “opens” new current paths. They enable the cell current to partly avoid the huge shunts and increase the overall cell efficiency. This would explain the improvement of the cell efficiency. Further measurements of “healthy” and shunted

cells under illuminated conditions combined with cell efficiency measurements could prove these assumptions. The investigation of the new created shunts with microscopic LIT measurements (and eventually advanced SEM and/or FIB measurements) could reveal which laser scribed line (P_1, P_2, or P_3) is affected by the shunts and how the so introduced parasitic current flow occurs.

4.6 Basic Limo-LIT measurement techniques used on thin film solar modules

Limo-LIT enables the investigation of solar cells and modules under operation conditions, in contrast to Vomo-LIT that is carried out without illumination. For exact measurements, the illumination needs to be homogeneous and have a high irradiance to reach the MPP. Illumination sources that meet these requirements are very cost-intensive. So often a compromise between the illumination's homogeneity and its irradiance has to be made. At IEK-5, we use a LED panel described briefly in chapter 3.4.1. It reaches the required high irradiance but shows a moderate illumination homogeneity that becomes directly visible in Limo-LIT images. Figure 4.13 shows several $S^{-45°}$ LIT images of an *a*-Si solar mini-module taken at $f_{\text{lock-in}} = 5$ Hz. Table 4.2 lists the corresponding measurement parameters.

All Limo-LIT images contain a high contribution due to thermalization[5], which depends on the homogeneity of the illumination source. In Figure 4.13a, b, and c, this dependence is seen in a radial gradient from the modules center to the edges. The second contribution to the heat generation is the power generated by charge carriers passing the p/i/n-junction. Both heat generation effects are discussed for p/i/n-junction solar cells in detail in chapter 2.4 and for p/n-junction solar cells in [6, p. 44]. In the present example, the magnitude of the contributions can be estimated as follows:

For the illumination, blue LEDs with a peak wavelength of $\lambda = 450$ nm was used. This corresponds to an energy $h\nu = 2.7$ eV for each single photon. The band gap of *a*-Si (neglecting tail states [100]) is approximately $E_g = 1.7$ eV. According to equation (2.14), the heating contribution of thermalization is thus $p_{\text{th}} = 15$ mW/cm², independent of the applied voltage. The overall heating at V_{oc} and J_{sc} according to equation (2.19) is $p_{\text{ill}}^{\text{add, } J_{\text{sc}}} = p_{\text{ill}}^{\text{add, } V_{\text{oc}}} = 40.5$ mW/cm². Thus, the contribution of the current flow J_{ph} at V_{oc} and J_{sc} is the difference $p_{\text{ill}}^{\text{add, } J_{\text{sc}}} - p_{\text{th}} = 25.5$ mW/cm². Hence, thermalization contributes to 37 % to the overall heating at V_{oc} and J_{sc}. At MPP, the relative contribution of the thermalization is moderately higher, as the overall dissipated power P_{d} is reduced by the amount of the extracted power P_{ext}.

[5] Note: The contribution of the thermalization can be minimized by using an illumination with monochromatic light with a photon energy close to the band gap of the investigated solar cell material.

Table 4.2: Measurement parameters applied voltage V and measured current J at the contacts for LIT images shown in Figure 4.13.

	measurement type	V [V]	J [mA/cm²]
a)	Limo-LIT@J_{sc}	0	-15
b)	Limo-LIT@MPP	3.5	-10
c)	Limo-LIT@V_{oc}	5.3	0
d)	Vomo-LIT	6.3	15

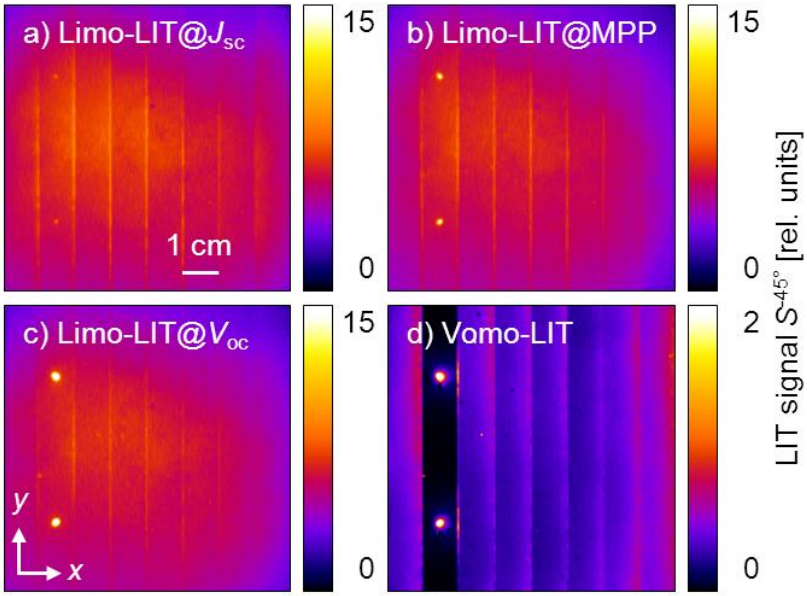

Figure 4.13: Comparison of Limo-LIT and Vomo-LIT images of an a-Si solar module. All images are taken at a lock-in frequency $f_{lock\text{-}in}$ = 5 Hz. For all Limo-LIT images, a LED source with blue LEDs (λ = 450 nm) was used with an irradiance E = 634 W/m². This led to the same short current density of J_{sc} = 15 mA/cm² as measured under standard test conditions at a sun simulator. All Limo-LIT signals show a gradient from the edges to the center, which originates from the inhomogeneity of the irradiance. Compared to Vomo-LIT, the Limo-LIT signal is stronger due to the higher dissipated power induced by the powerful irradiance. Furthermore, the Limo-LIT signal contains a large share (37 % at V_{oc} and J_{sc}) from thermalization. This effect does not occur in dark conditions. In the Limo-LIT images, the shunts in the second cell from the left show an increasing halo with decreasing current flow (J_{sc} to MPP to V_{oc}). Reciprocally, the signal of the series connection between the cell stripes rises with rising currents. The higher cell stripe signals of the shunted cell in b) and c) and the cell strip on the right in a) compared to the neighboring cell stripes originate from higher cell voltages.

According to this estimation, over the half of the Limo-LIT signal has to stem from charge carriers recombining over the p/i/n-junction. The location in *x*-*y*-direction where charge carriers recombine depends on the applied voltage as explained in chapter 2.4. At V_{oc}, where no overall current flows, the carriers can move broader in *x*-*y*-direction than in conditions, where a strong current flows (e.g. at J_{sc} or MPP). This effect is visible at the shunts in Figure 4.13a, b, and c. Their halo is largest at V_{oc} due to the higher lateral mobility of the charge carriers. At J_{sc} they are forced in the direction of the current flow described in chapter 2.4.

Compared to the Vomo-LIT image in Figure 4.13d, the Limo-LIT at MPP and J_{sc} show no clear pattern – i.e. a gradient over the cell stripes in *x* direction – stemming from the TCO sheet resistance. Yet, a slight gradient gets visible when integrating the signal values of the images in *y* direction and plotting the integrated values over the *x* direction. This plot is depicted in Figure 4.14. It shows all integrated signals of the images from Figure 4.13. A slope over all cells is seen in the Limo-LIT signals, which stems from the inhomogeneity of the irradiance. When looking at the signal differences between the neighboring edges of cells, it shows that the signal differences from Limo-LIT at V_{oc} and at MPP are smaller than at J_{sc}. Thus, the series resistance can be made visible at high flowing currents, yet needing a very homogeneous irradiance for quantitative evaluation. A way to overcome the difficulties with the homogeneity of the irradiance and gaining quantitatively evaluable information is described in chapters 7 to 7.4.

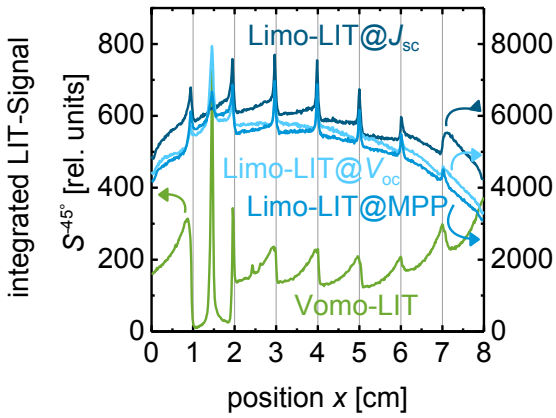

Figure 4.14: Comparison of integrated linescans of the Limo-LIT and Vomo-LIT images from Figure 4.13. The values are gained by integrating the image signals over the y-axis and plotting the integral values over the x-axis. The Vomo-LIT signal is lower by a factor of about 15 *to* 600*. The shunts at x* = 1.5 cm *have a strong impact on the signal as they cause a voltage breakdown in the cell. The Limo-LIT signal of the shunts is far less pronounced.*

The last distinctive effect seen in the Limo-LIT images is the signal at the series connections between the cell stripes. In all Limo-LIT images it is higher than the signal of the cell stripes. With increasing current flow, the series connection signal raises also, as Figure 4.14 illustrates. I assume an overlap of two effects here: The principal increase – seen in Limo-LIT@V_{oc} also – originates from the line P_3 (see chapter 2.1), which opens the back contact and the silicon layer. Therefore, the black paint used to enhance and homogenize the emissivity of the back metal lies directly on the TCO. It absorbs the incoming light and heats up stronger compared to its surrounding, where the light is mostly absorbed by the silicon layers. Hence, this effect is due to the measurement set-up and has no electrical origin. The second effect is the current flow over the connection line P_2, which forms the series contact between the front and back electrodes of neighboring cell stripes. With increasing current flow, the signal of the P_2 line increases also. As the spatial resolution of the Limo-LIT images cannot resolve the three laser scribed lines P_1, P_2, and P_3, both described effects overlap.

In chapter 4.3, the quantitative evaluation of the influence of shunts on the cell / module performance is discussed for Vomo-LIT measurements. The results presented there show that a realistic estimation of the shunt's influence cannot be carried out without illumination. This is also obvious from Figure 4.14 when comparing the Vomo-LIT and Limo-LIT signals at the site of the shunts (position x = 1.5 cm): The Vomo-LIT would strongly overestimate the shunt's influence. In operation, solar modules are driven at MPP. Thus, Limo-LIT@MPP should enable the realistic evaluation of the influence of shunts. However, the Limo-LIT@MPP signal is strongly affected by the homogeneity of the irradiance and contains a high contribution of thermalization. This hampers the interpretation of all Limo-LIT signals. A possible way to yield interpretable results would be the application of a very homogeneous illumination source and a mathematical correction for the thermalization. This is very cost- and labor-intensive. An approach to gain insight in the influence of shunts at operation conditions – even with a light source not matching the requirements on irradiance homogeneity – is presented in chapters 7 to 7.4.

4.7 Detecting LIT signals through glass encapsulation

Thin film solar modules are deposited on sub- or superstrates as shown in chapter 2.1. For outdoor durability, they are covered with a laminate foil and capsuled with a glass panel. Thus, when industrial thin film solar modules are measured by LIT, the thermographic camera has to capture the radiation of the solar module through the glass panel. The same applies to solar modules in superstrate configuration also. This comprises that the infrared radiation produced in the module has to pass the glass before being detected by the LIT system. The glass absorbs parts of the radiation and reemits

them, resulting in a reduction of the potentially acquired LIT signal of a solar module without glass panel. As the emission from a point of the solar module's surface goes into the half space $\Phi = \int_0^{2\pi} d\varphi \int_0^{\pi/2} \cos\theta \sin\theta \, d\theta = \pi$ and is refracted at the glass-air interface, the spatial resolution of the radiation measured outside the glass is lowered compared the radiation of the surface of the solar module. The resulting LIT images therefore may look "blurred".

CIGS solar modules, e.g., do not have to deal with this problem, as they are deposited on a substrate, so that the light couples in from the uncovered side. However, the surface does not necessarily have a homogeneous emissivity. Therefore, the LIT signal can inherit contrasts not stemming from temperature differences. Silicon thin film solar cells usually are made in superstrate configuration, but can be imaged from the back side if they are coated with black paint. This enhances the back metal emissivity strongly and delivers a homogeneous emission with best spatial resolution. The paint could be applied to CIGS modules also for an enhancement of the emission's homogeneity.

In the following, the differences of the LIT image acquisition through the glass side and from the coated back side are discussed by the example of a shunt in an *a*-Si solar module measured with Vomo-LIT. Figure 4.15 displays the linescans of the signals $S^{0°}$ and $S^{90°}$ through the shunt, representing the heat diffusion from the shunt's center.

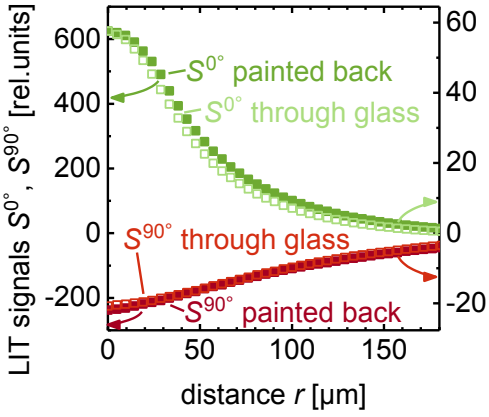

Figure 4.15: Comparison of LIT signals of a shunt in an a-Si module acquired through a glass panel and from the painted back side. The plot is fitted to match the respective maxima of the $S^{0°}$ signals. The glass panel dampens the infrared radiation originating from the solar module with the factor 10.8. *The slope of both curves is nearly identical.*

Open squares display the measurement through the glass superstrate; filled squares the measurement of the painted back side. The plot is fitted to match the respective maxima of the $S^{0°}$ signals. A measurement frequency of $f_{\text{lock-in}} = 20$ Hz was used. The maximum $S^{0°}$ signal is 625 relative units for the measurement from the painted back side and 58 relative units for the one through glass; hence the damping factor of the glass is about 10.8. Their slope of the curves of both measurements is nearly identical. This proves that the emission into half space and refraction at the glass surface does not induce a blurring of the LIT signal.

To verify that the measured radiation through the glass superstrate originates from the solar module and not from the glass surface, I coated the front glass and measured the radiation from the glass surface above the shunt. The result of this measurement is shown in Figure 4.16. For comparison, a measurement of the signals acquired from the solar module through the glass superstrate is depicted also. Both Vomo-LIT measurement were carried out with a measurement frequency of $f_{\text{lock-in}} = 4$ Hz. The plot is fitted to match the respective minima of the $S^{90°}$ signals.

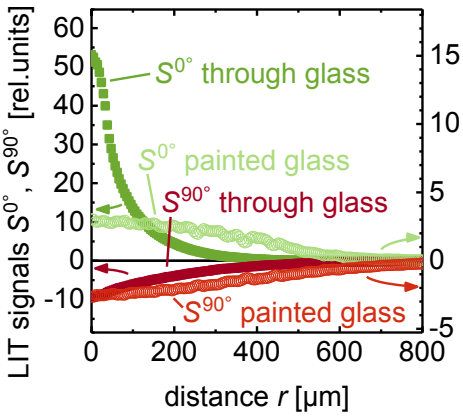

Figure 4.16: Comparison of LIT signals of a shunt in an a-Si module acquired through a glass panel and from the painted glass surface. The signal of the painted glass surface is broader and lower (by a factor of 17.4*) than the signal measured through the uncovered glass panel.*

The signals of the painted glass surface are broader than the signals measured through the unpainted glass and lower by a factor of 17.4. Thus, the signal acquired through the unpainted glass originated from the solar module. That means the disadvantage of the measurement through a glass panel is the dampening of the radiation emitted by the solar module. This results in a lower *SNR* when measuring through a glass compared to measuring the painted back side (for the same measurement time). If a comparable *SNR* as in the measurement of the coated back side is needed, a longer

measurement time has to be used. Yet, the dampening makes it difficult to measure at low injection currents as the LIT signal is very low then. This can only be overcome by using lower lock-in frequencies or by injecting higher currents if a measurement from a not encapsulated side is not possible.

5 Simulation of the theoretical LIT signal of thin film solar cells

A profound understanding of the complex LIT signal S of thin film solar modules can only be gained by comparing theoretical simulations with acquired LIT measurement results. The simulations presented in this chapter are based on the analytical approach of calculating the heat diffusion differential equation of an oscillating point heat source on the surface of a solid body representing the solar cell. The simulation results find criteria for a consistent acquisition of the signal phase.

5.1 Thermal model of thin film solar cells and calculation of the heat diffusion differential equation

LIT is limited to the detection of sample *surface* temperatures. As the signal stimulus can principally occur at different depths in the sample, the temperature distribution within the sample depends on its geometry and boundary conditions (e.g. heat exchange with the medium surrounding the sample) in all three space dimensions x, y and z. Furthermore, the temperature distribution depends not only on space, but also on time t. That means, LIT deals with a four-dimensional physical problem, but only measures three dimensions: The surface temperature of the sample, depending on surface position x, y, and time t. For an uncoupling with the help of calculations, the third space dimension z has to be taken into account. The surface temperature field can be calculated by solving the heat diffusion differential equation. The equation needs a thermal model of a solar cell.

Here, I investigate the simplest case of a heat source, which is a point heat source on the upper surface of the sample periodically stimulated with $f_{\text{lock-in}}$. The sample's geometry can be modeled by a stack of functional layers, each including its respective thermal behavior, i.e. thermal conductivity λ, mass density ρ and specific heat capacity c_p. Additionally including the layer thickness d results in four parameters for each layer. The thermal quantities can be summarized in the thermal diffusivity $D = \lambda/\rho c_p$, leaving two parameters per layer, D and d. To reduce complexity, I chose the simplest possibility for a model: a cuboid with extended dimensions in x and y direction and a small dimension in z direction as illustrated in Figure 5.1. The different functional layers of a thin film solar cell are neglected and seen as one homogenous medium with a certain thermal behavior. This leaves only two parameters for the cuboid model: the thermal diffusivity D and the thickness d in z direction. A more detailed approach is a two layer model with a solid cuboid representing the glass sub- or superstrate and a

very thin layer on its top representing the solar cell. The different heat conductivities and capacities as well as the different mass densities of the glass and the solar cell are regarded in such a model. It is discussed intensively in ref. [101] along with a comparison to the simple model. In the following chapters, I show that the simple model describes the thermal behavior of thin film solar modules on glass adequately.

Combined with the chosen lock-in frequency $f_{\text{lock-in}}$ of the LIT measurement, the thermal diffusion length

$$\Lambda = \sqrt{\frac{\lambda}{\rho c_{\text{p}} \pi f_{\text{lock-in}}}} = \sqrt{\frac{D}{\pi f_{\text{lock-in}}}} \tag{5.1}$$

defines the spatial resolution of the resulting LIT image. If Λ is smaller than the dimension that one pixel of the image depicts, then the heat diffusion will not play a role in the evaluation of LIT signals. In evaluations at laboratory scale, Λ can be larger than the dimension of one camera pixel and therefore hampers the analysis of small structures and defects. If several heat sources are present within Λ, it is hard to distinguish between them. An example for thin film solar modules is the investigation of scratched or laser-scribed integrated series connections between cells as will be shown in chapter 6.2.

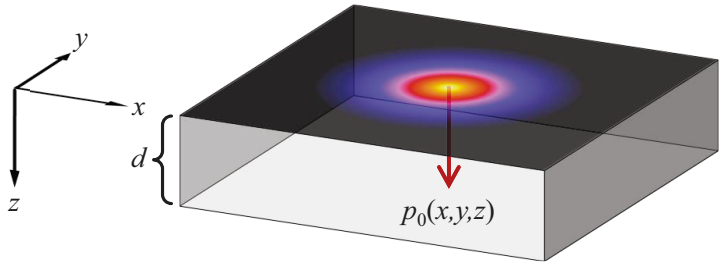

Figure 5.1: Thermal model of a thin film solar module. The module is seen as a solid with finite dimensions in x and y direction and a finite thickness d << x, y. The differing thermal behavior of the thin layers and the glass are neglected and the whole compound is described by one value each for its thermal conductivity λ, mass density ρ and specific heat capacity c_p. These three quantities are summarized in the thermal diffusivity $D = \lambda/\rho c_p$. The model assumes a point heat source at the upper surface of the body that is stimulated periodically and induces a power flow p_0 in all directions.

There are principally two ways to calculate the heat diffusion of an oscillating point heat source: Either using the mirror source method [6, p. 115] in real space or cal-

culating the point spread function (PSF)[6] [101] in Fourier space. They differ in the way they treat the source: In the mirror source method, the value in the center of the source is infinitely high. The PSF finds a finite value for the source center. Therefore, the PSF calculation is physically more realistic and will be described in the following.

As explained, a solution is needed for the three-dimensional heat equation for a periodic excitation with angular frequency $\omega = 2\pi f_{lock-in}$ [102, p. 56]. The solution for the temperature (difference) ΔT has to fulfill

$$\frac{\lambda}{\rho c_p}\left(\frac{\partial^2}{\partial x^2}+\frac{\partial^2}{\partial \mathrm{y}^2}+\frac{\partial^2}{\partial z^2}\right)\Delta T = \frac{\partial}{\partial t}\Delta T = i\omega\Delta T. \tag{5.2}$$

The Fourier transform method [101] makes use of the fact that the (spatial) partial differential equation given by equation (5.2) transforms into a simpler algebraic equation in the (spatial) frequency domain. In the following the two-dimensional Fourier transform with respect to the coordinates (x, y)

$$\hat{T}(k_x, k_y, z) = \frac{1}{2\pi}\iint \Delta T\,(x, y, z)\; e^{-ik_x x}\; e^{-ik_y x} dk_x dk_y. \tag{5.3}$$

is considered. Then, equation (5.2) transforms into

$$D\left(-k_x^2 - k_y^2 + \frac{\partial^2}{\partial z}\right)\hat{T}(k_x, k_y, z) = i\omega\hat{T}(k_x, k_y, z), \tag{5.4}$$

where k_x, k_y are the spatial wavenumbers corresponding to the coordinates x, y. Reorganization of equation (5.4) yields the ordinary differential equation

$$\frac{\partial^2}{\partial z^2}\hat{T}(k_x, k_y, z) = \left(\frac{i\omega}{D} + k_x^2 + k_y^2\right)\hat{T}(k_x, k_y, z) = \tilde{k}^2\,\hat{T}(k_x, k_y, z), \tag{5.5}$$

with the definition of the complex wavenumber $\tilde{k}$. The general solution of equation (5.5) is given by

$$\hat{T}(k_x, k_y, z) = A(k_x, k_y)\cosh(\tilde{k}z) + B(k_x, k_y)\sinh(\tilde{k}z), \tag{5.6}$$

where the coefficients A and B must be chosen in a way that the boundary conditions are fulfilled for each pair of wavenumbers (k_x, k_y).

[6] The PSF is the thermal wave response to a point-like heat source.

The heat source lies on the surface of the regarded solid, i.e. $z = 0$ (see Figure 5.1). It causes a spatially extended heat flux $p_0(x, y)$ which equals the dissipated power density p (per unit area). In the spatial frequency domain the Fourier transform $\hat{p}_0(x, y)$ and the boundary condition reads

$$\hat{p}_0(k_x, k_y) = -\lambda \frac{\partial}{\partial z} \hat{T}(k_x, k_y, z = 0) = -\lambda \tilde{k} B(k_x, k_y). \tag{5.7}$$

Note that in equation (5.7) no thermal losses (cooling) at the interface between the layer and the ambient are considered. At $z = d$, the thickness of the layer, the same assumption leads to

$$\hat{p}_{q,z}(k_x, k_y, z = d) = -\lambda \tilde{k} \left[A(k_x, k_y) \sinh(\tilde{k} d) + B(k_x, k_y) \cosh(\tilde{k} d) \right] = 0. \tag{5.8}$$

Combining equations (5.7) and (5.8) yields for the Fourier transform of the temperature T at the surface of layer $(z = 0)$

$$\hat{T}(k_x, k_y, 0) = \frac{\coth(\tilde{k} d)}{\lambda \tilde{k}} \, \hat{p}_0(k_x, k_y). \tag{5.9}$$

The term $\coth(\tilde{k}d)/(\lambda\tilde{k})$ in equation (5.9) is the Fourier transform $\hat{u}(k_x, k_y, z)$ of the Green's function $u(x, y, z)$ at $z = 0$, i.e. the PSF in Fourier space. It is the key term for the description of the thermal response found in LIT signals, representing the heat flux from the source p that causes the temperature field ΔT.

The inversion of equation (5.9) allows for the uncoupling (or deconvolution, see chapter 6) of the heat source p from the heat flux, i.e.

$$\hat{p}_0(k_x, k_y, 0) = \hat{u}^{-1}(k_x, k_y, 0) \, \hat{T}(k_x, k_y, 0) = \lambda \tilde{k} \tanh(\tilde{k} d) \, \hat{T}(k_x, k_y, 0). \tag{5.10}$$

Thus, equation (5.10) can be used to deduce the Fourier transform $\hat{p}_0(k_x, k_y, 0)$ of the heat source from the Fourier transform $\hat{T}(k_x, k_y, 0)$ of the detected complex signal $\Delta T(x, y, 0)$ (which corresponds to the complex LIT signal *S*). Concluding, by two Fourier transforms (forth and back) with an intermediate division, the initial source $p = p_0(x, y, 0)$ can be reconstructed under the assumption of a thermal model for the system that leads to the PSF in Fourier space $\hat{u}(k_x, k_y, 0)$.

The phase shift between excitation $p_0(x, y, 0)$ and thermal response $\Delta T(x, y, 0)$ is given by the argument of the PSF in real space $u(x, y, z)$

$$\phi = \arg\big(u(x,y,0)\big). \tag{5.11}$$

Only the understanding of ϕ allows the acquisition of the global phase ϕ_g of LIT measurements as the following chapter shows.

5.2 Analysis of phase information of LIT signals

The understanding of the phase signal is very important for a profound interpretation of the complex LIT signal *S*. Several mechanisms can induce a phase shift between excitation and thermal response and add each other up. They have to be separated, if e.g. conclusions from the frequency response of a sample want to be drawn. Altogether, these phase shift mechanisms lead to the *global phase* ϕ_g that is detected by LIT measurements. The following subchapters discuss the main mechanism inducing a phase shift, an additional (avoidable) phase shift due to transients overlapping the lock-in periods, and the detection of the correct global phase.

5.2.1 Mechanisms causing the global phase of LIT images

As shown in chapter 3.3.3, two phase shift mechanisms can principally be detected with the lock-in process: a phase shift due to a dead time t_{dead} or due to a capacitive signal shape distortion. In terms of thermography, it can be stated that heat diffusion in solids is a very fast process, so the temporal course of *S* is expected to correspond to a signal shape distortion rather than to a dead time.

To validate this assumption, a pulsed stimulus was applied to a cut-out of an *a*-Si solar module showing a shunt (the same sample as used in chapter 6.2). A video of the raw thermography signal of the thermographic camera without lock-in process recorded the thermal answer. Figure 5.2 displays the acquired signals: a) shows the temporal evolution of the raw thermography images for selected points in time. The ascent and descent of the signal do not show an immediate response as expected by a rectangular signal shape. Neither a dead time is visible. b) illustrates the temporal course of the signal in two regions, one in the shunt center (red curve), and one far away from the shunt (green curve). The latter region is a constant background signal. The applied stimulus is illustrated by the blue curve.

The applied pulse had a length of t_{pulse} = 62.5 ms. The frame rate f_r of the camera was 160 Hz, that means every $t_r = 1/f_r$ = 6.25 ms an image was recorded. This delivered 10 images for the first half period and overall n = 20 images for the whole period. If the pulsed stimulus had been repeated periodically, this would have led to a lock-in frequency $f_{lock\text{-}in} = f_s/n$ = 8 Hz. The signal in the shunt center increases with limited growth while the pulse is applied.

a)

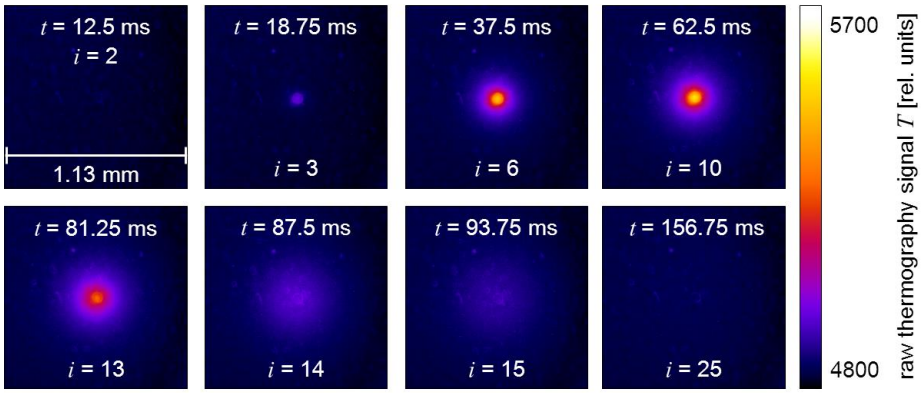

b)

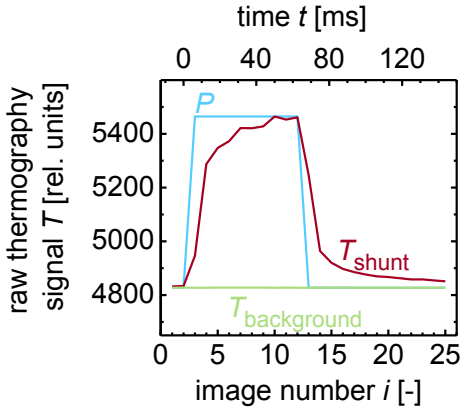

Figure 5.2: Temporal evolution of the thermographic response of a shunt. A pulse with the duration t_{pulse} = 62.5 ms *was applied to the shunt of the a-Si solar module from chapter 6.2.The infrared camera recorded a video at a frame rate* f_r = 160 Hz*, resulting in a time interval of* t_r = 6.25 ms*. a) Selected raw thermography images at certain points in time marked with their running image number i. b) Progress of the raw thermographic signal in the shunt center and in background.*

When the excitation is stopped, the signal decays exponentially. Thus, no dead time t_{dead} is detected, leading to the conclusion that the phase shift is principally caused by a capacitive signal distortion. The primary assumption and expectation was therefore correct. Hence, for a correct quantification of LIT signals, the lock-in process needs to detect capacitive signals reliably. As discussed in chapter 3.3.3, the lock-in technique is only reliable if the number of frames per period n is set sufficiently high, i.e. $n > 20$, leading to a sufficiently high sampling.

5.2.2 Additional phase shift due to transients over many lock-in periods

The considerations made so far on the creation of a phase shift between excitation and thermal response regarded only single lock-in periods. Yet, lock-in measurements are acquired over many periods *N*. When an overlap of slow transient changes is present, an additional phase shift occurs. Such a slow transient is the heating phase of a sample. Breitenstein showed [6, p. 104] that the heating phase of a lock-in measurement leads to an additional phase shift if the measurement is started with the first stimulus. He shows two ways to compensate such an additional phase drift:

- experimentally by applying the stimulus and only starting the measurement when no transient condition overlaps the periodically pulsed signal, i.e. the sample is in a steady state;
- mathematically by calculating the temperature drift.

I used the first suggestion whenever possible; introducing a delay time between first stimulus and the beginning of the acquisition. This procedure ensures the correct use of the lock-in principle and yields reliable results.

Please note that the heating time of a sample is strongly dependent on the setup, i.e. whether the sample is thermally connected to a temperature controlled chuck. A temperature control is generally preferable as measurements can be performed at a standard temperature, allowing for better comparison between measurements. Due to the structure of *a*-Si solar modules, I chose not to use a chuck and preferred to measure from the side of deposition. A temperature control only makes sense if contacted to the deposition side, because heat conduction through the glass superstrate is slow. As no temperature control was used, for each measurement the overall sample temperature was recorded. This record helped in the analysis of differences induced by differing sample temperatures.

5.3 Theoretical frequency response of thin film solar cells and modules

Additionally to the evaluated mechanisms that introduce a phase shift to the complex LIT signal *S* (see chapter 5.2), devices in the LIT setup can cause a further phase shift. Such a device can be e.g. the electrical power supply if it does not response quickly enough to the excitation from the thermographic camera or a chopper wheel of an illumination source. Both examples cause a dead time t_{dead} inducing a further phase shift. Thus, the phase ϕ_{m} of a measured LIT signal *S* can lie anywhere between 0° and 360°. The deviation of the measured phase ϕ_{m} to the theoretical expectation ϕ_{th} is the *global phase*

$$\phi_{\mathrm{g}} = \phi_{\mathrm{m}} - \phi_{\mathrm{th}}. \tag{5.12}$$

The theoretical expectation of the phase ϕ_{th} depends on the type of the stimulating heat source and on the geometrical dimensions of the investigated sample.

The simplest geometry for a heat source is a point heat source. All other geometries can be calculated by the superposition of multiple point heat sources. Thus, the theoretical expectation of the phase ϕ_{th} can be calculated with a simulation of an LIT image using the thermal model presented in chapter 5.1. The geometrical boundaries in this case are the dimensions of the sample in *x* and *y* direction, the sample thickness *d* and the area of one simulated image pixel A_{p}.

As thermal parameter, the diffusivity *D* or the thermal diffusion length Λ given in equation (5.1) can be used. Since Λ depends on the excitation frequency *f*, which is variable in LIT measurements, it is reasonable to examine the frequency response of the thermal model to review criteria for the determination of ϕ_{g}. The dependence of Λ on *f* is proportional to $1/\sqrt{f}$, i.e. Λ decreases with increasing *f*.

The theoretical expectation of the phase ϕ_{th} is derived from equation (5.11). The solution of the PSF in real space can be given analytically only for infinite dimensions of the model in *x* and *y* direction and only in two limiting cases. These solutions are equations (18) and (19) in [101]. The limiting cases depend on the ratio of the model thickness *d* to Λ. For $d \ll \Lambda$, the limiting case is called "thermally thin", resulting in a phase of $\phi_{\mathrm{th}}^{\mathrm{thin}} = -90°$. For $d \gg \Lambda$, the limiting case is referred to as "thermally thick", resulting in a phase of $\phi_{\mathrm{th}}^{\mathrm{thick}} = -45°$ [6, pp. 103, 136]. In between these limiting cases there is a phase transition; and it is important for the understanding of LIT measurements whether this phase transition lies in the range of measurable frequencies.

To determine the global phase ϕ_{g}, criteria have to be found for the derivation of a single value for ϕ_{m} from the LIT signal *S*. As shown in chapter 3.5, ϕ is an image and thus dependent on the position (*x, y*): $\phi = \phi(x, y)$. The first idea for the derivation of a value for ϕ_{m} would be the arithmetic mean of $\phi(x, y)$. Yet, this mean value would not be reliable since $\phi(x, y)$ is generated in a non-linear operation as shown in equation (3.24). Hence, an integral operation is necessary to find an integral phase signal ϕ_{int}. This operation is the replacement of $S^{0°}$ and $S^{-90°}$ in equation (3.24) by their respective integrals over the whole image dimensions (*x, y*), finding the term for the measured phase

$$\phi_{\mathrm{m}} = \phi_{\mathrm{int}} = \arg\left(\iint S(x, y)\, dx\, dy\right). \tag{5.13}$$

An elegant way for a quick access to ϕ_m when calculating in Fourier space is using the first component of the Fourier transform $\hat{T}(k_x, k_y, 0)$, namely $\hat{T}(1,1,0) = \phi_\mathrm{m}$ (see equation (5.3)). This integral definition of a single phase value leads to the first possible criterion for the derivation of ϕ_g: At the limiting cases thermally thin (theoretical phase $\phi_\mathrm{th}^\mathrm{thin} = -90°$) and thermally thick (theoretical phase $\phi_\mathrm{th}^\mathrm{thick} = -45°$), ϕ_g is found to be

$$\phi_\mathrm{g}^\mathrm{thin} = \phi_\mathrm{m}^\mathrm{thin} - \phi_\mathrm{th}^\mathrm{thin} = \phi_\mathrm{m}^\mathrm{thin} + 90° \tag{5.14}$$

and

$$\phi_\mathrm{g}^\mathrm{thick} = \phi_\mathrm{m}^\mathrm{thick} - \phi_\mathrm{th}^\mathrm{thick} = \phi_\mathrm{m}^\mathrm{thick} + 45°, \tag{5.15}$$

respectively, with $\phi_\mathrm{m}^\mathrm{thin}$ and $\phi_\mathrm{m}^\mathrm{thick}$ being the measured integral phase values in the two limiting cases.

Breitenstein showed that the integral definition of ϕ_m from equation (5.13) is only valid if an (image) area larger than $3\Lambda \times 3\Lambda$ is evaluated [6, p. 135]. Thus, an additional second criterion apart from the integral phase could potentially be helpful for accessing ϕ_g. This second criterion shall be the phase position of the maximum signal of a point heat source center $\phi_\mathrm{max}^\mathrm{center}$. The phase of a point heat source center $\phi_\mathrm{max}^\mathrm{center}$ lies at 0° by definition, finding

$$\phi_\mathrm{g} = \phi_\mathrm{m}^\mathrm{center} - \phi_\mathrm{max}^\mathrm{center} = \phi_\mathrm{m}^\mathrm{center} - 0° = \phi_\mathrm{m}^\mathrm{center}, \tag{5.16}$$

where $\phi_\mathrm{m}^\mathrm{center}$ is the measured phase at the point heat source center. With the simulation of the frequency response of the thermal model from chapter 5.1, the applicability and congruence of both criteria can be verified.

For the thermal simulation of the PSF I used the parameters given by the optical resolution of the thermographic camera, which where a sample area of $x = y = 2.44$ mm² (corresponding to the number of 512 × 512 image pixels) and the area of one image pixel $A_\mathrm{p} = (4.77)^2$ µm² = 22.71 µm². As sample thickness, I used $d = 1.1$ mm, which is the thickness of the IEK-5 solar mini modules shown exemplarily in chapter 2.1. The point heat source was modeled with an image having the pixel value of 0 for every pixel except for the middle pixel that represents the heat source with a dimensionless value of 1. The thermal diffusivity D was assumed to be 1 mm²/s; the value was derived from a fit to measurements, which are shown in chapter 6.2. Since the simulation does not contain any additional phase shift, $\phi_\mathrm{g}^\mathrm{sim} = 0°$ and thus $\phi_\mathrm{m}^\mathrm{center} = \phi_\mathrm{max}^\mathrm{center}$ and $\phi_\mathrm{m} = \phi_\mathrm{th}$ hold. The frequency response of $\phi_\mathrm{max}^\mathrm{center}$ and ϕ_th is depicted in Figure 5.3.

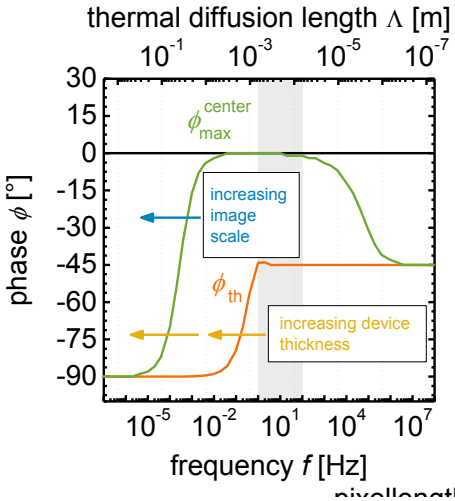

Figure 5.3: Simulated frequency response of the integral image phase and of the heat source center phase. The grey colored area marks the frequency range from 1 *to* 100 Hz *where reasonable LIT measurements can be carried out. The integral image phase signal* ϕ_{th} *verifies that the thermal model is in the limiting case "thermally thick" in the measurable frequency range, since it lies at* -45°. *For lower frequencies, a transition to the limiting case "thermally thin" occurs, shifting* ϕ_{th} *to* -90°. *The heat source center phase* ϕ_{max}^{center} *lies at* 0° *in the measurable frequency range and shifts towards the integral phase at low and high frequencies.*

The transition of the theoretical integral image phase ϕ_{th} between the limiting cases thermally thin and thick is in the frequency range of 0.01 to 1 Hz, i.e. $\Lambda \geq d$. This range can principally be measured by LIT, but transients over such long lock-in periods (1 to 100 s) can hamper the reliable signal detection and are thus not recommended.

For lower frequencies, $\Lambda >> d$ and ϕ_{th} lies at -90° as expected. The transition of $\phi_{\mathrm{max}}^{\mathrm{center}}$ towards -90° with decreasing frequency can be explained by the small simulated area $x \times y$. The simulation has the boundary conditions of total reflection; that means at a low frequency and thus a long thermal diffusion length Λ, the heat source damping is very low. Hence, the source degenerates into an extended heat source. In simulations with increasing image scales, the transition of $\phi_{\mathrm{max}}^{\mathrm{center}}$ shifts to lower frequencies while the transition of ϕ_{th} stays at the same frequency range. For thicker devices with $d > 1.1$ mm, both transitions of $\phi_{\mathrm{max}}^{\mathrm{center}}$ and ϕ_{th} are shifted towards lower frequencies. This proves that d is responsible for the transition of ϕ_{th}. Regarding industrial thin film solar modules, which are thicker than laboratory mini-modules, it can be stated that the frequency range where the thermal thick approximation is valid, is enhanced to lower frequencies for them.

At high frequencies ($\Lambda << d$), a transition of $\phi_{\max}^{\text{center}}$ towards -45° occurs. This can be explained by the fact, that the thermal diffusion length Λ becomes small against the dimension of one image pixel. Thus, the point heat source is seen as an extended heat source, which phase lies at -45°.

The limiting case of thermal thickness is reached in the frequency range of 1 to 100 Hz, where $\Lambda \leq d$ and where LIT measurements are performed. Both phase criteria ϕ_{th} and $\phi_{\max}^{\text{center}}$ stay constant at -45° and 0°, respectively. Thus, both criteria show a good congruence and are a valuable measure for accessing the global phase ϕ_{g}. Chapter 6.3 shows experimental results and the application of these criteria to the measurement of a point heat source.

6 Deconvolution of power generation from heat diffusion with a self-calibrating LIT system

This chapter describes a method called deconvolution that dissociates heat generating sources and thermal blurring due to heat diffusion. This can either be done with the calculation of the heat diffusion differential equation using a thermal model or with a measurement of the heat diffusion. The latter case enables the development of a self-calibrating LIT system that automatically corrects the thermal blurring, without the need to develop a thermal model. The thermal model used for the deconvolution is verified and limits of the deconvolution method are discussed.

6.1 The deconvolution method

LIT is an active measurement method based on a modulation, which is an electrical or optical stimulus in the case of the measurement of solar cells. The response of the sample to the stimulus is heat dissipation at small local and at extended area heat sources. This dissipated heat spreads quickly due to the very fast heat diffusion mechanism in solid bodies. The sources of heat dissipation are often quite small compared to the dimensions of the diffused thermal answer. This impedes the detection of small heat sources, especially in the case of several sources lying close to each other. To detect the size and intensity of the sources of power dissipation, this chapter discusses the possibility to uncouple the source of power dissipation from the heat diffusion. This uncoupling process is based on the calculation or measurement of the heat diffusion and is called deconvolution [6, p. 137]. Figure 6.1 illustrates a scheme of the deconvolution process.

The heat diffusion sets the limit for the spatial resolution of LIT measurements. Mathematically considered, power dissipation of heat sources and heat diffusion are convoluted in real space. In Fourier space, the two mechanisms can be separated by dividing the measured LIT image by the calculated or measured image of the point spread function (PSF, see chapter 5.1). This results in a power dissipation image in Fourier space. Inverse Fourier transforming this image yields the power dissipation image in real space. The original size of all heat sources in the LIT image are reconstructed in this deconvoluted real power dissipation image.

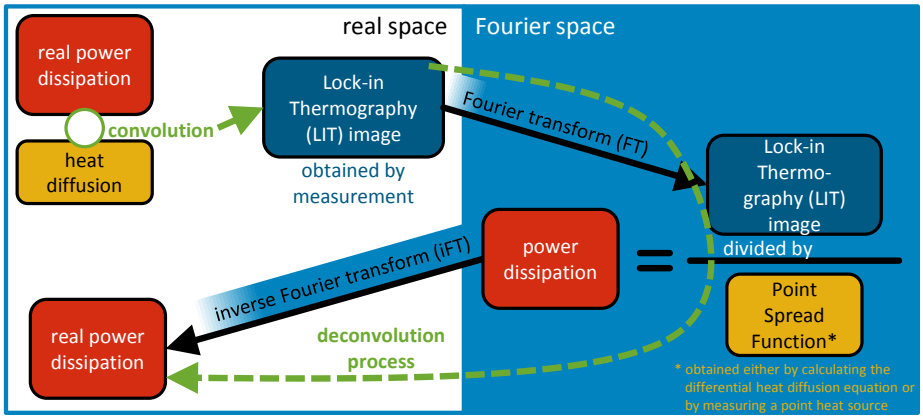

Figure 6.1: Scheme of the deconvolution process. Inherent to LIT images is the heat diffusion from the heat generating sources. Mathematically, both mechanisms are convoluted in real space. In Fourier space, they can be deconvoluted by a division: The Fourier transformed LIT image is divided by the point spread function (PSF) image, which is gained by a calculation of the heat diffusion differential equation or by a measurement of the heat diffusion profile of a point heat source. The resulting image of the division finds the real power dissipation image after an inverse Fourier transform step.

6.2 Deconvoluting the LIT signal of practical devices

To perform a well-defined model experiment, an artificially introduced shunt was shot into an *a*-Si cell during the manufacturing process by a high energy laser that locally ablated the silicon layers. This resulted in a direct contact between the front and the back electrode. This short-circuit was a circular shunt with a diameter of about 65 µm as can be seen from the thermography image in live (non lock-in) mode without (Figure 6.2a) and with applied bias (Figure 6.2b).

Figure 6.2c and d display the real part S^{0° of the measured LIT signal S, obtained with a periodically applied bias current density $J = 12.5$ mAcm^{-2} and a lock-in frequency of $f_{\text{lock-in}} = 3$ Hz and 10 Hz, respectively. Clearly, the higher frequency leads to a better resolution of the thermal LIT image because the thermal diffusion length Λ is reduced by a factor of ~1.8. Still, the dimensions of the shunt cannot be derived from the LIT image at 10 Hz.

For a further enhancement of resolution, the LIT signals can be deconvoluted as explained above, using the calculation of the heat diffusion differential equation (5.2) for the defined thermal model. As a first step, the thermal diffusivity D and the thickness d of the *a*-Si cell had to be obtained. The thickness d was measured to be 1.1 mm. The diffusivity D was found by comparing the LIT measurement with the calculation of

the PSF of an ideal heat source (see chapter 5.3) for several values of D. This fitting process achieved the value $D = 1.0$ mm^2/s. The deconvolution process was then carried out in the following steps:

1) Fourier transform of $S_{\text{shunt}} \rightarrow \hat{S}_{\text{shunt}} = \hat{T}$ in equation (5.3).
2) Calculation of the PSF in Fourier space $\hat{u} = \frac{\coth(\tilde{k}d)}{\lambda\tilde{k}}$ (see equation (5.9)).
3) Calculation of the real power dissipation image of the shunt in Fourier space $\hat{p}_0 = \hat{p}_{\text{shunt}} = \frac{\hat{S}_{\text{shunt}}}{\hat{u}}$ (see equation (5.10)).
4) Inverse Fourier transformation of $\hat{p}_{\text{shunt}} \rightarrow p_{\text{shunt}}$ to obtain the real power dissipation image of the shunt p_{shunt} in real space.

Figure 6.2e and f show the real part p^{0° of the deconvoluted power images p_{shunt} of the shunt. A comparison of both figures unveils that the deconvoluted results at both frequencies are very similar as expected, since the size of the power dissipation source is independent of $f_{\text{lock-in}}$.

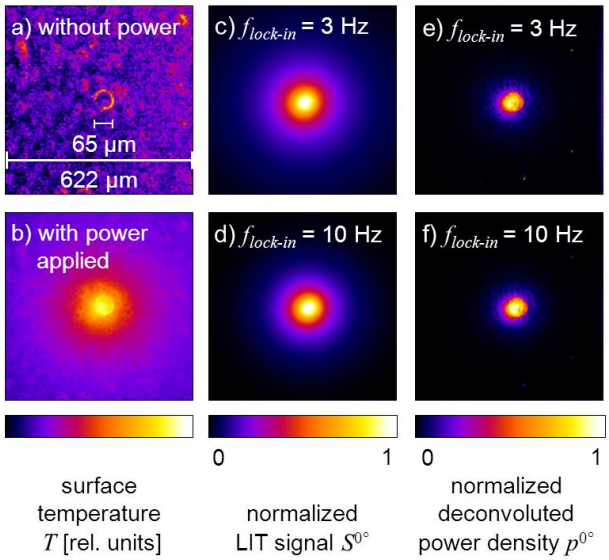

Figure 6.2: Thermography images of an artificial shunt in an a-Si solar module. The live mode – a) without bias and b) with bias $J = 7$ mAcm^{-2} *– representing the detector signal without application of the lock-in technique is used to localize the artificial shunt with an approximate diameter of* 65 µm. *c) and d) show the real part* S^{0° *of the LIT signal (bias* $J = 12.5$ mAcm^{-2}*) measured at lock-in frequencies* $f_{\text{lock-in}} = 3$ Hz *and* 10 Hz, *respectively. e) and f) show the real part* p^{0° *of the power density obtained from the deconvolution process using a layer thickness* $d = 1.1$ mm *and a thermal diffusivity* $D = 1.0$ mm²/s.

This finding is more clearly seen from Figure 6.3, which shows linescans ($y = 0$ in the center of the shunt, $x \geq 0$) for the original signals $S^{0°}$ and $S^{90°}$ corresponding to the LIT images in Figure 6.2c and d, as well as for the real part $p^{0°}$ and the imaginary part $p^{90°}$ of the deconvoluted power density. Although the original thermal signals $S^{0°}$ and $S^{90°}$ differ slightly for the two frequencies, the reconstruction yields equal results for $p^{0°}$ in both cases. Furthermore, the imaginary parts $p^{90°}$ of the deconvoluted signals are close to zero (within the limits given by the noise), indicating that the deconvolution has successfully reconstructed the original source term p, which must be real by definition.

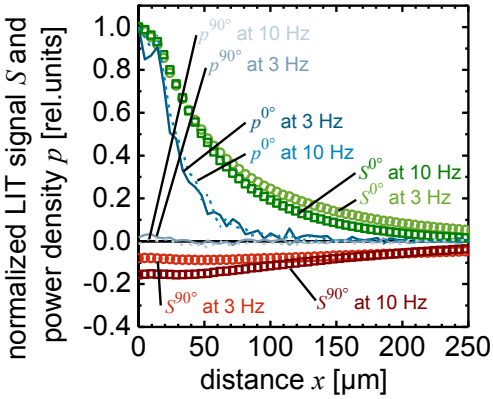

Figure 6.3: Linescans of the LIT signal (real part $S^{0°}$ and imaginary part $S^{90°}$) through the center of the shunt measured at lock-in frequencies $f_{\text{lock-in}}$ = 3 Hz and 10 Hz, respectively, together with the deconvoluted power density signals $p^{0°}$ and $p^{90°}$. The real parts $p^{0°}$ of the deconvoluted signals are very similar for both frequencies. The imaginary parts $p^{90°}$ are zero in both cases (neglecting the noise).

To learn how sensitive the deconvolution process is, the measurement frequency $f_{\text{lock-in}}$ and the assumed diffusivity D was investigated. As a measure for the application of the deconvolution, the full width at half maximum (*FWHM*) was chosen. Figure 6.4 shows the *FWHM* of the measured $S^{0°}$ signal in comparison to the *FWHM* of the deconvoluted signals $p^{0°}$. Whereas the *FWHM* of $S^{0°}$ decreases with increasing frequency as expected, the *FWHM* values of $p^{0°}$ remain about constant over the whole frequency range supported by the camera. With values of about 62 ± 10 µm (linear fit for $p^{0°}$), the *FWHM* is close to the shunt diameter of 65 µm. It has to be mentioned that one pixel width depicts approximately 4.8 µm, i.e. the *FWHM* varies about 2 pixel lengths only.

Furthermore, the choice of the thermal diffusivity D only has an influence at higher frequencies and if chosen lower than about $D = 1.0$ mm^2/s. For lower values, the *FWHM* of the deconvolution increases. For chosen values of D higher than

$D = 1.0$ mm^2/s, the deconvolution always yields similar results. Thus, the deconvolution process is relatively robust against assuming too high values for D, at least for the geometry of the present shunt.

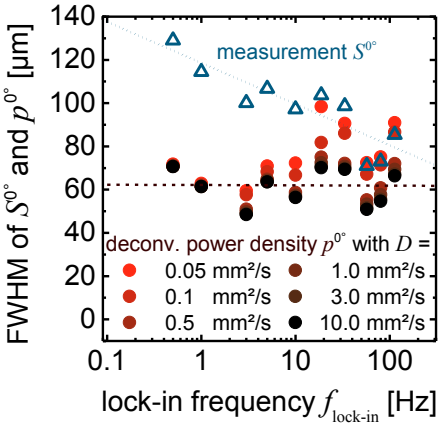

Figure 6.4: Full width at half maximum (FWHM) of the real part $S^{0°}$ of the thermal LIT signal and of the real part $p^{0°}$ of the deconvoluted power density signal, both as a function of the lock-in frequency $f_{lock\text{-}in}$. The FWHM of $S^{0°}$ decreases with increasing $f_{lock\text{-}in}$. The FWHM of the deconvoluted power density $p^{0°}$ is essentially independent of $f_{lock\text{-}in}$. Moreover, if D is chosen above a certain value (here about 1 mm²/s*) the results become independent of the precise choice of D.*

To evaluate the deconvolution process on a practical device, I applied both processes on a defective series interconnection between two cells in an *a*-Si solar module. Figure 6.5a shows $S^{0°}$ and $S^{90°}$ of the LIT signal S obtained at $J = 65$ mA/cm^2 and $f_{lock\text{-}in} = 3$ Hz. The main dissipation occurs at the edges of the laser line P_2 which connects the back contact of the cell at the left with the front transparent conductive oxide (TCO) contact of the cell to the right. As shown in chapter 2.1, the lines P_1 and P_3 must separate the front TCOs and the back contacts between the two cell areas [103].

The power density p derived from the deconvolution process is depicted in Figure 6.5b. As p is the reconstruction of a real power source, its imaginary part $p^{90°}$ should be zero. Within the attainable *SNR*, $p^{90°}$ is negligibly small, proving the successful deconvolution. The real part $p^{0°}$ shows a strong enhancement of the spatial resolution of the heat sources compared to the LIT signal $S^{0°}$ in Figure 6.5a. It finds that the main dissipation occurs at the edges of the P_2 line. This is due to the fact that when choosing non-optimal parameters for this laser scribing process, the line becomes almost insulating due to redeposition of Si material [104]. As can be seen from Figure 6.5b, the current concentrates at few spots at the edges of the line. Thus, the main signal

in this case does not stem from shunts but from current crowding. After deconvolution the edges of the laser lines P_1 and P_3 are also clearly seen. This effect is essentially due to geometric and/or material effects on the emissivity at the edges of the lines. Imperfections in the deconvolution process may play a role. The process cannot distinguish between emissivity effects at features and a heat diffusion of near-by sources that overlap. This effect can be seen in Figure 6.5b at the left edge of the P_3 line, which appears brighter than the right one.

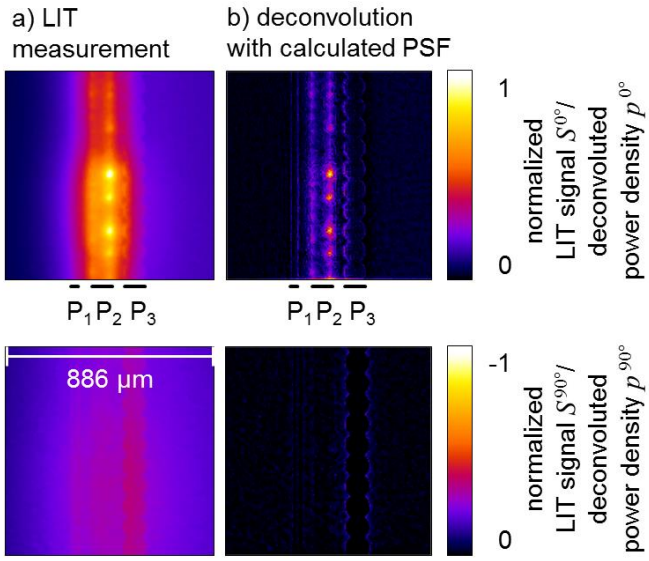

Figure 6.5: Comparison of deconvolution results of a defective integrated series connection in a tandem solar module. The LIT signal S (a) acquired at $J = 65$ mA/cm^2 *and* $f_{\text{lock-in}} = 3$ Hz *is deconvoluted to reconstruct the original dissipated power density p (b). The deconvoluted power density p finds the main dissipation at the edges of the* P_2 *line, which is supposed to connect the back contact of the cell at the left with the front TCO contact of the cell to the right.*

6.3 Realization of a self-calibrating LIT system

Instead of calculating the PSF, it can be measured with the heat diffusion profile of a point heat source. Adding such a measurement possibility to the LIT setup, allows for the LIT system to automatically deconvolute the LIT results. It does not play a role, which thickness and which thermal diffusivity a used sample has and whether the operator of the system knows these data. Such a type of LIT system would be particularly user-friendly as it could calculate the actual electrical power dissipation by just two measurements; one of the PSF, and one LIT measurement of the device. In the following, I will call such a system “self-calibrating”.

6.3.1 Setup

The development of a self-calibrating LIT setup inherits some obstacles that can be solved by certain tricks. The first aim is to find a heat source that is smaller than the optical dimensions of one pixel of the thermographic camera. Furthermore, the thermal diffusion length Λ has to be in a range that is visible in the LIT images. For example, for $D = 1.0$ mm²/s and $f_{\text{lock-in}} = 10$ Hz as above, the thermal diffusion length is about $\Lambda \approx 178$ µm. If the optical dimension of a LIT image pixel width is larger than Λ, no practical information on the actual size of heat sources can be found. In the LIT setup, I used a close-up lens with a magnification factor of $m = 5$ for the thermographic camera. With that, the optical dimension of one image pixel was about 4.8 × 4.8 µm². The heat diffusion according to Λ could therefore be seen well. To obtain a heat source smaller than these 4.8 × 4.8 µm², I used a laser spot that is focused through a microscope lens so that its diameter d_{spot} was smaller than 3 µm. A scheme of the setup is illustrated in Figure 6.6. For the correct measurement of the laser spot, it was important to find the right focus so that the spot is focused in the plain of the TCO and not in the plain of the glass surface. With such a small spot diameter, even a laser spot of a low power laser yields a very high power density. Therefore, I weakened the laser with a filter (dampening 10^{-3}) and a quartz mirror (reflection efficiency 4 %) from 2 mW to 80 nW. The spot area was about $A_{\text{spot}} = \pi(d_{\text{spot}}/2)^2 = 7.07 \times 10^{-12}$ m², leading to an irradiance E_{laser} of the spot of approximately 11300 W/m², which corresponded to the power density of 11.3 suns. This power density was high enough to find an LIT signal and low enough not to damage the investigated solar module. In order to obtain a complex signal as basis for the determination of the PSF, I chopped the laser spot with a chopper wheel and measured it with a regular LIT setup.

6.3.2 Evaluation of the measured heat diffusion profile

With this setup, I measured a similar solar cell sample as used in chapter 6.2 (having an artificial shunt also) with the laser spotting to an area away from the shunt. The LIT measurement of the chopped laser spot leads to an image of a temperature distribution $\Delta T_{\text{meas}} = S_{\text{meas}}$ that shows the heat diffusion profile of an ideal heat source, which is smaller than one image pixel. If this image is normalized to its maximal value, the corresponding power density image p_{ideal} is known: This image has the same dimensions as the LIT image; all pixel values are 0 except the one in the position of the heat source, which has the dimensionless value of 1. With the Fourier transforms of $S_{\text{meas}} \rightarrow \hat{S}_{\text{meas}}$ and $p_{\text{ideal}} \rightarrow \hat{p}_{\text{ideal}}$, the PSF image is obtained by transforming equation (5.10) to $\hat{u} = \hat{S}_{\text{meas}} / \hat{p}_{\text{ideal}}$. Figure 6.7 shows a comparison of the LIT images $S^{0^\circ} = \text{Re}(S)$ and $S^{90^\circ} = \text{Im}(S)$ of the measured heat diffusion profile at lock-in frequencies $f_{\text{lock-in}}$ of 1, 3, and 10 Hz with the results of the simulation of an ideal point heat source, which are presented in chapter (5.3).

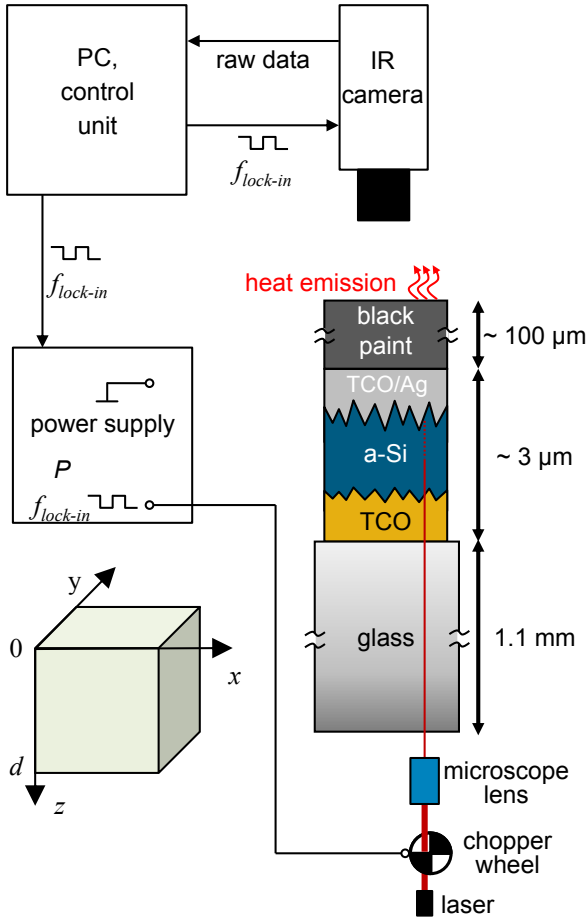

Figure 6.6: LIT setup for the acquisition of the PSF in a sample. The cube shows the orientation of the sample in the setup. The lock-in signal is passed on to a chopper wheel, which is positioned in the light path of the laser beam. The laser beam is focused by a microscope lens to a spot diameter d_{spot} *smaller than* 3 µm*. Thus, the spot is smaller than the resolution of the infrared camera, where an image pixel pictures an area of* 4.8 × 4.8 µm². *The heat diffusion profile of the laser beam on the sample is captured with the infrared camera and processed by a personal computer to obtain the PSF.*

In principle, the measured and the calculated heat diffusion profiles S_{meas} and S_{ideal} show acceptable congruence; yet with some deviations in the absolute signal height and the slope as well as in the imaginary parts S^{90°. For a more incisive comparison, Figure 6.8 shows linescans from the center in x direction to the rims of all images contained in Figure 6.7.

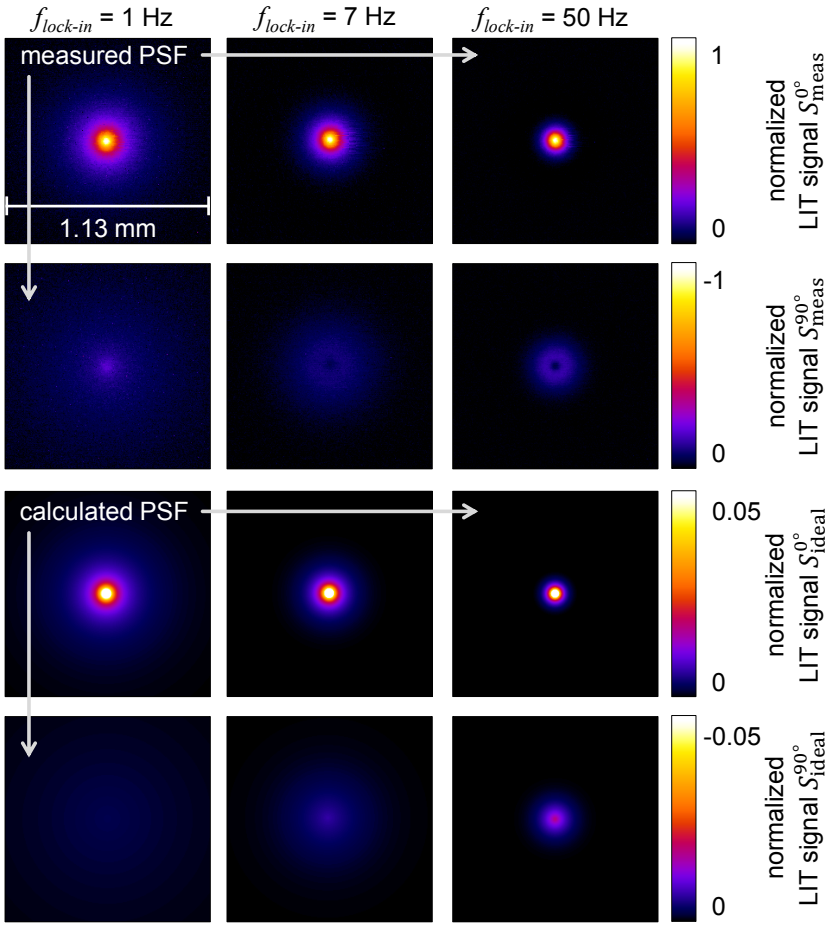

Figure 6.7: Measured heat diffusion profile of a small laser spot on an a-Si solar cell compared to the simulation of an ideal heat source on a thermal model of a thin film solar cell. The measured heat diffusion profiles were acquired with the setup shown in Figure 6.6. Since the heat inducing laser spot is smaller than the dimensions that one image pixel depicts, the measured signal stems from the heat diffusion of this "ideal" point heat source in the center pixel. The comparison to the simulation of an ideal heat source shows deviations in the absolute signal height and the slope as well as in the imaginary parts $S^{90°}$.

The comparison of the linescans of the real parts $S^{0°}$ finds only slight deviations in the slope, pointing to a successful acquisition of the PSF with the measurement of the laser spot. Yet, the discrepancy in the absolute height of the signal is markedly. The discrepancy is presumably caused by the thermal model, since Straube [101] finds lower absolute values for a two-layer model with a thin and highly heat conductive layer on top of a solid body.

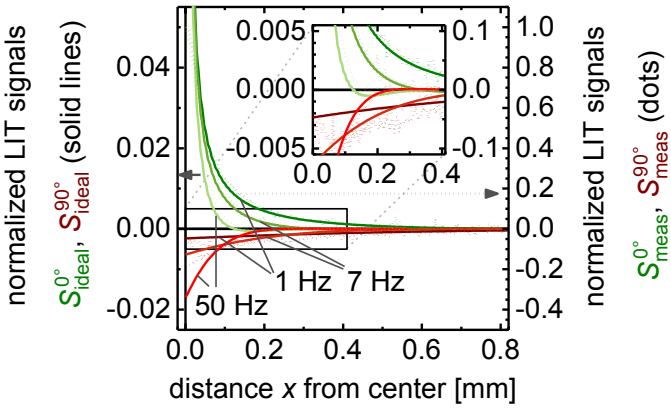

Figure 6.8: Linescans of measured and calculated ideal heat diffusion profiles. The linescans were taken from the center of the images in Figure 6.7 in x direction. The deviations in the slope of the $S^{0°}$ signals are negligibly small. The $S^{90°}$ signal behavior of the measurements at 7 Hz *and* 50 Hz *with the "dip" at r* = 0.1 mm *is due to small phase deviations probably caused by the settling time of the chopper wheel. The markedly higher absolute value of the ideal profile is presumably caused by the simple thermal model [101].*

The deviations in the center of $S^{90°}_{meas}$ are the overestimation at 1 Hz and the occurrence of an undershoot at 7 Hz and 50 Hz. The cause of these deviations is probably the settling process for the synchronization of the chopper wheel that controlled the lock-in process of the laser beam measurement. The setup does not allow leaving out several lock-in periods at the beginning of a measurement as postulated in chapter 5.2.2. Since the settling process for the synchronization of the chopper wheel varied for each measurement frequency, it was not possible to correct the measurements afterwards. I tried to contain the settling process by choosing a long measurement time. Additionally to the chopper wheel synchronization, a further influence on the phase deviations may be caused by a low sampling as explained in chapter 3.3.3. Figure 6.9 illustrates the results for the phase deviations of the two criteria for ϕ^{center}_{max} and ϕ_{int} (see chapter 5.3). The plot was achieved by adjusting the global phase ϕ_g to fulfill the limiting case of "thermal thickness", resulting in ϕ_{int} = -45° for all frequencies. This limiting case was predicted by the simulations in chapter 5.3.

The phase of the heat source center maximum ϕ^{center}_{max} fluctuates only slightly except for some outliers at 1, 20, 30 and 100 Hz. As explained, they are probably due to the chopper wheel synchronization time and the low sampling at higher frequencies. At 1 Hz, the thermal thick approximation additionally starts to become precarious, since Λ = 0.56 mm is in the range of d = 1.1 mm. The linear fit to ϕ^{center}_{max} over all measurements shows a slight increasing trend. But when leaving out the precarious measure-

ments at 1 Hz and 100 Hz (low sampling, $n = 4$), the linear fit lies well at 0° with a slight negative slope only.

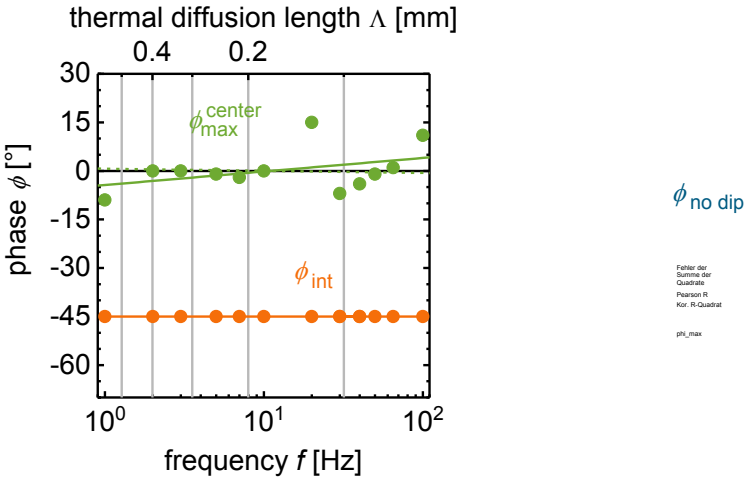

Figure 6.9: Measured frequency response of the integral image phase and of the heat source center phase. The global phase ϕ_g was adjusted with the criteria of ϕ_{int} = -45° to fulfill the limiting case of "thermal thickness" that was predicted in chapter 5.3. The phase of the heat source center maximum ϕ_{max}^{center}, which was predicted to be consistently 0° in theory, fluctuates with maximally 15°. The solid lines represent the respective linear fits to the data. At 1 Hz and 100 Hz uncertainties occur due to the beginning transition of the thermal thick case at 1 Hz (see Figure 5.3) and due to the low sampling at 1 Hz with n = 4. When leaving out these two points, the linear fit of ϕ_{max}^{center} (dashed green line) stays almost constantly at 0°.

Summarizing, the measurement of the heat diffusion profile and the derived PSF seem acceptable, still there is room for improvement. For a reliable self-calibrating system, the chopper wheel synchronization has to be improved in particular to ensure a consistent acquisition of the PSF phase. Furthermore, the application of a two-layer model could deliver a more precise theoretical description. Whether the quality of the measured PSF is acceptable for a self-calibrating device is discussed in the following chapter 6.3.3.

6.3.3 Self-calibration on a sample with an artificial shunt

To evaluate the functioning of the setup and the deconvolution process, I acquired an LIT signal of an artificial shunt in the same sample cell that was used for the measurement of the heat diffusion profile S_{meas}. The LIT signal acquisition was carried out at lock-in frequencies $f_{\text{lock-in}}$ of 1, 3, and 10 Hz and at a current flow over the shunt

of approximately $I_{\mathrm{shunt}} \approx 45$ mA (see Figure 6.10). The deconvolution process was carried out in the following steps:

1) Construction of the power density image p_{ideal} as described in chapter 6.3.2.
2) Fourier transform of the three complex quantities $S_{\mathrm{shunt}} \rightarrow \hat{S}_{\mathrm{shunt}}$ ($= \hat{T}$ in equations (5.10)), $S_{\mathrm{meas}} \rightarrow \hat{S}_{\mathrm{meas}}$, $p_{\mathrm{ideal}} \rightarrow \hat{p}_{\mathrm{ideal}}$.
3) Calculation of the PSF in Fourier space $\hat{u} = \hat{S}_{\mathrm{meas}}/\hat{p}_{\mathrm{ideal}}$.
4) Calculation of the real power dissipation image of the shunt in Fourier space by $\hat{p}_{\mathrm{shunt}} = \hat{S}_{\mathrm{shunt}}/\hat{u}$.
5) Inverse Fourier transformation of $\hat{p}_{\mathrm{shunt}} \rightarrow p_{\mathrm{shunt}}$ to obtain the real power dissipation image p_{shunt} of the shunt in real space.

The deconvolution results using the measured PSF are shown in Figure 6.10 compared to the deconvolution results using the calculated PSF shown in chapter 5.1, using the parameters solar cell thickness $d = 1.1$ mm and thermal diffusivity $D = 1$ mm²/s. Following observations regarding each method separately can be made: First, all deconvoluted shunt signals have the same size independent of the frequency. Second, the signal $p_{\mathrm{m}}^{90^\circ}$ is noise only and $p_{\mathrm{c}}^{90^\circ}$ is very low. Both observations lead to the conclusion that the deconvolution works successfully in principle, as theoretically the heat source is real (not complex) and independent of the acquisition frequency.

Comparing the results of the two deconvolution methods with each other, the method using the calculated PSF shows a significantly higher *SNR*. This is expected since the calculated PSF does not contain any noise. So the deconvoluted result using the calculated PSF just contains the noise of the shunt measurement. The deconvoluted result using the measured PSF contains the noise of the shunt measurement and the heat diffusion profile measurement, explaining its markedly lower *SNR*. As the noise looks like a more or less regular pattern, it seems to contain information from interferences of the laser spot with the glass surface or the TCO layer.

In terms of the shunt size that is reconstructed by both methods, the method using the calculated PSF reconstructs smaller features. It finds the shunt size to be 65 µm compared to 85 µm, which the method using the measured PSF reconstructs. This fact points to the conclusion, that the method using the calculated PSF is more accurate. Yet, as mentioned above, 1 image pixel width corresponds to approximately 4.8 µm; so the size difference is just 4 image pixels. Thus, the shunt size reconstruction lies in the tolerance of the image resolution. However, another feature of the comparison points to the above conclusion, too: The deconvolution with the calculated PSF resolves the heat source more precisely, showing that most of the heat generated in the shunt stems from its edges. In contrary, the method using the measured PSF finds the maximal power dissipation in the center of the shunt.

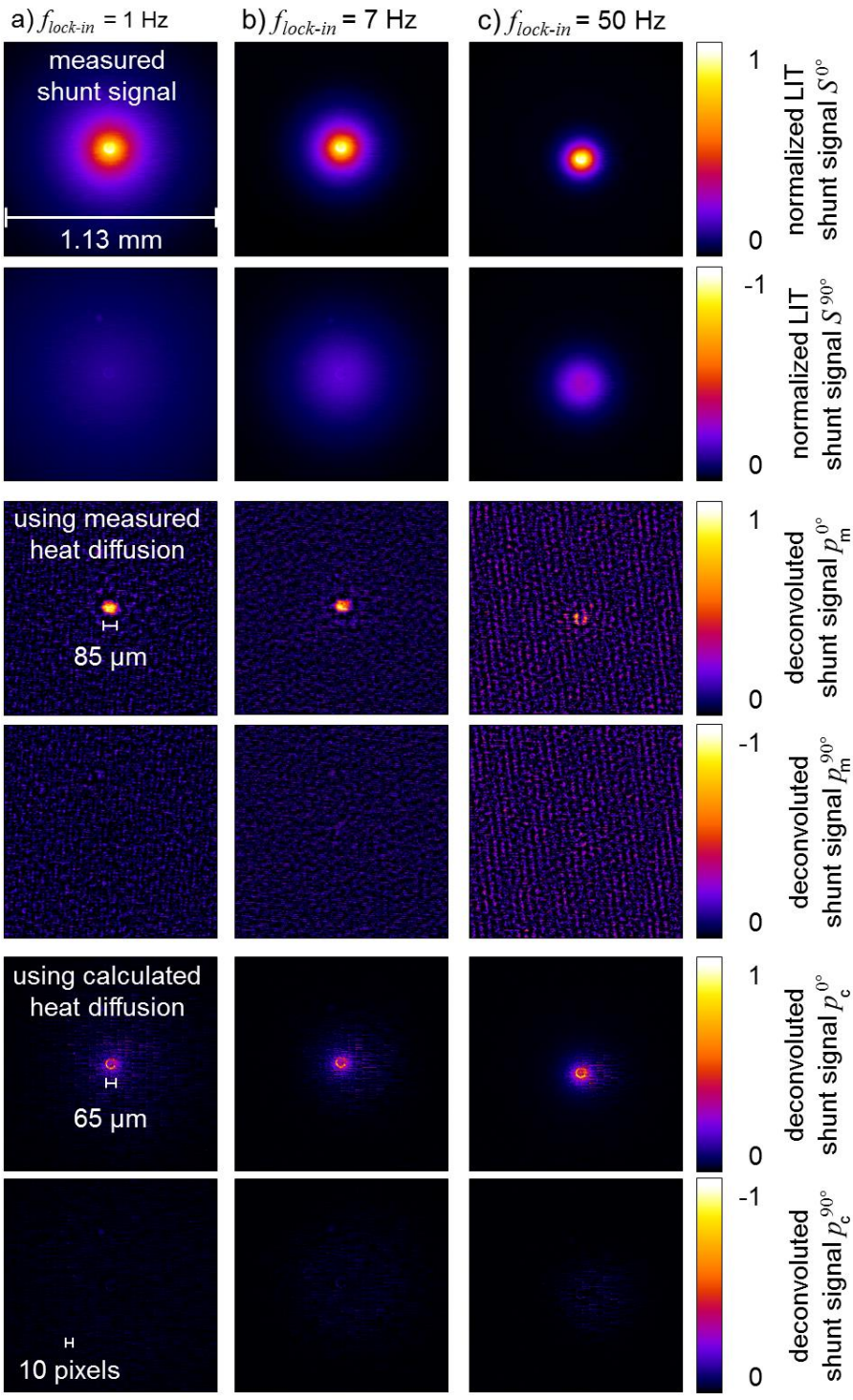
a) $f_{lock\text{-}in}$ = 1 Hz
b) $f_{lock\text{-}in}$ = 7 Hz
c) $f_{lock\text{-}in}$ = 50 Hz
measured shunt signal
1.13 mm
using measured heat diffusion
85 µm
using calculated heat diffusion
65 µm
10 pixels
normalized LIT shunt signal $S^{0°}$
normalized LIT shunt signal $S^{90°}$
deconvoluted shunt signal $p_m^{0°}$
deconvoluted shunt signal $p_m^{90°}$
deconvoluted shunt signal $p_c^{0°}$
deconvoluted shunt signal $p_c^{90°}$
1
0
-1
0

Figure 6.10: Comparison of deconvolution results of a shunt. The measured LIT signal at three lock-in frequencies $f_{\text{lock-in}}$ of 1 Hz *(a),* 3 Hz *(b), and* 10 Hz *(c) is deconvoluted using the measured PSF (Figure 6.7) and the calculated PSF (chapter 5.1). All deconvoluted shunt signals have the same size for each method independent of the frequency. This shows that the deconvolution method in principle successfully reconstructs the shunt's size. As a second proof for the validity of the deconvolution, the signals $p_{\text{m}}^{90^\circ}$ and $p_{\text{c}}^{90^\circ}$ are very low (nearly zero), finding that the original heat source is real as postulated by theory. Comparing the results of the two deconvolution methods, it is found that the method using the calculated PSF resolves the shunt in more detail.*

This leads to the conclusion, that the measured heat diffusion profile has a too large extent. An explanation for this is the focusing of the laser spot, which is presumably hampered by the TCO layer. This layer is optimized for the spreading of incoming light, i.e. the TCO layer may expand the laser beam, leading to a larger heat source than depicted in one image pixel. Anyway, the shunt size reconstruction with the deconvolution using the measured diffusion works acceptably well.

To characterize the self-calibrating LIT system, a measurements series over the whole supported frequency range was acquired. Compared to the measurements series from chapter 6.2, which included lock-in frequencies $f_{\text{lock-in}}$ from 0.1 to 100 Hz, the series for the self-calibrating LIT system was limited from 1 to 100 Hz. This was due to the chopper wheel that did not support frequencies below 1 Hz. Concerning the shunt size in the deconvoluted results, a manual review found them to be 85 ± 10 µm using the method with measured PSF and 65 ± 10 µm using the method with calculated PSF, as can be seen in Figure 6.10.

The deconvolution results using calculated PSF showed that most of the heat generated in the shunt stems from the edge of the shunt. In this case, the *FWHM* as used in chapter 6.2 is not an appropriate measure for the deconvolution results over the frequency range. Instead, the *SNR* is used to compare the deconvolution results of the self-calibrating system with the ones of the method using calculated PSF. In principal it can be stated that the higher the *SNR*, the better the deconvolution result is. The *SNR* was calculated with the definition by Bushbert for imaging techniques [105], being the ratio of the amplitude of the useful signal A_{signal} to the standard deviation σ_{noise},

$$SNR = \frac{A_{\text{signal}}}{\sigma_{\text{noise}}}. \tag{6.1}$$

The standard deviation σ_{noise} is calculated using the estimator function

$$\sigma_{\text{noise}} = \sqrt{\frac{1}{n-1}\sum_{i=1}^{n}(X_i - \bar{X})^2} \tag{6.2}$$

with n being the number of regarded pixels, X_i the value of pixel No. i and the arithmetic mean of all pixel values $\bar{X} = \frac{1}{n}\sum_{i=1}^{n} X_i$. Since the signals are normalized, the used amplitude of the useful signal is $A_{\text{signal}} = 1$. The standard deviation is calculated using all image pixels except the ones of the shunt in the center carrying the useful signal. Figure 6.11 shows the *SNR* of the deconvoluted real power images $p_{\text{m}}^{0^\circ}$ and $p_{\text{c}}^{0^\circ}$ (for both methods – measured and calculated PSF) named SNR_{m} and SNR_{c}.

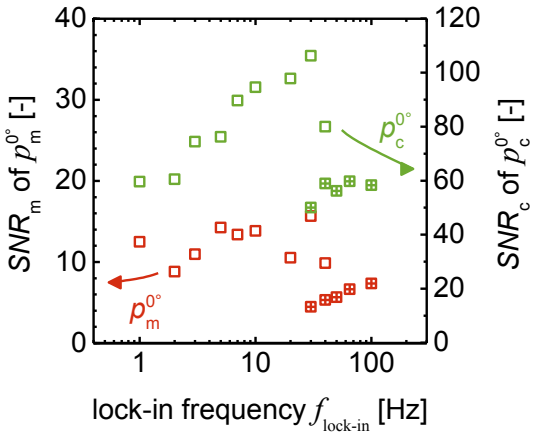

Figure 6.11: Comparison of the signal-to-noise ratios of deconvolution results using measured (SNR_{m}) and calculated PSF (SNR_{c}). Cubes represent measurements at full detector resolution. For higher acquisition frequencies, the detector resolution has to be scaled-down. These measurements are represented by crossed cubes. For both deconvolution techniques, the SNR of the scaled-down images decrease markedly. Over the whole frequency range, SNR_{c} is higher than SNR_{m} with a factor of about 8 to 10. When only considering full frame images, the SNR tends to rise with increasing frequency. Best deconvolution results were obtained at $f_{\text{lock-in}}$ = 30 Hz for both processes.

As explained above, SNR_{c} is higher than SNR_{m} over the whole frequency range. Quantitatively, the factor $SNR_{\text{c}}/SNR_{\text{m}}$ is about 8 to 10. At higher lock-in frequencies above 30 Hz (crossed cubes in Figure 6.11), both signal-to-noise ratios drop markedly. To achieve these high frequencies, a subframe of the infrared detector had to be chosen (256 × 256 pixel, see chapter 3.4.1). Obviously, this enhanced the noise in the images at high frequencies. For a comparison, images at full frame resolution (cubes) were acquired at $f_{\text{lock-in}}$ = 30 Hz and at $f_{\text{lock-in}}$ = 40 Hz, which showed a higher *SNR* compared to

the low resolution images at the same frequencies. Neglecting the deconvoluted low resolution images, the *SNR* tendentially increased with increasing frequency. The best *SNR* for both deconvolution methods was achieved at 30 Hz in full frame resolution. It has to be noticed that all shunt LIT images at full frame resolution had the same acquisition time of $t_{acq} = 10$ min; the acquisition time of the heat diffusion profiles was $t_{acq} = 20$ min. Concluding, a high lock-in frequency and a full frame resolution enable the best deconvolution results.

In summary it can be stated that the deconvolution process for LIT images is a useful tool for the evaluation of small heat sources in solar cells and modules. It can be applied to any structures with a size as large as about the thermal diffusion length. It is helpful for the analysis of defects as well as new processes, e.g. new series connection concepts for thin film solar modules. There are two ways to implement the deconvolution process: First, to establish a thermal model for the sample and then to calculate the PSF of the thermal model. Second, to measure the heat diffusion profile of a point heat source smaller than the dimensions that a pixel of the thermographic camera depicts. In many cases, a focused laser beam can deliver such a heat source. In both cases, the implementation of an algorithm using Fourier transform is necessary. The first implementation with calculated PSF shows very satisfying deconvolution results with a high *SNR*. It was found to be quite insensitive to the estimation of a high thermal diffusivity *D*, i.e. its algorithm is relatively robust. Yet, the implementation is quite complex with the introduction of a thermal model including a fitting process for the parameters needed.

The second implementation using a measurement of the PSF enables a self-calibrating system for each sample without the need to know its thermal properties, dimensions, etc. This principally could fasten the deconvolution process compared to the first implementation. The setup I used produced acceptable results for the estimation of the size of a shunt.

7 Quantitative interpretation of Limo-LIT signals and images

This chapter explains known and novel voltage-modulated LIT methods under constant illumination that allow for a reasonable quantification of power dissipation and generation in solar modules. Contrarily to previously proposed LIT methods, the novel methods are carried out at the MPP, i.e. under operation conditions.

7.1 Power density scaling of Limo-LIT signals

The evaluation of solar cells and modules by means of LIT can obtain insight into power dissipation sites and mechanisms. This evaluation has to be realized at realistic operation conditions, i.e. under illumination. Hence, the correct quantification of Limo-LIT signals plays a major role in this evaluation.

Primarily to the quantitative evaluation, Limo-LIT measurements have to be carried out. Compared to Vomo-LIT measurements, the requirements on the setup are more demanding: As described in chapter 4.6, a suitable light source has to be chosen, i.e. with a high irradiance and sufficient irradiance homogeneity. Furthermore, a source measuring unit working in four quadrants (instead of two) has to be used, as the power generated by the solar cell or module has to be absorbed.

In principle, Limo-LIT can be carried out at any bias voltage applied to the solar cell or module. For the implementation of the modulation, there are several possibilities:

- For small bias voltages below V_{oc}, the bias can be held constant and the illumination can be modulated. This approximation is valid as long as the dark current flow J_d at switched off illumination is negligible compared to the current flow J at full illumination.
- A more accurate measurement is achieved, if the bias voltage and the illumination are modulated simultaneously. This requires a fast and reliable triggering of both modulated quantities with the lock-in process.
- The same accuracy at lower requirements for the setup achieves the use of an adjustable resistance (potentiometer) that is connected to the solar cell or module. The resistance can be adjusted to the wanted bias voltage under full illumination. Then just the illumination can be modulated. The Limo-LIT measurements in this thesis were carried out with this method.

An access to the quantitative evaluation of Limo-LIT is the approach introduced by Isenberg [70], which uses the entire *P/V* characteristic of a solar cell. I applied the

approach to the *a*-Si solar mini-module used in chapter 4.6. First, a characterization of the solar module under the LED light source of the Limo-LIT setup and under a sun simulator with normed air mass 1.5 global light (AM1.5G) had to be carried out. This had to be done to find out, whether the module's *J/V* characteristic changes under the different spectrum of the light. In principle, the V_{MPP} could be shifted to another voltage and J_{MPP} could differ as the distance of LED light source and module was chosen to match the respective J_{sc} under both light conditions, i.e. $J_{sc,LED} = J_{sc,AM1.5G}$. If the deviations were too high, this would prevent drawing more general conclusions from Limo-LIT measurements. The matching led to an irradiance $E_{LED} = 634.4$ W/m² of the LED light source. The measured *J/V* (a) and *P/V* (b) characteristics are shown in Figure 7.1.

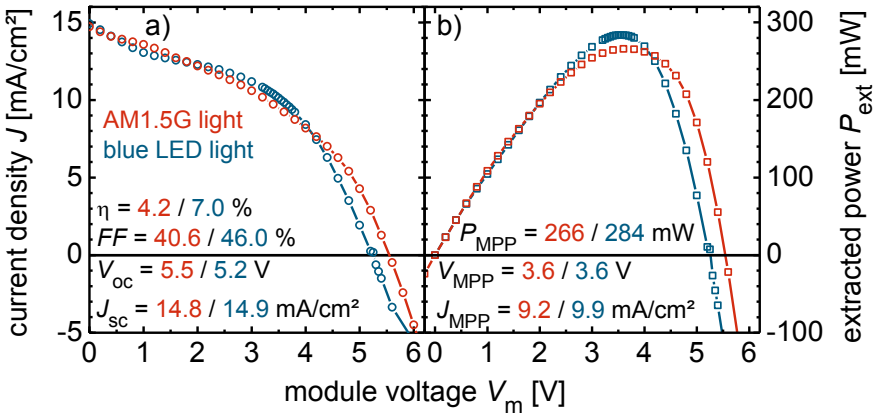

Figure 7.1: Measured J/V and P/V characteristics of the examined a-Si module under AM1.5G and illumination with blue LEDs. Under blue LED light, the module achieves a somewhat higher J_{MPP} and thus a higher P_{MPP}. The FF is higher, which partly is due to the lower V_{oc}. The efficiency η is much higher as the a-Si solar module is especially sensitive to illumination in the short-wave range of the visible spectrum. This shows that integrally over the whole module, the LED illumination source of the LIT setup yields results comparable to those of a sun simulator.

The characteristics under both illuminations almost correspond except for some minor differences. The V_{oc} is lower under the LED light, but the current at MPP I_{MPP} higher. As V_{MPP} is the same for both illuminations, the output power P_{MPP} and the fill factor *FF* are higher, too. The efficiency eta is much higher under the blue light as the *a*-Si solar module is especially sensitive to illumination in the short-wave range of the visible spectrum. In conclusion, the module characteristics do not change much under the different illumination sources. This allows drawing conclusions about the electrical behavior of the module from Limo-LIT measurements to real operation conditions.

Yet it has to be stated that the measurements represent integral values of the complete module. Voltages of single cells in the module still can differ under the different light sources. A monitoring of the cell voltages during the *I/V*-measurements at the sun simulator is necessary, if the Limo-LIT signals want to be investigated in detail. Such an investigation is shown in chapter 7.3. As the approach of Isenberg evaluates the integrally dissipated electrical power, these deviations can be neglected in the following evaluation. According to chapter 2.4 and Breitenstein [6, p. 44], the integral of the $S^{-45°}$ Limo-LIT signal must be proportional to all dissipated heat in the solar cell at a certain operation point. Therefore this integral can be compared to the measured electrically dissipated power of the solar module at its contacts. In that way, a P_d/V-characteristic can be retrieved. Figure 7.2 shows this comparison of the characteristics. The green curve is the measured power at the contacts ($P_{ext} = V \times I = P_{in} - P_d$) and the blue curve is the integrated $S^{-45°}$ Limo-LIT signal.

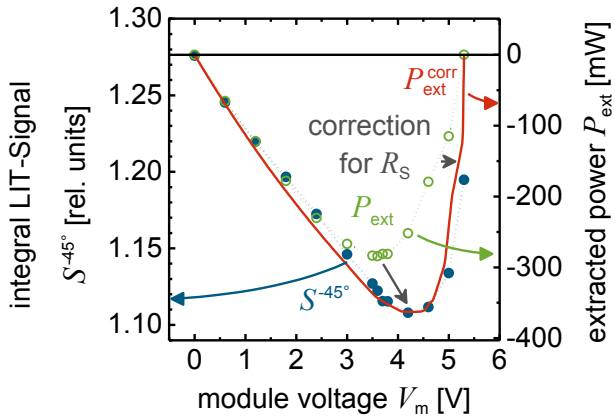

Figure 7.2: Comparison of integral Limo-LIT $S^{-45°}$ signals (blue circles) to the extracted power P_{ext} (green circles) of the examined a-Si module, both over the module's voltage. The MPP according to the integral LIT signals is shifted compared to the MPP of the extracted power by a voltage $\Delta V_{abs} = 0.64$ V. This is due to the contact series resistance R_S^c, which cannot be measured by LIT. With a procedure that corrects for R_S^c, the MPPs of P_{ext} and $S^{-45°}$ can be fitted to match (red line). In the present case, the contact series resistance was found to be $R_S^c = 12\ \Omega$. The comparison of the corrected maximal extracted power P_{ext}^{corr} and the difference level between the integral LIT signals at J_{sc} and MPP can be used to scale the Limo-LIT images. Here, the result is a power density scaling from 0 *to* 1276 W/m² *for Figure 4.13 a-c.*

Two major discrepancies between the two curves can directly be seen: The first discrepancy is that at V_{oc}, the Limo-LIT signal does not reach the same value as at J_{sc}, which a solar cell does in theory. This can be due to the series resistance R_S^c of contacts

and supply cables or it can have to do with additional losses occurring outside the field of view of the LIT images. Due to mechanical restrictions of the sample holder, which only enables a free view on the active solar module area, it was not possible to find such losses with the LIT setup. Still, there is another possible explanation for the deviation of the LIT signal at V_{oc}: If the directly measured temperatures by the camera are compared, it shows that the mean temperature of the whole module rises from 30.0 °C at $V_m = 0$ to 30.5 °C at $V_{oc,m}$. A possible explanation is that the spectrum of the emitted heat of the solar module shifts with increasing voltage. If additionally the quantum efficiency of the thermocamera is not constant over this spectrum range, this can lead to the loss of proportionality between the camera signal and the dissipated power. As the measurements of both the spectrum of the solar module excitation as well as the cameras quantum efficiency is very challenging, this explanation could not be verified experimentally.

The second distinctive discrepancy between P_{ext} and the integral $S^{-45°}$ LIT signals is that the MPP is shifted from $V_{MPP} = 3.60\,\mathrm{V}$ to $V_{MPP}^{corr} = 4.24\,\mathrm{V}$ by a the voltage $\Delta V_{abs} = V_{MPP}^{corr} - V_{MPP} = 0.64\,\mathrm{V}$. This is probably due to the series resistance R_s^c of the contacts and supply cables, which are not in the field of view of the LIT images and thus not inherent to the integral $S^{-45°}$ LIT signals. To verify the assumption that a series resistance causes the shift of the MPP, the measured curve of P_{ext} can be corrected for R_s^c with the following procedure:

- The absolute voltage difference between P_{ext} and the integral $S^{-45°}$ LIT signals normalized to the same minimum of dissipated power has to be calculated. From this curve, a typical value, for example the arithmetic mean or the median or the voltage difference in the MPP has to be chosen. In this case, I chose the latter method, leading to $\Delta V_{abs} = 0.64\,\mathrm{V}$.
- The additional resistance can then be calculated by $R_s^c = \Delta V_{abs}/I$, leading to a value of $R_s^c = 12\,\Omega$ in this example.
- The power curve corrected for R_s^c is then achieved by calculating the voltage difference $\Delta V_{const} = R_s^c \times I$ and shifting $I(V)$ by ΔV_{const}.
- The corrected curve is then found by calculating $P_{ext}^{corr} = V \times I$.

This method causes uncertainties in the range of low voltages, thus an approximation (e.g. linear) for low voltages to fit $P_{ext}^{corr}(V = 0) = 0$ can be applied. However, the low voltage range is not as important as the voltage region around V_{MPP} for the quantitative analysis and may be neglected as well. The corrected extracted power P_{ext}^{corr} is depicted in Figure 7.2 as red curve. It matches the measured integral LIT signals (blue curve) well so that the assumption of additional series resistances explains the shift of the MPP well.

The values of the highest ($S_{Isc}^{-45°} = 1.276 \times 10^6$ rel. units) and lowest ($S_{MPP}^{-45°} = 1.108 \times 10^6$ rel. units) LIT signal can be used indirectly for an estimation of the dissi-

pated power, allowing to apply a power density scale to the Limo-LIT images. The difference of these two signals $\Delta S^{-45°} = S_{Isc}^{-45°} - S_{\mathrm{MPP}}^{-45°}$ is proportional to the extracted power $P_{\mathrm{ext,max}}^{\mathrm{corr}} = 363$ mW. With that, the scale for the dissipated power density in an image pixel $p_{\mathrm{d}}^{\mathrm{x_0,\,y_0}}$ of the Limo-LIT measurement is

$$p_{\mathrm{d}}^{\mathrm{x_0,\,y_0}} = \frac{N_{xy}}{\Delta S^{-45°}} \frac{P_{\mathrm{ext,max}}^{\mathrm{corr}}[\mathrm{W}]}{A_{\mathrm{m}}[\mathrm{m^2}]} S_{\mathrm{x_0,\,y_0}}^{-45°} \tag{7.1}$$

with the module's area A_{m} (in this case, 64 cm²), the Limo-LIT signal $S_{\mathrm{x_0,\,y_0}}^{-45°}$ of a pixel $\mathrm{x_0}$, $\mathrm{y_0}$, and the total number of image pixels N_{xy} (compare chapter 4.2). In the present case, one relative unit of $S_{\mathrm{x_0,\,y_0}}^{-45°}$ conforms to $p_{\mathrm{d}}^{\mathrm{x_0,\,y_0}} = 85.1$ W/m². The dissipated power density is $p_{\mathrm{d}}^{Isc} = 430.8$ W/m² at I_{sc} and $p_{\mathrm{d}}^{\mathrm{MPP}} = 374.1$ W/m² at MPP. This conforms to an absolute dissipated power of $P_{\mathrm{d}}^{Isc} = 2.757$ W and $P_{\mathrm{d}}^{\mathrm{MPP}} = 2.394$ W, respectively. These values lead to a power density scaling for the Limo-LIT images in Figure 4.13 a-c from 0 to 1276 W/m². This seems reasonable as the largest parts of the module have a reddish color that conforms to about 630 W/m². This value is well in the range of the irradiated power $p_{\mathrm{in}} = E_{\mathrm{LED}} = 634.4$ W/m².

This power scaling procedure for the Limo-LIT images is very sensitive to the measurement times used. It relies on absolute integral values, which contain frequency-independent random noise. This noise decreases with increasing measurement time, thus the highest and the lowest Limo-LIT signal (at I_{sc} and MPP) also. But as these signals decrease in the same level, their difference ΔS will stay constant. That means, the noise level drops quickly at the beginning of the measurement. If the measurement is stopped while the integral values still change, huge deviations in the power scaling can occur. Therefore I recommend displaying the integral LIT signal level while measuring and only stopping the measurement when the integral signal level goes into saturation.

If the achieved values for P_{d}^{Isc} and $P_{\mathrm{d}}^{\mathrm{MPP}}$ are compared to the irradiated power – which is in our case $P_{\mathrm{in}} = 634.4$ W/m² × 64 cm² = 4060 mW – it becomes clear that a huge amount of power is "lost". This is most likely due to the reflectivity of the sample, i.e. the measured heat through the camera just allows an "internal" power scale for the device. Also, losses outside the module area could occur due to insufficient edge isolation. The isolation is produced by a laser scribing process and could leak so that currents could flow over areas outside the module that are not in the field of view of the LIT camera.

Concluding it can be said that the application of a power density scaling to Limo-LIT images needs accurate measurements and possibly a correction for series re-

sistances. The reliability of the scaling procedure could be investigated in a statistical analysis of many measured devices.

7.2 Overview of known and new developed LIT methods

Principally, LIT is a very variable investigation tool with many measurement parameters that can be chosen. Especially the parameters of the modulated stimulus (light or voltage) can be set freely in a reasonable range depending on the sample. Yet, up to now only quite distinctive modulation parameters were used in LIT investigations of solar cells and modules. That means, in Vomo-LIT investigations, the voltage was only modulated starting with zero bias. Other starting biases were not considered so far. A modulation from a negative voltage to a positive one of the same value, for example, could yield an LIT image of a solar cell that is corrected for shunts. In case of Limo-LIT, one could think of modulating from zero irradiance to different maximal irradiances, not just to the irradiance of standard test conditions E_{STC}. Also a modulation between two different irradiance levels is imaginable.

Particularly the combination of a bias illumination with a modulated voltage offers manifold possibilities for the evaluation of solar cells and modules. So far, only a method with a modulation between $V = 0$ and $V = V_{MPP}$ (R_s-ILIT) was developed, as introduced in chapter 3.4.2. With opening this method for modulations between any two reasonable bias voltages, many new insights into the operation of solar cells and modules in realistic conditions could be found. I will call this method Vomo-ILIT in the following, and specify the modulation biases if needed. Vomo-ILIT modulations can be categorized into three bias voltage ranges:

- offset from $0 \leq V < V_{MPP}$, modulation to $V = V_{MPP}$
- offset from $V = V_{MPP}$, modulation to $V_{MPP} < V \leq V_{oc}$
- power-neutral modulation around V_{MPP}

These Vomo-ILIT methods are introduced in chapters 7.3 and 7.4. To clarify, which modulation different LIT methods use, Figure 7.3 shows a schematic overview of the most popular LIT methods and the new methods presented in this thesis. Figure 7.4 illustrates the same methods by means of the I/V and p_d/V characteristics of a solar cell or module.

All Vomo-ILIT measurements are principally carried out under a constant illumination and a voltage modulation. Yet, there is another possibility to gain the same results with Limo-LIT measurements, i.e. modulated illumination and constant voltage. In that case, two Limo-LIT images at different voltages have to be acquired and then be subtracted from each other.

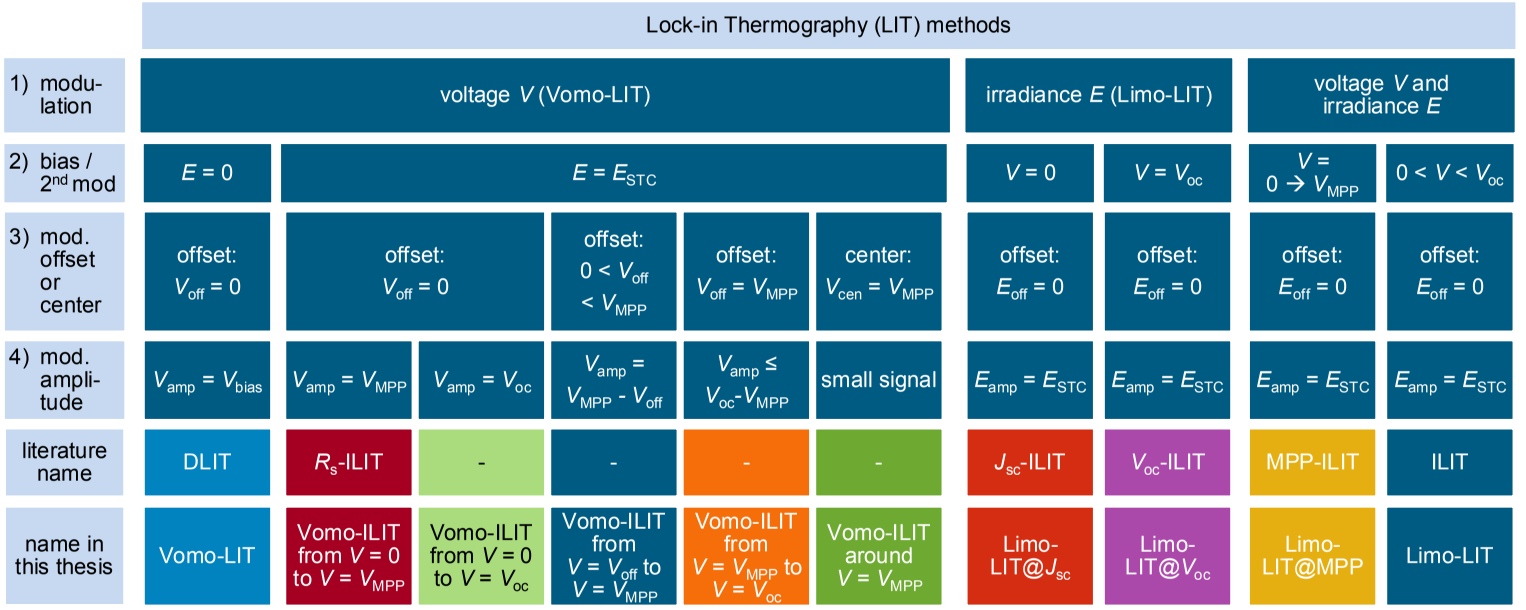

Figure 7.3: Overview scheme of LIT methods. LIT methods can be structured in four hierarchical levels: 1) The applied modulation source. This can be either an applied voltage V or light with the irradiance E. According to this classification, methods using a modulated voltage are called Vomo-LIT and methods using modulated light Limo-LIT. 2) The applied constant bias. If the voltage is modulated, light as a constant bias can be applied, and vice versa. The bias value can be chosen freely, reasonable points are listed in the scheme. 3) The modulation offset or center. The modulation offset is the lower value of the modulation. Alternatively to the lower and upper values of the modulation, the modulation center can be given. The modulation is then carried out around the modulation center. 4) The modulation amplitude. This is the upper value of the modulation if no offset is applied. Otherwise, the modulation amplitude is the value of the modulation height.

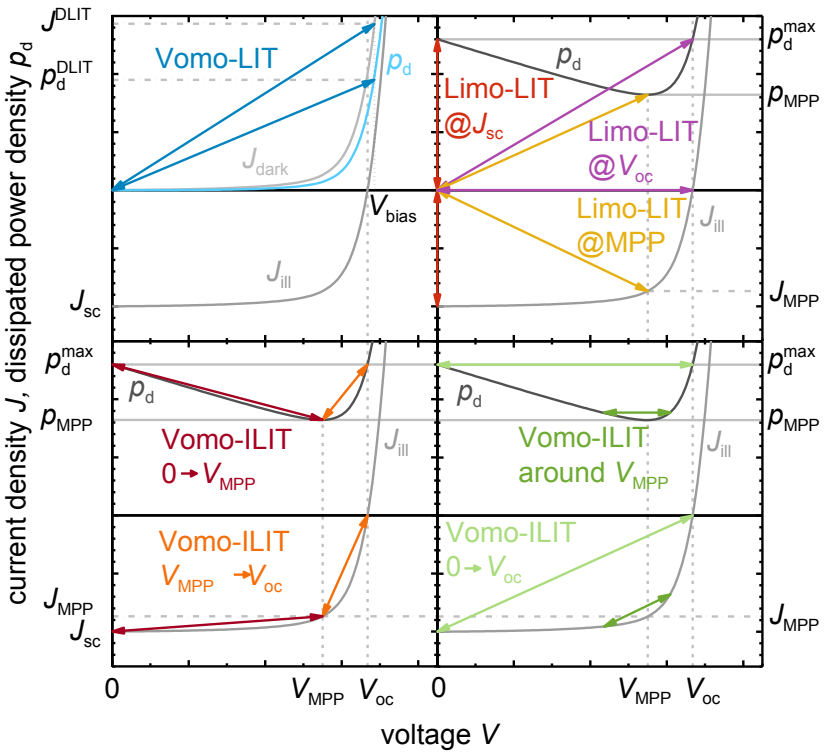

Figure 7.4: Modulation of established and new developed LIT methods by means of solar cell I/V and P/V characteristics. The modulations of the different LIT methods are marked by arrows between the operating points, each in the I/V and p_d/V characteristic. The colors of the arrows match the specific colors of the methods presented in Figure 7.3. The novel methods Vomo-ILIT from V_{MPP} to V_{oc}, from 0 to V_{oc}, and around V_{MPP} are discussed in chapters 7.3 and 7.4.

This method seems more effortful, but has a clear advantage: If many Limo-LIT images at different voltages are recorded (compare the p_d/V characteristic in chapter 7), the Vomo-LIT images can be calculated afterwards between any two recorded voltages. This simplifies the evaluation as specific voltages like V_{MPP} do not need to be known before starting the measurements.

The equality of both methods for the acquisition of Vomo-ILIT images is due to the commutability of the sum in the LIT signal generation. According to equation (3.25), a LIT signal is the sum over single frames F, here as a function of the applied voltage V. The modulation between two voltages leads to a signal

$$S_{\mathrm{mod}}(V) = \frac{1}{nN}\sum_{l=1}^{N}\sum_{m=1}^{n} K_m \left(F_{l,m}(V_2) - F_{l,m}(V_1)\right) \tag{7.2}$$

with the number of correlation bases n, the number of measured lock-in periods N, the correlation vector $K = [K_1, K_2, \dots, K_m, \dots, K_n]$ (see equations (3.26) and (3.27)), and $F_{l,m}$ being the raw temperature signal acquired by the thermographic camera in a certain lock-in period l and at a certain correlation base m. The difference of two separately measured LIT signals S_1 and S_2 at same measurement conditions ($n_1 = n_2 = n$; $N_1 = N_2 = N$) is

$$\begin{aligned} S_{\mathrm{dif}}(V) &= S_2 - S_1 = \frac{1}{nN}\sum_{l=1}^{N}\sum_{m=1}^{n} K_m F_{l,m}(V_2) - \frac{1}{nN}\sum_{l=1}^{N}\sum_{m=1}^{n} K_m F_{l,m}(V_1) \\ &= \frac{1}{nN}\left[\sum_{m=1}^{n} K_m \sum_{l=1}^{N} F_{l,m}(V_2) - \sum_{m=1}^{n} K_m \sum_{l=1}^{N} F_{l,m}(V_1)\right] \\ &= \frac{1}{nN}\sum_{m=1}^{n} K_m \left[\sum_{l=1}^{N} F_{l,m}(V_2) - \sum_{l=1}^{N} F_{l,m}(V_1)\right] \\ &= \frac{1}{nN}\sum_{m=1}^{n} K_m \sum_{l=1}^{N} \Big(F_{l,m}(V_2) - F_{l,m}(V_1)\Big) \\ &= \frac{1}{nN}\sum_{l=1}^{N}\sum_{m=1}^{n} K_m \Big(F_{l,m}(V_2) - F_{l,m}(V_1)\Big) \\ &= S_{\mathrm{mod}}(V). \end{aligned} \tag{7.3}$$

This equality is valid for any two LIT signals measured under the same conditions. In practice, the number of frames per period n should be the same to calculate such differential signals; but the number of measured periods N will only influence the *SNR*. If an absolute power scale shall be used for the quantification of Vomo-ILIT measurements, a high N – and along with that, a long measurement time – should be used obtain reasonable results as explained in chapter 7.1.

7.3 Evaluation of cell voltages with Vomo-ILIT

7.3.1 Vomo-ILIT from $V = 0$ to V_{MPP} (R_{s}-ILIT)

The only LIT method with modulated voltage at a constant illumination that was reported in literature up to now is Vomo-ILIT from $V = 0$ to V_{MPP}. It was introduced as R_{s}-ILIT, as the method made series resistance in crystalline silicon solar cells observable [80]. The signal of Vomo-ILIT from $V = 0$ to V_{MPP} is proportional to the electrically dissipated power in the solar cell. This is illustrated well in Figure 7.4, where the arrow

in the p_d/V characteristic representing the Vomo-ILIT modulation from $V = 0$ to V_{MPP} lies between the same points that are used in chapter 7 for the application of a power density scale to Limo-LIT images.

The modulation direction makes the signal of Vomo-ILIT from $V = 0$ to V_{MPP} of a functioning solar cell essentially negative. A negative dissipated power P_d means that a power generation occurs. Exactly this power generation can be made visible with this method. Figure 7.5 shows an image and an average linescan of the dissipated power density p_d of the *a*-Si solar module used in chapters 4.6 and 7, derived from Vomo-ILIT measurement from $V = 0$ to V_{MPP}. The Vomo-ILIT image was derived by subtracting the Limo-LIT@J_{sc} image from the Limo-LIT@MPP image. The same scaling value of one relative unit conforming to 85.1 W/m² from chapter 7 was used.

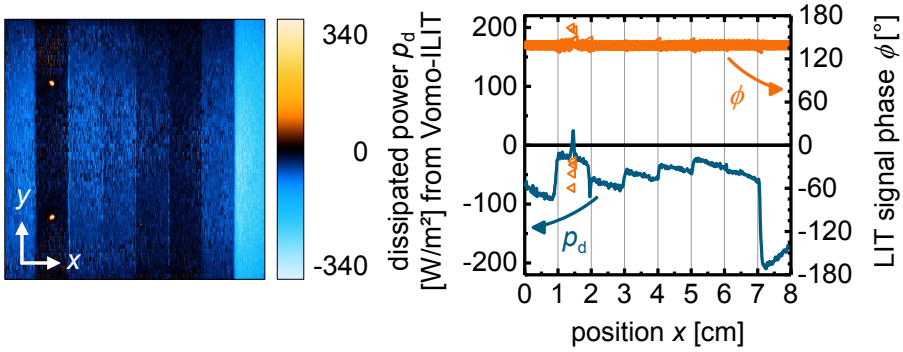

Figure 7.5: Image and average linescan of the dissipated power density p_d as well as phase linescan ϕ of an a-Si module acquired by Vomo-ILIT from $V = 0$ to V_{MPP}. The dissipated power density is essentially negative, conforming to a power generation in the solar module. This is affirmed by the phase signal, which lies close to 135°. The only exception are the shunts in cell 2; where p_d is positive and where ϕ lies approximately around -45°. The gradient over the cells is in opposite direction to the one of the Vomo-LIT linescans in Figure 4.14. The interpretation of the signal of cell 8 is challenging: Here, the signal value is significantly higher compared to the other cells, meaning a higher power generation. Yet, the gradient shows in the opposite direction, giving a clue for the current, which thus is flowing in the opposite direction. This happens if the voltage of the cell V_{cell8} is reversed at $V_m = 0$.

As expected, the dissipated power is essentially negative, conforming to a power generation in the solar module. The phase signal lies close to 135°. This indicates a power generation also: Power dissipation has a phase of $\phi = -45°$ as shown in chapter 3.5, and $135° = -45° + 180°$, meaning that the phase turns around 180° between power generation and dissipation. The only exceptions of the negative dissipated power are the shunts in cell 2, which have a positive Vomo-ILIT signal and a phase of approximate-

ly -45°. This is physically well understandable as shunts consume energy. The cell signal of cell 2 is lower than the signal of the other cells, conforming to a lower power generation. The gradients of the dissipated power over the cell stripes visible in the linescan of p_d are opposed to the gradients found in the Vomo-LIT image linescan of the same module in Figure 4.14. Thus, the signal shows the photo current flow of J_{ph} in contrary to the dark current flow J_{dark} in Vomo-LIT images.

Up to this point, the Vomo-ILIT measurement from $V = 0$ to V_{MPP} delivers a reasonable dissipated power distribution in the solar module. However, the signal of cell 8 deviates from the signals of the other cells: it has a significant higher absolute value, and shows a gradient in the opposite direction. This would mean, that more power is generated compared to the other cells, but with an opposed current flow. This is physically not reasonable. The opposed current can only occur when the voltage on the cell V_{cell8} is reversed. In that case, the cell would dissipate and not generate power. The acquisition of the cell voltages during an *I/V* measurement of the whole module proves the assumption of V_{cell8} being reversed at $V_m = 0$, as Figure 7.6 shows in the discussion in chapter 7.3.2.

The question, why such a high negative dissipated power is acquired, can be explained as follows: The cell voltage V_{cell8} is reversed at the module voltage $V_m = 0$. Therefore, it is inherent to the Limo-LIT@J_{sc} image. The thermal signal from the solar module always has a positive value independent from the direction of the current flow and the algebraic sign of the voltage. It is proportional to the dissipated electrical power. The electrical power is the product of current times voltage. If the voltage of a cell is reversed, the current direction switches also, i.e. both quantities switch their algebraic sign. The product of them, i.e. the electrical power, thus has always the same algebraic sign. This impedes the correct detection of the dissipated power in voltage reversed cells of a module with the Vomo-ILIT method from $V = 0$ to V_{MPP}. Yet, with choosing a higher offset voltage for the modulation, this restriction can be overcome, as the following subchapter shows. As long as all cells of a module are biased with a forward voltage at $V_m = 0$, the Vomo-ILIT method from $V = 0$ to V_{MPP} finds a LIT signal proportional to the generated and dissipated power in a solar module.

An open question is whether the proportionality of the Vomo-ILIT signal and the dissipated power density holds in shunts also. An answer to that question can possibly be found when comparing complex network simulations of shunts with Vomo-ILIT results. This could lead to a realistic estimation of power losses due to shunts.

7.3.2 Vomo-ILIT from $0 < V < V_{MPP}$ to V_{MPP}

To prevent single cells from being reversed biased in Vomo-ILIT measurements, the lower modulation point – the offset voltage V_{off} – can be increased. The higher V_{off},

the more likely all cell voltages are positive. This fact is illustrated in Figure 7.6 showing the measured cell voltages of the investigated solar module over the module voltage V_m during the acquisition of the *I/V* characteristic under the LED light source of the LIT setup.

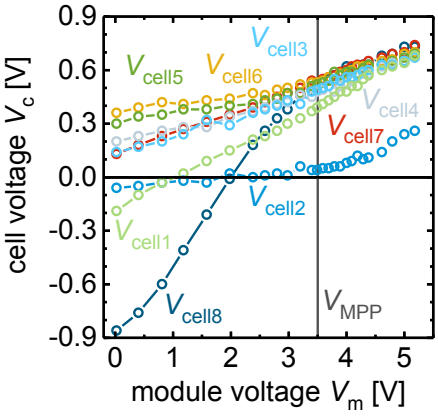

Figure 7.6: Monitored cell voltages during I/V-measurements of the examined a-Si module under illumination of the LED panel of the LIT setup. At low module voltages V_m, three cells are driven in reverse voltage: cell 1, cell 2 and cell 8. At high module voltages V_m above 4 V *the cell voltages distribute equally except for cell 2, as it contains the shunts. For all module voltages $V_m > 2$ V, no reverse biasing on the cells occurs.*

Above a module voltage $V_m > 2$ V, all cells are driven in forward bias. Thus, Vomo-ILIT measurements from an offset voltage above $V_{off} = 2$ V to V_{MPP} could deliver a physically reasonable interpretation of the dissipated power density p_d. Furthermore, the combination of several Vomo-ILIT measurements from different offset voltages $0 < V_{off} < V_{MPP}$ could find out, at which module voltage V_m a cell voltage is reversed. To evaluate these assumptions, Figure 7.7 shows such a comparison of the dissipated power density in the examined solar module gained from Vomo-ILIT measurements using different modulations: from offset voltages $V_{off} = 0$, $V_{off} = 1.8$ V and $V_{off} = 3.5$ V to $V_m = V_{MPP}$. The scaling to p_d was achieved using the factor of 85.1 W/m² for one relative unit of $S^{-45°}$ that was found in chapter 7.

The first modulation from $V_{off} = 0$ conforms to the R_s-ILIT signal from Figure 7.5. As explained above, the voltage at cell 8 V_{cell8} is negative at these conditions. This can be seen from the gradient of the signal, which is in direction of the diode current flow J_d (compare the Vomo-LIT signal in Figure 4.14).

The signal for the modulation from $V_{off} = 1.8$ V shows almost no gradient over cell 8 as $V_{cell8} \approx 0$ at $V_m = 1.8$ V (see Figure 7.6). That means, the module voltage, where the cell voltage is reversed, can be found with this Vomo-ILIT method.

The gradient of the signal of cell 8 for the modulation from $V_{off} = 3.5$ V shows that the current flows in the direction of J_{ph} as in the other cells. Thus, this synopsis of the different Vomo-ILIT modulations finds out at which module voltage V_m cell voltages are reversed. This can be a helpful evaluation of fully processed solar modules, where one has no access to information about cell voltages as the cells cannot be contacted due to the encapsulation of the modules. This is the first reported imaging technique that allows for such a detailed investigation of the cells' behavior in a module at operation conditions.

Concerning a reasonable interpretation of the dissipated power density p_d, it has to be stated that the Vomo-LIT modulation from $V_{off} = 1.8$ V to $V_m = V_{MPP}$ does not hold the proportionality of the acquired LIT signal $S^{-45°}$ and p_d for the signal of cell 8. Thus, the offset voltage for the modulation has to be higher than the module voltage, where cell voltages are just zero, to find a power proportional signal. Yet, a too high voltage close to V_{MPP} shows a partly positive signal in the cells as the linescan of the modulation from $V_{off} = 3.5$ V shows. The interpretation of such a signal is not trivial, because it is not physically reasonable that a cell partly dissipates and partly generates power. Yet, it is probable that a modulation can be found where the offset is found to be optimal so that no reverse cell voltages and no partly positive cell signals occur. Such a signal is then proportional to p_d.

7.3.3 Vomo-ILIT at voltages between V_{MPP} and V_{oc}

The previous two chapters showed that if both module bias voltages for the modulation are chosen so that no reverse biasing on cells occurs, the gradient over average linescans of cells is in the direction of the current flow J_{ph}. In principle, the series resistance R_s of a cell could be calculated by dividing power-proportional Vomo-ILIT signals by the cell voltage. As a first approximation, a uniform voltage over a cell could be assumed. More precise results would be obtained by using a voltage distribution which is either obtained by EL measurements or simulations.

The Vomo-ILIT signals from $V_{off} < V_{MPP}$ to V_{MPP} in Figure 7.7 showed that the gradient over the cells is relatively low compared to the noise of the signal. It is generated by the power difference between the rims of the cell stripe. This power difference is proportional to the current density J and the cell voltage V_{cell}. For high quality solar cells, J_{MPP} is not much lower than J_{sc}, leading to a low current difference between the modulation points. In contrary, the voltage difference can be quite high.

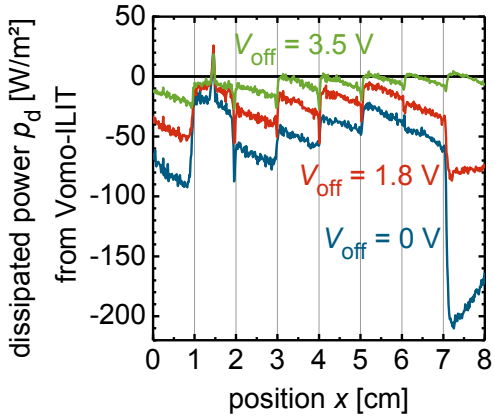

Figure 7.7: Average linescans of the dissipated power density obtained by Vomo-ILIT measurements with modulations from different voltages to V_{MPP}. The closer the modulation offset voltage V_{off} is to V_{MPP}, the smaller the signal is. In this case, V_{cell8} is positive at both module voltages and the signal of cell 8 is comparable to the other cell's signals. By varying the V_{off} it can be found out at which module voltage V_m cell voltages are reversed.

With another modulation, the proportions can be turned around: the modulation from V_{MPP} to V_{oc} has a high current difference of I_{MPP}, and a comparably low voltage difference. The product of both still may cause a higher power difference than at the modulation from $V_{off} < V_{MPP}$ to V_{MPP} and thus give a better basis for the evaluation of R_s.

In contrast to the modulation from $V_{off} < V_{MPP}$ to V_{MPP}, the modulation from V_{MPP} to V_{oc} results in a positive signal for cells that are not affected by defects. This is due to the fact that at voltages above V_{MPP} the solar module dissipates more heat than at V_{MPP} as shown in Figure 7.2. The average power density gained from the Vomo-ILIT signal from V_{MPP} to V_{oc} is depicted in Figure 7.8.

As expected, the signal is mainly positive and the phase lies close to -45° except in the region around the shunts in cell 2 and except the series interconnections between the cells. The signal in the shunts is positive and significantly higher than the signal of the cells. In all cells except cell 2 a gradient can be seen which is in the same direction as in Figure 7.5. So this modulation shows the photo current J_{ph} also. The gradient over the cells is higher compared to the cell gradient of the modulation from $V_{off} = 0$ to V_{MPP} shown in Figure 7.5. Therefore, it possibly could deliver a more reliable interpretation of R_s.

Another possible application for this modulation method is the investigation of the integrated series connection. At V_{oc}, the currents over the series interconnections are relatively low, especially compared to the currents that flow at V_{MPP}. Therefore, the

power flow over the laser scribed interconnections could be interpreted with this signal and deliver a measure for the interconnection quality.

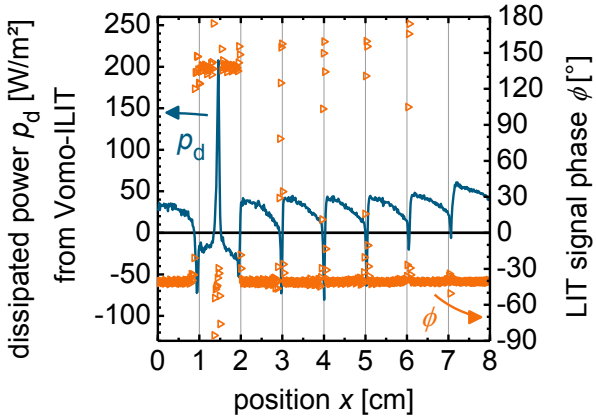

Figure 7.8: Average linescan of the dissipated power density p_d and the phase ϕ acquired by Vomo-ILIT from $V = V_{MPP}$ to V_{oc}. The resulting signal is mainly positive and the phase lies at ϕ = -45° for cells that are not affected by defects. In defects like the shunt in cell 2, the signal is positive also.

In terms of the estimation of power losses, it has to be stated that it is not clear, which Vomo-ILIT modulation delivers the most realistic estimate. The shunt signal in Figure 7.8 is markedly higher than the one in Figure 7.5, as the current difference is higher for the modulation from V_{MPP} to V_{oc}. As stated before, only complex simulations of a shunt's electrical properties combined with the evaluation of Vomo-ILIT signal with different modulations can deliver reliable results for the estimation of power losses due to shunts.

7.4 Realistic evaluation of defects with power-neutral Vomo-ILIT around V_{MPP}

The investigated Vomo-ILIT methods in the previous chapters were mainly carried out with relatively large modulations. The MPP was used as one of the two modulations points, either as goal for the amplitude or as offset. However, if a solar module shall be investigated at realistic operation conditions, i.e. the MPP, a voltage modulation ΔV_{ext} around MPP could deliver insight in the power dissipation and generation mechanisms occurring at these conditions. As the LIT signal is power proportional, a voltage modulation around MPP can be carried out, which is power-neutral. Please note that only in special cases a voltage-symmetric modulation around V_{MPP} would represent such a power-neutral modulation. This voltage modulation is of large interest as the integral

of the modulation signal is zero; therefore any deviations from zero can be referred to features of the solar cell. For the overall dissipated power difference ΔP_d and the locally dissipated power density p_d integrated over the cell's (module's) area *A,*

$$\frac{\Delta P_d}{\Delta V_{ext}} \approx \int_A \frac{d}{dV_{ext}} p_d dA = 0. \tag{7.4}$$

holds due to the conservation of power. If this voltage modulation is carried out for a solar module, the result gives insight in how the module's cells work at realistic operation conditions. As already shown in Figure 7.6, cell voltages do not distribute uniformly in a module. Therefore, the power-over-voltage characteristics of the cells differ also. Figure 7.9 shows the *P/V*-characteristics of the above investigated module and exemplarily, its cells 1 to 4. They were determined by direct measurements of the voltages at the contacts and multiplying the voltages with the overall current.

As can be seen, the module's $V_{\mathrm{MPP}}^{\mathrm{module}}$ does not lie at the same voltage as the $V_{\mathrm{MPP}}^{\mathrm{cells}}$ of the cells. That means, a Vomo-ILIT image with the modulation around MPP should be able to show whether the MPPs of a module's cells lie at higher or lower voltages. In this example, a voltage modulation of the module from $V_\mathrm{m} = 3$ V to $V_\mathrm{m} = 4$ V would result in a dissipated power difference of $\Delta P_\mathrm{d} = 0$. Therefore, the integrated Vomo-ILIT signal should be zero also. In that range, the dissipated power in cells 1 and 2 decreases continuously, i.e. the Vomo-ILIT signal of the modulation around MPP of these cells should be mainly negative. In contrary, the dissipated power in cell 4 is lower at $V = 3$ V, so the signal of cell 4 should be essentially positive. The difference of the dissipated powers in cell 3 is relatively low; therefore the integrated signal over the cell should be around zero. An ideal module which contains of cells that have the exactly same electrical characteristics would result in such signals that have a gradient over a cell with the zero value at its center, and the integral over the cell being zero.

The assumptions made above were verified with Vomo-ILIT measurements around V_MPP with different power-neutral modulations. The modulation voltage points were chosen from Figure 7.2 so that both points had about the same power dissipation. Figure 7.10 shows the resulting images and average linescans scaled with the conversion of one relative unit of S^{-45° to a power density of 85.1 W/m² as found in chapter 7. The images were obtained by subtracting the complex Limo-LIT images of following different bias voltages:

a) from $V_\mathrm{off} = 3.8$ V to 4.6 V, yielding an amplitude voltage of $V_\mathrm{amp} = 0.8$ V,
b) from $V_\mathrm{off} = 3.5$ V to 5.0 V, yielding an amplitude voltage of $V_\mathrm{amp} = 1.5$ V,
c) from $V_\mathrm{off} = 1.8$ V to 5.3 V, yielding an amplitude voltage of $V_\mathrm{amp} = 3.5$ V,

d) from V_{off} = 0.0 V to 5.3 V, yielding an amplitude voltage of V_{amp} = 5.3 V = V_{oc}.

The modulation (d) is an exception as it is not power neutral although it modulates from J_{sc} to V_{oc}. This is due to the discrepancy of the integral LIT signals in both points, which is explained in chapter 7. Still it was carried out to use the information of the entire p_d/V characteristic. All images contain a relatively high amount of noise. This is due to a malfunction of the LIT system, which occurs markedly at Limo-LIT measurements. The camera system builds blocks of one times eight image pixels having similar values and a significant change in the values to the neighboring blocks. The manufacturer was not able to solve this problem. With the subtraction of two Limo-LIT images, the noise increases in some Vomo-LIT images.

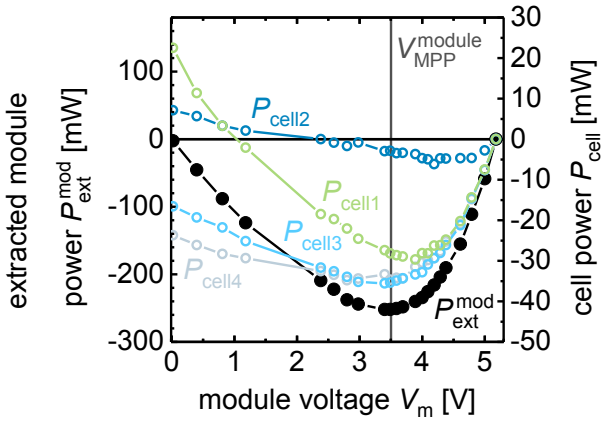

Figure 7.9: Extracted module power density and selected cell power densities of the examined a-Si module. The black curve shows the module's P_{ext}^{mod}/V characteristic; the colored curves the P_{cell}/V characteristics. Due to the cell voltage distribution in the module, the P_{cell}/V curves of the cells differ significantly. Concomitant, the voltages of the respective cell MPPs vary. Therefore a Vomo-ILIT image made with a modulation around the module's MPP will have cell signals related to the voltage of the cells' MPPs: Cells with a MPP at lower V_m than V_{MPP}^{module} will show a positive signal; cells with a MPP at higher V_m than V_{MPP}^{module} will show a negative signal.

The Vomo-LIT images (a) and (b) show a similar signal with a higher contrast in (b) due to the higher modulation amplitude voltage V_{amp}. As predicted from the results in Figure 7.9, the signal of cell 4 is mainly positive. The signal of cell 3 has almost equally high positive and negative signals and the signals of cells 2 and 1 are negative except in the shunts. Hence, the Vomo-LIT measurements agree well with the acquisition of the power densities in the cell measured at the contacts. Therefore, Vomo-ILIT signals with modulations around the MPP of a solar module can be used to evaluate

relatively, at which voltages the MPPs of the module's cells lie in respect to the module's V_{MPP}.

The Vomo-LIT images (c) and (d) show a feature that was observed in the Vomo-ILIT measurements from $0 < V < V_{MPP}$ to V_{MPP} in chapter 7.3.2 also and is clearly visible in the linescans: the high power "generation" in cell 8 and the reversing of the current direction for the modulation (d). Thus using the modulation around V_{MPP} with different voltage modulations can also observe which cell voltages V_{cell} are reversed at certain module voltages V_m. However, the determination of the module voltage V_m where $V_{cell8} = 0$ is not that easy as for the modulation from $0 < V < V_{MPP}$ to V_{MPP}. This is exemplified in the comparison of modulation (c) in Figure 7.10 with the modulation from $V_{off} = 1.8$ V to V_{MPP} in Figure 7.7. The offset voltage of both modulations is $V_{off} = 1.8$ V, but in the gradient in cell 8 is only approximately zero for the modulation ion in Figure 7.7, where it was proven that $V_{cell8} \approx 0$. That means, the modulation part from V_{MPP} towards V_{oc} in modulation (c) influences the gradient so that V_m for $V_{cell8} = 0$ cannot be determined as precisely as with the modulation from $0 < V < V_{MPP}$ to V_{MPP}. Anyway, a synopsis of several Vomo-ILIT signals with different modulations around V_{MPP} and substantial statistical evaluations could find at least approximate values for V_m.

The choice of the modulation for the Vomo-ILIT method around V_{MPP} lies between two conflicting priorities: On the one hand, a relatively small signal modulation is wanted to describe the operation at MPP and to prevent cells from reverse biasing (see modulations (c) and (d) in Figure 7.10). On the other hand, this implies a poor *SNR* of the LIT results leading to relatively high uncertainties in the evaluation of the dissipated power. As a consequence, a suiting amplitude voltage V_{amp} has to be found for each sample separately.

To evaluate these aspects of the Vomo-LIT method on another example, a defective *a*-Si module with several defects was measured. Figure 7.11 shows its Vomo-ILIT around MPP images and average linescans of $S^{-45°}$ and ϕ for the two modulations $V_{amp} = 0.5$ V (a) and $V_{amp} = V_{oc}$ (b). Several remarkable features in the defective module are visible:

- The shunt in cell 6, leading to a high power dissipation, and the weaker shunts in cells 5 and 8;
- the defective edge isolation at the upper rim of the module, where parasitic currents flow;
- the probably defective series interconnection between cells 2 and 5.

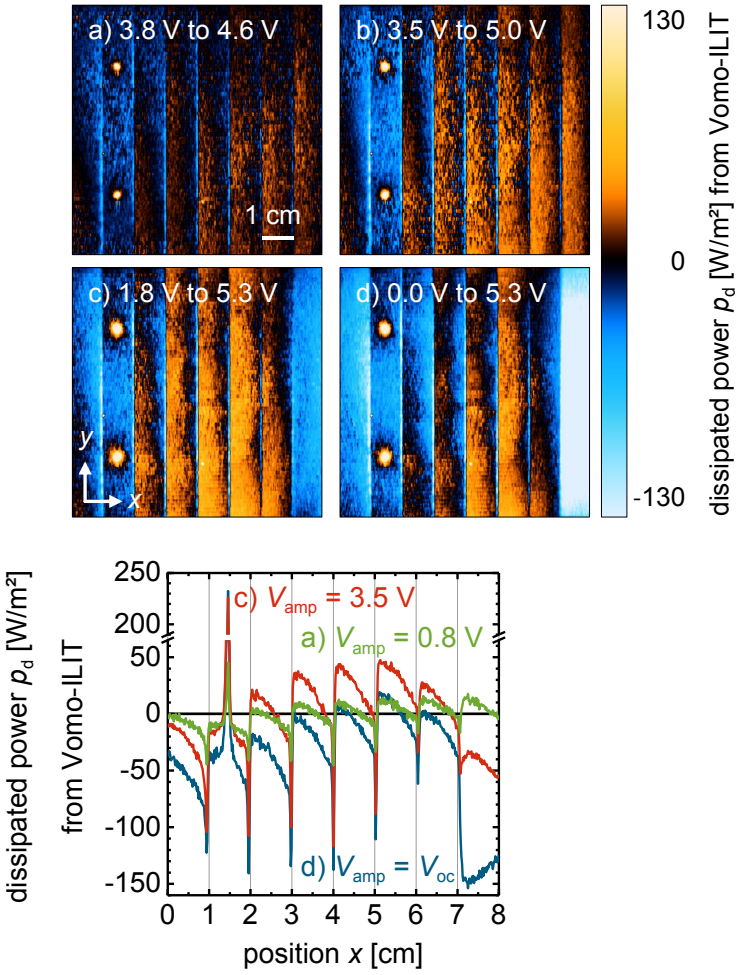

Figure 7.10: Images and average linescans of the dissipated power density derived from Vomo-ILIT with different modulations around V_{MPP}. The modulation around V_{MPP} is matched to fulfill $\Delta P_d = 0$, leading to the integral signal of the whole module being 0 also – except for modulation (d) which uses the complete information of the P_d/V characteristic. All signal / power deviations from zero refer to features in the solar cell. If the signal within a cell is integrally 0, then the cell's MPP has the same voltage as the module's MPP. As shown in Figure 7.9, a signal shift towards positive or negative signals unveils lower or higher V_{MPP}^{cells}, respectively.

The first and the second feature are clearly visible in both $S^{-45°}$ and ϕ images. Due to the good congruence of the two signals, power dissipating and power generating areas can be well distinguished. The negative signals of $S^{-45°}$ conform to a phase of ϕ = 135° and the generation of power. Positive signals of $S^{-45°}$ and a phase of ϕ = -45° conforms to the dissipation of power. As shown above, the $S^{-45°}$ signal is power pro-

portional and can be used for a scaling. The benefit of the phase signal is its preciseness: the series interconnection between cells 2 and 5 show a phase of $\phi = 0°$, giving a hint for a line heat source. This feature cannot be deduced from the $S^{-45°}$ signal.

As explained, the sense of the Vomo-ILIT method is the derivation of a power proportional signal at realistic operation conditions at MPP and thus a modulation as small as possible. Yet there may be reasons to use the modulation over the entire P_d/V characteristic: If the module cannot be biased, the Vomo-LIT image can be determined by the subtraction of two contactless acquired Limo-LIT images, i.e. at V_{oc} and at J_{sc}. Furthermore, the higher signal amplitude – in this example about the factor of 10 as visible from the linescans in Figure 7.11 – eases the evaluation due to its higher *SNR*. In principle, the additional information due to the exploitation of entire P_d/V characteristic could find further features not visible with a small signal modulation.

As shown, Vomo-ILIT is a very powerful tool to find out about the operation conditions of solar cells and their electrical characteristics in operation in solar modules. This is of special interest, since the cells cannot be contacted and monitored after the encapsulation of the module, hampering a realistic evaluation of the defect related losses in solar modules. The Vomo-ILIT method is very flexible as it can be carried out for many different modulations to reveal the interaction of the cells, especially at the most important operation point, the MPP of the module. For example, it can determine, at which module voltages cell voltages become negative when using modulations between $V = 0$ and V_{MPP}. A reverse voltage stresses affected cells and potentially leads to damage. If these "turnover points" are known, a protective mechanism could be implemented in the MPP-trackers[7], which prevents the module voltage from dropping under these critical voltages. The Vomo-ILIT method can principally be performed outdoors and scaled up to PV-arrays also. It allows a power density scaling under use of the extracted electrical power at MPP (the most relevant operation point). Thus, it is the LIT method obtaining the most realistic results for the quantification of power losses in solar modules.

[7] MPP-trackers are devices that set the voltage in a module or array, trying always to hold it in the MPP.

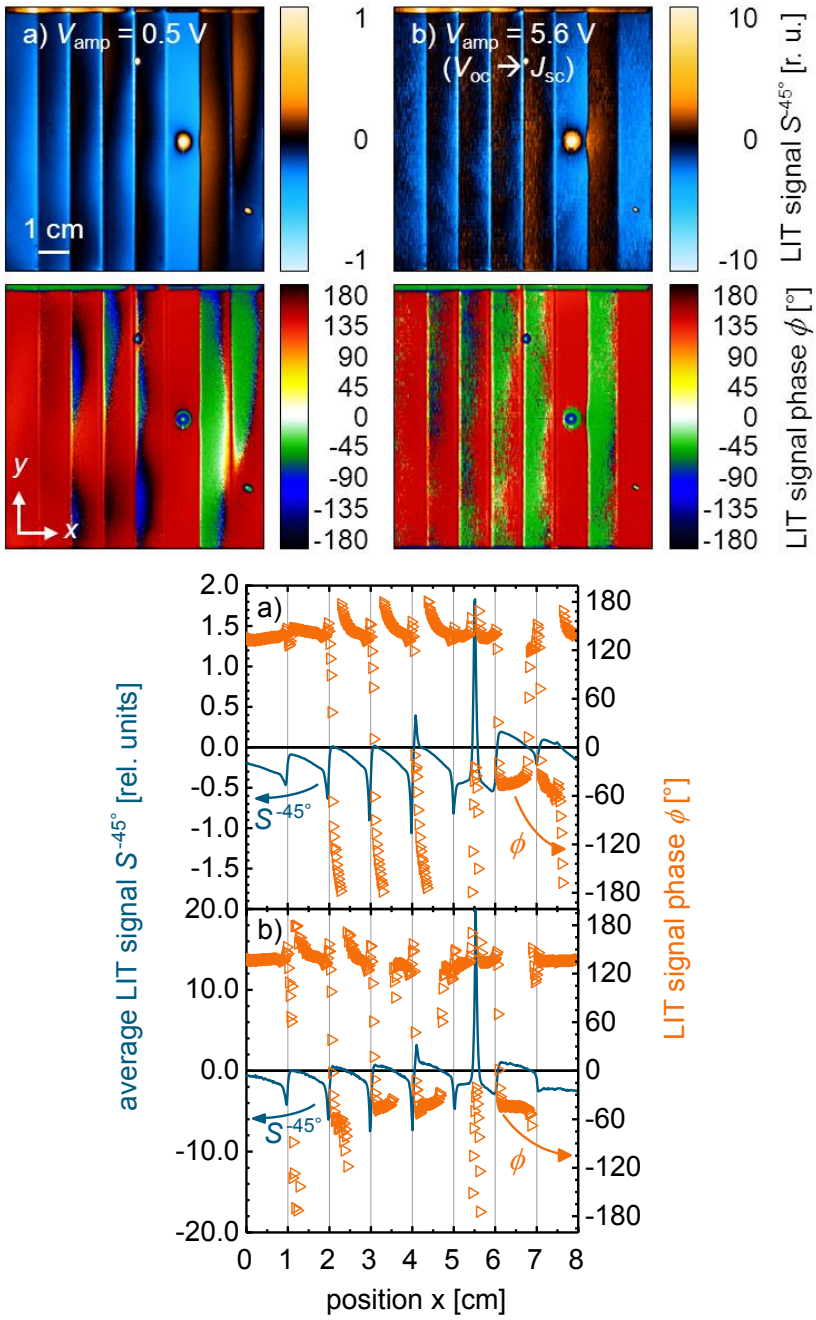

Figure 7.11: Vomo-ILIT signals around MPP of a defective a-Si module for two modulations with V_{amp} = 0.5 V (a) and V_{amp} = V_{oc} (b). Several defect areas are visible: The shunts in cell 5, 6 and 8; the defective edge isolation at the upper rim of the module, and the probably defective series interconnection between cells 2 and 5. The latter feature is only visible in the phase signal ϕ by negative values there (power consumption).

8 Discussion and Conclusions

In the past decade, Lock-in Thermography (LIT) has become a widely used characterization technique for crystalline silicon solar cells. For the investigation of thin film solar cell devices, it has not yet become a standard tool. This is due to the high costs of a LIT setup, the low market share of thin film photovoltaics and the humble knowledge on the operation of LIT systems including the interpretation of its results. Indeed, the LIT process implies a complicated algorithm that contains obstacles in its application. Even commercially available LIT systems comprise error sources due to insufficiently restricted measurement parameters and even wrong implementations. The present thesis works out, how LIT can successfully be used for the defect analysis of thin film silicon solar modules. It equips operators of a LIT system with the knowledge, how correct measurement preferences can be found and how results can be interpreted. Most findings are transferable to other thin film solar cell technologies also, or need few adaptions only.

A detailed evaluation of the lock-in algorithm reveals its weak points and shows how pitfalls can be avoided, or corrected afterwards. The first pitfall is the adaption of the lock-in correlation function coefficients to the excitation signal. It causes errors in the absolute amplitude value. The correct correlation coefficient c for a rectangular excitation signal is $c = \pi$; the most established coefficient $c = 2$ is only valid for a sinusoidal excitation. The correlation with the 4-bucket method needs a correlation coefficient of $c = 2\sqrt{2}$. The second pitfall is the location of the correlation vectors in a period. To avoid errors in the amplitude and phase acquisition, they should be centered and evenly distributed over the period. The third pitfall is the sampling of the measured signal hampering the acquisition of the correct phase signal at measurement frequencies above $f_{\text{lock-in}} = 10$ Hz. Here, only the use of higher sampling rates can help, otherwise the frequency limit should be adhered if correct quantitative results are needed.

A practical measurement problem is, how an LIT signal acquired through a glass encapsulation of a solar module deviates from an LIT signal acquired from the semiconductor's surface. I find that the acquisition through glass only dampens the LIT signal and is not disturbed by the glass or the transparent conductive oxide (TCO) layer. The damping leads to a lower signal-to-noise ratio (*SNR*). Thus, small temperature differences at low excitation power are hardly detectable. This may be overcome by applying a more powerful excitation or by using longer measurement times and lower lock-in frequencies.

The quantitative evaluation of LIT images of entire thin film modules is possible by converting the arbitrary or temperature scaling to a power density scaling. Depend-

ing on the measurement settings, resistance related defects, i.e. series/sheet resistance and shunts can be pronounced in acquired LIT images. A classification of shunts is presumably redundant, since their electrical characteristics are ohmic and their origin seems to have the same cause: focused ion beam (FIB) measurements showed that in thin film silicon solar cells, shunts are direct short-circuits between the front and the back contact due to an locally missing absorber layer. Shunts probably only vary in their size and the type of impurity that causes them.

The investigation of consequences of reverse biasing a thin film solar cell finds the creation of new shunts. The new created shunts lie close to existing shunts and at the series interconnection of the cell. This permanent damage can lead to a decrease of the cell's efficiency. The treatment of "shunt bursting" or "shunt removing" uses reverse biasing to enhance the efficiency of shunted cells. Its effect bases presumably on a more balanced current distribution over a cell stripe due to the new created shunts at the series connection. They prevent the shunt from concentrating most of the cell's current, as the current can flow over the edge shunts.

The calculation of the heat diffusion differential equation with a simple thermal model of a point heat source finds the heat diffusivity and thermal diffusion length of a thin film solar cell. With theoretical calculations, criteria for the acquisition of the global phase are found, namely the point heat source phase that has to be 0° and the integral phase that has to be -45° for lock-in frequencies above 1 Hz.

Combining the thermal model with LIT measurements, a deconvolution technique using Fourier transform finds the originating electrical power distribution and cancels the "blurring" of the heat. This technique reproduces the actual sizes of defects at the expense of a worse *SNR*. An idea for the measurement of the heat diffusion with a small laser spot instead of its calculation avoids the manual fitting process. This leads to a "self-calibrating" LIT system that can measure the heat diffusion of a sample and that automatically deconvolutes the LIT result, revealing the actual size of power dissipation sources.

The estimation of the influence of shunts on a cell's or module's efficiency has been tried with LIT without illumination before. In principle, the dark and illuminated currents in thin film solar cells differ, which makes this approach unrealistic. Solar cells are operated under illumination and at the point of maximal power extraction (MPP). The comparison with LIT results under illumination at MPP finds an overestimation of the shunt's influence in LIT images without illumination. In contrary, in light-modulated LIT measurements at MPP, shunts may be underestimated because of a high LIT signal contribution due to irradiance. An approach for a novel LIT method using a differential voltage modulation under illumination could make it possible to realistically evaluate the actual influence of shunts. Furthermore, this novel LIT method gives in-

sight into the operation and interaction of cells connected in a module without the need of contacting the single cells. This is especially interesting for capsuled modules, where single cells cannot be contacted. Another presented LIT method uses the measurement of several LIT images under constant illumination and at different voltages to derive a "thermal" *P/V*-characteristic of a solar module. The subtraction of two images at different voltages delivers information on the power dissipation in the solar module between these bias conditions. Depending on the choice of the biases, e.g. it can be found at which module voltage the voltage of a cell reverses. The reverse voltage potentially leads to damage. If the biases are chosen around the MPP, one derives the operation points of the cells of a module, showing whether their respective MPPs lie at higher or lower voltages. Additionally, regions of power generation and power dissipation can be distinguished. This information can be used to calculate the influence of defects, to optimize the interaction of solar cells in a module, or to develop algorithms for MPP trackers preventing reverse biasing, for example.

In summary, the present thesis delivers the basic knowledge for the operation of LIT systems and presents methods for the failure analysis and optimization of thin film solar modules. The findings about the LIT process could be implemented in future LIT systems to avoid operational errors. The self-calibrating LIT system would allow for an insight into many types of investigated samples without the need of knowing their thermal properties. Combined with simulations, the introduced novel LIT method with differential voltages under illumination has great potential to investigate the interaction of solar cells in a module. This can lead to a deeper understanding of interconnection processes and the further optimization of the efficiency of solar modules.

Bibliography

[1] G. Masson, M. Latour and D. Biancardi, *Global Market Outlook for Photovoltaics until 2016* (2012), online at http://www.epia.org/?id=20, accessed 11 Mar. 2013

[2] D. Boehme, *Development of renewable energy sources in Germany in 2011* (2012), online at http://www.bmu.de/fileadmin/bmu-import/files/english/pdf/application/pdf/ee_in_deutschland_graf_tab_en.pdf, accessed 11 Mar. 2013

[3] National Center for Photovoltaics, *Research Cell Efficiency Records* (2012), online at http://www.nrel.gov/ncpv/images/efficiency_chart.jpg, accessed 11 Mar. 2013

[4] B. Rech and H. Wagner, Appl. Phys. A **69**, 155 (1999)

[5] M. Osborne, *Fraunhofer ISE targets efficiency losses from the cell to the module to only 2.5%* (2011), online at http://www.pv-tech.org/news/fraunhofer_ise_targets_efficiency_losses_from_the_cell_to_the_module_to_onl, accessed 11 Mar. 2013

[6] O. Breitenstein, W. Warta and M. Langenkamp, *Lock-in Thermography* (Springer, Berlin, 2010)

[7] O. Breitenstein, M. Langenkamp, O. Lang and A. Schirrmacher, Sol. Energy Mater. Sol. Cells **65**, 55 (2001)

[8] M. Kasemann, D. Grote, B. Walter, W. Kwapil, T. Trupke, Y. Augarten, R. Bardos, E. Pink, M. Abbott and W. Warta, Prog. Photovolt: Res. Appl. **16**, 297 (2008)

[9] H. Nesswetter, P. Lugli, A. Bett and C. G. Zimmermann, IEEE J. Photovolt. **3**, 353 (2013)

[10] M. Bokalič, U. O. Krašovec, M. Hočevar and M. Topič, in *Conference record of the 35th IEEE Photovoltaic Specialists Conference* (Austin, Texas, USA, 2012), p. 001507

[11] O. Breitenstein, J. Bauer, K. Bothe, D. Hinken, J. Mueller, W. Kwapil, M. C. Schubert and W. Warta, IEEE J. Photovolt. **1**, 159 (2011)

[12] D. Shvydka, Appl. Phys. Lett. **84**, 729 (2004)

[13] J. Bachmann, C. Buerhop-Lutz, C. Deibel, I. Riedel, H. Hoppe, C. J.Brabec and V. Dyakonov, Sol. Energy Mater. Sol. Cells **94**, 642 (2010)

[14] S. Johnston, I. Repins, N. Call, R. Sundaramoorthy, K. M. Jones and B. To, in *Conference record of the 35th IEEE Photovoltaic Specialists Conference* (IEEE, Honolulu, Hawaii, USA, 2010), p. 001727

[15] T. Tran, B. Pieters, M. Siegloch, A. Gerber, C. Ulbrich, T. Kirchartz, R. Schaeffler and U. Rau, in *Conference Record of the 26th European Photovoltaic Solar Energy Conference* (WIP Renewable Energies, Hamburg, 2011), p. 2981

[16] H. Straube, J.-M. Wagner, J. Schneider and O. Breitenstein, J. Appl. Phys. **110**, 084513 (2011)

[17] T. Lanz, M. Bonmarin, M. Stuckelberger, C. Schlumpf, C. Ballif and B. Ruhstaller, IEEE J. Sel. Top. Quantum Electron. (to be published) (2013)

[18] M. A. Green, Prog. Photovolt: Res. Appl. **9**, 123 (2001)

[19] A. Shah, J. Meier, A. Buechel, U. Kroll, J. Steinhauser, F. Meillaud, H. Schade and D. Dominé, Thin Solid Films **502**, 292 (2006)

[20] D. Abou-Ras, T. Kirchartz and U. Rau, *Advanced Characterization Techniques for Thin Film Solar Cells* (Wiley-VCH, Berlin, 2011)

[21] T. Repmann, B. Sehrbrock, C. Zahren, H. Siekmann and B. Rech, Sol. Energy Mater. Sol. Cells **90**, 3047 (2006)

[22] H. M. Yates, P. Evans, D. W. Sheel, S. Nicolay, L. Ding and C. Ballif, Surf. Coat. Technol. **213**, 167 (2012)

[23] J. Mueller, G. Schoepe, O. Kluth, B. Rech, V. Sittinger, B. Szyszka, R. Geyer, P. Lechner, H. Schade, M. Ruske, G. Dittmar and H.-P. Bochem, Thin Solid Films **442**, 158 (2003)

[24] J. Krc, M. Zeman, O. Kluth, F. Smole and M. Topic, Thin Solid Films **426**, 296 (2003)

[25] C. Beneking, B. Rech, S. Wieder, O. Kluth, H. Wagner, W. Frammelsberger, R. Geyer, P. Lechner, H. Ruebel and H. Schade, Thin Solid Films **351**, 241 (1999)

[26] D. Staebler and C. Wronski, Appl. Phys. Lett. **31**, 292 (1977)

[27] B. Rech, O. Kluth, T. Repmann, T. Roschek, J. Springer, J. Mueller, F. Finger, H. Stiebig and H. Wagner, Sol. Energy Mater. Sol. Cells **74**, 439 (2002)

[28] S. C. Gau, IEEE J. Photovolt. **3**, 72 (2013)

[29] S. Haas, *Untersuchung und Optimierung der Serienverschaltung von Silizium-Duennschicht-Solarmodulen,* PhD thesis, RWTH Aachen University (2010), online at http://hdl.handle.net/2128/4356, accessed 10 Mar. 2013

[30] P. Würfel, *Physics of Solar Cells* (WILEY-VCH Verlag, Weinheim, 2005)

[31] C. Sah, R. Noyce and W. Shockley, Proc. of the IRE **45**, 1228 (1957)

[32] J. Beier and B. Voss, in *Conference record of the 23rd IEEE Photovoltaic Specialists Conference* (Louisville, Kentucky, USA, 1993), p. 321

[33] A. van der Heide, J. Bultman, J. Hoomstra, A. Schonecker, G. Wyers and W. Sinke, in *Conference record of the 29th IEEE Photovoltaic Specialists Conference* (New Orleans, Louisiana, USA, 2002)

[34] M. Acciarria, S. Binettia, A. Racza, S. Pizzinia and G. Agostinelli, Sol. Energy Mater. Sol. Cells **72**, 417 (2002)

[35] B. Moralejo, M. Gonzalez, J. Jimenez, V. Parra, O. Martinez, J. Gutierrez and O. Charro, J. Electron. Mater. **39**, 663 (2010)

[36] J. A. Poce-Fatou, J. Martín, R. Alcántara and C. Fernández-Lorenzo, Rev. Sci. Instrum. **73**, 3895 (2002)

[37] A. Kaminski, O. Breitenstein, J. P. Boyeaux, P. Rakotoniaina and A. Laugier, J. Phys.: Condens. Matter **16**, 9 (2004)

[38] J. Carstensen, G. Popkirov, J. Bahr and H. Föll, Sol. Energy Mater. Sol. Cells **76**, 599 (2003)

[39] M. Kasemann, M. C. Schubert, M. The, M. Köber, M. Hermle and W. Warta, Appl. Phys. Lett. **89**, 224102 (2006)

[40] K. Ramspeck, K. Bothe, D. Hinken, B. Fischer, J. Schmidt and R. Brendel, Appl. Phys. Lett. **90**, 153502 (2007)

[41] D. Hinken, K. Ramspeck, K. Bothe, B. Fischer and R. Brendel, Appl. Phys. Lett. **91**, 182104 (2007)

[42] H. Kampwerth, T. Trupke, J. W. Weber and Y. Augarten, Appl. Phys. Lett. **93**, 202102 (2008)

[43] T. Trupke, E. Pink, R. A. Bardos and M. D. Abbott, Appl. Phys. Lett. **90**, 093506 (2007)

[44] V. Quaschning and R. Hanitsch, Sol. Energy **56**, 513 (1996)

[45] O. Breitenstein, J. Bauer, J.-M. Wagner and A. Lotnyk, Prog. Photovolt: Res. Appl. **16**, 679 (2008)

[46] J. K. Arch, F. A. Rubinelli, J.-Y. Hou and S. J. Fonash, J. Appl. Phys. **69**, 7674 (1991)

[47] M. Topic, F. Smole and J. Furlan, J. Appl. Phys. **79**, 8537 (1996)

[48] M. Zeman, J. A. Willemen, L. L. Vosteen, G. Tao and J. W. Metselaar, Sol. Energy Mater. Sol. Cells **46**, 81 (1997)

[49] M. Burgelman, P. Nollet and S. Degrave, Thin Solid Films **361-362**, 527 (2000)

[50] K. Ding, T. Kirchartz, B. E. Pieters, C. Ulbrich, A. M. Ermes, S. Schicho, A. Lambertz, R. Carius and U. Rau, Sol. Energy Mater. Sol. Cells **95**, 10 (2011)

[51] O. Breitenstein, J. P. Rakotoniaina, M. H. Al Rifai and M. Werner, Prog. Photovolt: Res. Appl. **12**, 529 (2004)

[52] O. Breitenstein, J. P. Rakotoniaina, A. S. van der Heide and J. Carstensen, Prog. Photovolt: Res. Appl. **13**, 645 (2005)

[53] R. S. Crandall, J. Appl. Phys. **54**, 7176 (1983)

[54] C. Hof, *Thin Film Solar Cells of Amorphous Silicon: Influence of i-layer Material on Cell Efficiency,* PhD thesis (University of Neuchâtel, Neuchâtel, 1999)

[55] J. van den Heuvel, R. van Oort and M. Geerts, Solid State Commun. **69**, 807 (1989)

[56] D. E. Carlson, Sol. Energy Mater. **3**, 503 (1980)

[57] X. P. Maldague, *Infrared Methodology and Technology* (Gordon and Breach Science Publishers S.A., Amsterdam, 1994)

[58] M. Kasemann, B. Walter, C. Meinhardt, J. Ebser, W. Kwapil and W. Warta, J. Appl. Phys. **103**, 113503 (2008)

[59] R. Dicke, P. J. Peebles, P. G. Roll and D. T. Wilkinson, Astrophys. J. **142**, 414 (1965)

[60] M. Harwit, *Interview of Robert Dicke,* Niels Bohr Library & Archives, American Institute of Physics, College Park, Maryland, USA (1985), online at http://www.aip.org/history/ohilist/4572.html, accessed 12 Mar. 2013

[61] W. C. Michels and N. L. Curtis, Rev. Sci. Instrum. **12**, 444 (1941)

[62] W. C. Michels and R. C. Barbera, Rev. Sci. Instrum. **23**, 293 (1952)

[63] E. A. Johnson, R. C. Meyer, R. E. Hopkins and W. H. Mock, J. Opt. Soc. Am. **29**, 512 (1939)

[64] A. M. Skellett, Bell Sys. Tech. J. **19**, 249 (1940)

[65] C. R. Cosens, Proc. Phys. Soc. **46**, 818 (1934)

[66] J. C. Krapez, in *Quantitative Infrared Thermography 4 (QIRT'98)* (Lodart S.A. Lodz, Lodz, Poland, 1998), p. 148–153

[67] A. Kaminski, J. Jouglar, M. Mergui, Y.Jourlin, A. Bouille, P. L. Vuillermoz and A. Laugier, Sol. Energy Mater. Sol. Cells **51**, 233 (1998)

[68] C. E. Shannon, Proc. Institute of Radio Engineers **37**, 10 (1949)

[69] H. Nyquist, Trans. AIEE **47**, 617 (1928)

[70] J. Isenberg and W. Warta, J. Appl. Phys. **95**, (2004)

[71] J. Isenberg and W. Warta, Prog. Photovolt: Res. Appl. **12**, 339 (2004)

[72] J. Isenberg, *Neue Infrarotmeßtechniken für die Photovoltaik,* PhD thesis, University of Konstanz (2004), online at https://kops.ub.uni-konstanz.de/xmlui/browse?value=Isenberg%2C+J%C3%B6rg&type=author, accessed 13 Mar. 2013

[73] J. Isenberg, S. Riepe, S. W. Glunz and W. Warta, J. Appl. Phys. **93**, 4268 (2003)

[74] G. Busse, D. Wu and W. Karpen, J. Appl. Phys. **71**, 3962 (1992)

[75] M. Kaes, S. Seren, T. Pernau and G. Hahn, Prog. Photovolt: Res. Appl. **12**, 355 (2004)

[76] I. E. Konovalov, O. Breitenstein and K. Iwig, Sol. Energy Mater. Sol. Cells **48**, 53 (1997)

[77] K. Ramspeck, K. Bothe, J. Schmidt and R. Brendel, J Mater Sci: Mater Electron **19**, 4 (2008)

[78] J. Isenberg, A. S. van der Heide and W. Warta, Prog. Photovolt: Res. Appl. **13**, 697 (2005)

[79] O. Breitenstein, J. P. Rakotoniaina and M. H. Al Rifai, Prog. Photovolt: Res. Appl. **11**, 515 (2003)

[80] O. Breitenstein and J. P. Rakotoniaina, J. Appl. Phys. **97**, 074905 (2005)

[81] M. Langenkamp and O. Breitenstein, Sol. Energy Mater. Sol. Cells **72**, 433 (2002)

[82] J. Bauer, O. Breitenstein and J. P. Rakotoniaina, Phys. Status Solidi A **204**, 2190 (2007)

[83] U. Rau, Phys. Rev. B **76**, 085303 (2007)

[84] T. Kirchartz and U. Rau, J. Appl. Phys. **102**, 104510 (2007)

[85] T. Kirchartz, A. Helbig, W. Reetz, M. Reuter, J. H. Werner and U. Rau, Prog. Photovolt: Res. Appl. **17**, 394 (2009)

[86] T. C. Mueller, B. E. Pieters, T. Kirchartz, R. Carius and U. Rau, Phys. Status Solidi C **9**, 1963 (2012)

[87] S. S. Hegedus, Prog. Photovolt: Res. Appl. **5**, 151 (1997)

[88] A. Johansson, R. Gottschalg and D. G. Infield, in *Conference record of the 3rd World Conference on Photovoltaic Energy Conversion* (Osaka, Japan, 2003), p. 1934

[89] V. Quaschning, *Simulation der Abschattungsverluste bei solarelektrischen Systemen* (Verlag Dr. Koester, Berlin, 1996)

[90] D. Lausch, K. Petter, R. Bakowskie, C. Czekalla, J. Lenzner, H. v. Wenckstern and M. Grundmann, Appl. Phys. Lett. **97**, 073506 (2010)

[91] O. Breitenstein, J. Bauer, A. Lotnyk and J.-M. Wagner, Superlattices Microstruct. **45**, 182 (2009)

[92] O. Breitenstein, J. Bauer, K. Bothe, W. Kwapil, D. Lausch, U. Rau, J. Schmidt, M. Schneemann, M. C. Schubert, J.-M. Wagner and W. Warta, J. Appl. Phys. **109**, 071101 (2011)

[93] A. Haehnel, J. Bauer, H. Blumtritt, O. Breitenstein, D. Lausch and W. Kwapil, J. Appl. Phys. **113**, 044505 (2013)

[94] T. McMahon and M. Bennett, Sol. Energy Mater. Sol. Cells **41-42**, 465 (1996)

[95] V. G. Karpov, G. Rich, A. V. Subashiev and G. Dorer, J. Appl. Phys. **89**, 4975 (2001)

[96] T. J. McMahon, T. J. Berniard and D. S. Albin, J. Appl. Phys. **97**, 054503 (2005)

[97] S. Dongaonkar, J. D. Servaites, G. M. Ford, S. Loser, J. Moore, R. M. Gelfand, H. Mohseni, H. W. Hillhouse, R. Agrawal, M. A. Ratner, T. J. Marks, M. S. Lundstrom and M. A. Alam, J. Appl. Phys. **108**, 124509 (2010)

[98] D. Kendig, G. B. Alers and A. Shakouri, in *Conference record of the 26th Semiconductor Thermal Measurement and Management Symposium* (Santa Clara, CA, USA, 2010), p. 245

[99] S. Dongaonkar, K. Y, D. Wang, M. Frei and S. Mahapatra, IEEE Electron Device Lett. **31**, 1266 (2010)

[100] B. E. Pieters, *Characterization of Thin-Film Silicon Materials and Solar Cells through Numerical Modeling,* PhD thesis (Delft University of Technology, Delft, 2008)

[101] H. Straube, O. Breitenstein and J.-M. Wagner, Phys. Status Solidi B **248**, 2128 (2011)

[102] H. Carslaw and J. Jaeger, *Conduction of Heat in Solids* (Oxford University Press, London, 1959)

[103] S. Haas, A. Gordijn and H. Stiebig, Prog. Photovolt: Res. Appl. **16**, 195 (2007)

[104] S. Ku, S. Haas, B. E. Pieters, U. Zastrow, A. Besmehn, Q. Ye and U. Rau, Appl. Phys. A **105**, 355 (2011)

[105] J. T. Bushbert, J. A. Seibert, E. M. Leidholdt Jr. and J. M. Boone, *The Essential physics of medical imaging* (Lippincott Williams & Wilkins, Philadelphia, PA, USA, 2002)

Acknowledgements

The process of research and writing a PhD thesis is something a sole person could possibly never manage. There are a lot of people who contributed to this work to variable extent, but every contribution was absolutely necessary. Instead of listing all contributors (to which I count at least 50 persons), I would like to express my thanks generally. I am sure that every contributor knows her/his involvement best herself/himself. Every one of you supported me with the aid that she/he could give, and often I needed this aid to your own limits. Still, I am impressed by the unselfishness, the kindness and often the warmth that I encountered. I hope I am able to give you the same outstanding support that I received. Thank you all very much indeed.

Band / Volume 245
Light scattering and trapping in thin film silicon solar cells with an n-i-p configuration
W. Böttler (2015), 132 pp
ISBN: 978-3-95806-023-4

Band / Volume 246
Nanostructured Si-alloys for silicon solar cells
K. Ding (2015), 210 pp
ISBN: 978-3-95806-024-1

Band / Volume 247
Electrochemical Texturing and Deposition of Transparent Conductive Oxide Layers for the Application in Silicon Thin-Film Solar Cells
J.-P. Becker (2015), ix, 156, XXIV pp
ISBN: 978-3-95806-027-2

Band / Volume 248
Stoffliche Charakterisierung radioaktiver Abfallprodukte durch ein Multi-Element-Analyseverfahren basierend auf der instrumentellen Neutronen-Aktivierungs-Analyse – MEDINA –
A. W. Havenith (2015), 311 pp
ISBN: 978-3-95806-033-3

Band / Volume 249
Quantitative Two-Layer Inversion and Customizable Sensor-Array Instrument for Electromagnetic Induction based Soil Conductivity Estimation
A. T. Mester (2015), viii, 119 pp
ISBN: 978-3-95806-035-7

Band / Volume 250
Partial Neutron Capture Cross Sections of Actinides using Cold Neutron Prompt Gamma Activation Analysis
C. Genreith (2015), vii, 166, XXXII pp
ISBN: 978-3-95806-036-4

Band / Volume 251
Long Term Aerosol Composition Measurements at the CESAR Tower at Cabauw, NL
P. Schlag (2015), iii, 228 pp
ISBN: 978-3-95806-037-1

Band / Volume 252
Modellbasierte Spezifikationsmethodik zur effizienten Systementwicklung von Brennstoffzellenantrieben
R. Biurrun Sotelo (2015), 255 pp
ISBN: 978-3-95806-038-8

Band / Volume 253
Three-dimensional ray-tracing simulations of convective gravity waves
S. Kalisch (2015), iii, 183 pp
ISBN: 978-3-95806-040-1

Band / Volume 254
First-Principles Study on Pyrites and Marcasites for Photovoltaic Application
T. Schena (2015), 206 pp
ISBN: 978-3-95806-041-8

Band / Volume 255
Glass-Ceramic Sealant Reinforcement for High-Temperature Applications
B. Cela Greven (2015), xi, 119 pp
ISBN: 978-3-95806-042-5

Band / Volume 256
Entwicklung planarer $Ba_{0,5}Sr_{0,5}Co_{0,8}Fe_{0,2}O_{3-\delta}$-Membranmodule zur Sauerstoffabtrennung und Analyse ihres Transportverhaltens
P. Niehoff (2015), VIII, 134 pp
ISBN: 978-3-95806-044-9

Band / Volume 257
Extension of the Reactor Dynamics Code MGT-3D for Pebble-bed and Block-type High-Temperature-Reactors
D. Shi (2015), x, 162 pp
ISBN: 978-3-95806-045-6

Band / Volume 258
Failure Analysis of Thin Film Solar Modules using Lock-in Thermography
M. Siegloch (2015), XIII, 131 pp
ISBN: 978-3-95806-047-0

Energie & Umwelt /
Energy & Environment
Band / Volume 258
ISBN 978-3-95806-047-0